

UC Merced

UC Merced Electronic Theses and Dissertations

Title

Performance analysis of medium temperature non-tracking solar thermal concentrators

Permalink

<https://escholarship.org/uc/item/2p969963>

Author

Balkoski, Kevin

Publication Date

2011-12-15

Peer reviewed|Thesis/dissertation

UNIVERSITY OF CALIFORNIA
Merced

Performance Analysis of Medium Temperature Non-Tracking Solar Thermal Concentrators

A thesis submitted in partial satisfaction of the requirements for the degree of

Master of Science

in

Mechanical Engineering and Applied Mechanics

by

Kevin M. Balkoski

Fall 2011

The thesis of
Kevin M. Balkoski is approved:

Professor Roland Winston

Professor Gerardo Diaz

Professor Michael Modest

University of California, Merced

Fall 2011

Performance Analysis of Medium Temperature Non-Tracking Solar Thermal Concentrators

Copyright © 2011

by

Kevin M. Balkoski

Acknowledgements

I would like to express my sincere gratitude to several people who have helped make my education, my research, and this thesis possible. Firstly, I would like to thank Roland Winston for the opportunities to research alongside him, his patience with my work, his encouragement, and for all that he has done for me. I would like to give a posthumous expression of gratitude to Guenter Fischer and Hank Down for their encouragement, wisdom, and humor (“k, so” and “Charlie”). I wish to thank my colleagues and fellow students including Kevin Rico and Heather Poiry for all of their support and quality work. I would like to thank and state my love for my parents who have made it possible for me to be where I am today; I cannot thank them enough. Without all of the support and love from my friends, I probably would have gone insane by now... thank you Mike, Tavia, Georgina, Nicole, and everyone I missed.

I would also like the California Energy Commission, Abengoa Solar, UC MERI, UC Solar, and especially Sarah Kurtz for all of the financial support I received during my graduate studies.

Kevin Balkoski

Table of Contents

Acknowledgements.....	iv
Table of Contents.....	v
List of Figures	vii
List of Tables	x
1. Introduction	1
1.1. Fundamentals Solar Energy	2
1.1.1. Physics of Solar Thermal Energy	3
1.1.2. Sun-Earth Geometry	7
1.2. Solar Concentration.....	10
1.2.1. Nonimaging Optics	10
1.2.2. Benefits of Concentration for Solar Thermal Collectors	11
1.3. Solar Thermal Designs	12
2. XCPC Designs.....	19
2.1. Components.....	19
2.1.1. Evacuated tube	19
2.1.2. Reflector.....	26
2.2. Concentrator Designs	29
2.2.1. North-South.....	29
2.2.2. East-West	30
2.3. Collectors	31
3. Models	32
3.1. Optical Models	32
3.1.1. Procedures.....	33
3.1.2. Results and Discussion	38
3.2. Thermal Models	41
3.2.1. Bulk Model Setup	42
3.2.2. Finite Model Setup (Counter-flow Tube)	45
3.3. Combined Model Results	48
3.3.1. On-Axis Efficiency	48
3.3.2. Temperature Profile of Tube.....	48
4. Experiment.....	50
4.1. Methodology	50

4.1.1.	Description of Facilities	50
4.1.2.	Test Protocols.....	52
4.2.	Results	57
4.2.1.	North-South Counterflow with Alanod Collector.....	57
4.2.2.	East-West Counterflow with Alanod Collector	62
4.2.3.	North-South U-Tube with Alanod Collector	65
4.2.4.	East-West U-Tube with Alanod Collector	68
4.2.5.	East-West X-Tube with Alanod Collector	71
4.2.6.	North-South U-Tube with Reflectech Collector	74
4.2.7.	East-West U-Tube with Reflectech Collector.....	78
4.2.8.	Summary of Results	82
4.3.	Discussion	82
4.3.1.	North-South Counterflow with Alanod	82
4.3.2.	East-West Counterflow with Alanod	84
4.3.3.	Comparison between North-South and East-West Counterflow with Alanod collectors.....	85
4.3.4.	Improvements to North-South Collector (U-Tube and Reflectech)	86
4.3.5.	Improvements to East-West Collector (X-Tube, U-Tube, and Reflectech).....	88
4.3.6.	Possible errors	92
5.	Conclusions and Recommendations	94
	APPENDIX A: Spec Sheets.....	96
	APPENDIX B: Code	103
	References	107

List of Figures

Figure 1. Examples of addressable applications for solar thermal	1
Figure 2. Prototype collector.....	2
Figure 3. Blackbody emissive power as a function of wavelength.....	4
Figure 4. Solar irradiation on Earth	5
Figure 5. Absorption, reflection, and transmission by a slab.....	6
Figure 6. Selective surfaces	7
Figure 7. Sun-Earth geometry.....	8
Figure 8. Sun's directions in cosine space	8
Figure 9. Concentrator	10
Figure 10. FAFCO unglazed flat plate collectors	12
Figure 11. SunEarth glazed flat plate collector	13
Figure 12. Apricus evacuated tube collector	13
Figure 13. Apricus heat pipe tube	14
Figure 14. Parabolic trough collector	15
Figure 15. AREVA Solar linear Fresnel system	16
Figure 16. Solar tower	17
Figure 17. Sopogy parabolic trough collector	18
Figure 18. Chromasun linear Fresnel collector	18
Figure 19. U-Tube evacuated tube.....	19
Figure 20. Close-up of evacuated tube	20
Figure 21. Corning Pyrex 7740 transmittance	21
Figure 22. Transmittance testing setup	21
Figure 23. Borosilicate Glass Tube Transmittance	22
Figure 24. Counter-flow tube dimensions	23
Figure 25. X-tube dimensions.....	24
Figure 26. U-tube dimensions.....	25
Figure 27. Structure of Alanod MIRO-SUN	26
Figure 28. Total spectral reflectance of Alanod MIRO-SUN provided by Alanod Solar	27
Figure 29. Measured reflectance of Alanod reflective surfaces	27
Figure 30. Rolls of Reflectech film.....	28
Figure 31. Spectral reflectance of Reflectech and Alanod	29
Figure 32. Cross section of North-South design.....	30

Figure 33. Cross section of East-West design	30
Figure 34. Advanced scattering model as defined by LightTools	32
Figure 35. LightTools Advanced Scattering Model properties window.....	33
Figure 36. Emittance properties of source in LightTools	35
Figure 37. AM 1.5 spectrum used for simulations.....	35
Figure 38. East-West model in LightTools.....	36
Figure 39. Top view of North-South model.....	36
Figure 40. Off-axis simulation in LightTools	37
Figure 41. Ray-tracing for North-South Reflectech collectors	39
Figure 42. North-South Modeled IAM Chart	39
Figure 43. Ray-tracing for East-West Alanod collectors.....	40
Figure 44. East-West Modeled IAM Charts	41
Figure 45. Heat balance at glass	43
Figure 46. Heat balance at the absorber.....	44
Figure 47. Heat gained by fluid	44
Figure 48. Modeled on-axis efficiencies of Counter-flow tube collectors	48
Figure 49. Modeled temperature profile for North-South counter-flow.....	49
Figure 50. Modeled temperature profile for East-West counter-flow	49
Figure 51. Schematic of test site	50
Figure 52. North-South Counterflow with Alanod Effective Raw Efficiency Curve.....	58
Figure 53. North-South Counterflow with Alanod Effective Reduced Efficiency Curve.....	59
Figure 54. North-South Counterflow with Alanod Direct Reduced Efficiency Curve.....	59
Figure 55. North-South Counterflow with Alanod: IAM Chart	60
Figure 56. North-South Counterflow Time Constant Plot.....	61
Figure 57. East-West Counterflow with Alanod Raw Efficiency Curve.....	63
Figure 58. East-West Counterflow with Alanod Effective Reduced Efficiency Curve	64
Figure 59. East-West Counterflow with Alanod Direct Reduced Efficiency Curve	64
Figure 60. North-South U-Tube with Alanod Raw Efficiency Curve	66
Figure 61. North-South U-Tube with Alanod Effective Reduced Efficiency Curve.....	67
Figure 62. North-South U-Tube with Alanod Direct Reduced Efficiency Curve	67
Figure 63. East-West U-Tube with Alanod Raw Efficiency Curve.....	69
Figure 64. East-West U-Tube with Alanod Effective Reduced Efficiency Curve	70
Figure 65. East-West U-Tube with Alanod Direct Reduced Efficiency Curve.....	70
Figure 66. East-West X-Tube with Alanod Raw Efficiency Curve.....	72

Figure 67. East-West X-Tube with Alanod Effective Reduced Efficiency Curve	73
Figure 68. East-West X-Tube with Alanod Direct Reduced Efficiency Curve	73
Figure 69. North-South U-Tube with Reflectech Raw Efficiency Curve.....	75
Figure 70. North-South U-Tube with Reflectech Effective Reduced Efficiency Curve	76
Figure 71. North-South U-Tube with Reflectech Direct Reduced Efficiency Curve	76
Figure 72. Stagnation results for North-South U-Tube with Reflectech	77
Figure 73. East-West U-Tube with Reflectech Raw Efficiency Curve	79
Figure 74. East-West U-Tube with Reflectech Effective Reduced Efficiency Curve	80
Figure 75. East-West U-Tube with Reflectech Direct Reduced Efficiency Curve.....	80
Figure 76. East-West U-Tube with Reflectech: IAM Chart	81
Figure 77. North-South Counterflow with Alanod: Measured vs. Model	83
Figure 78. East-West Counterflow with Alanod: Measured vs. Model.....	85
Figure 79. North-South Collector Efficiency (Effective)	87
Figure 80. North-South Collector Efficiency (DNI)	87
Figure 81. East-West Collector Efficiency (Effective).....	89
Figure 82. East-West Collector Efficiency (DNI)	90
Figure 83. U-Tube Collector Efficiency (Effective).....	91
Figure 84. U-Tube Collector Efficiency (DNI)	91
Figure 85. Performance comparison to commercial products	94

List of Tables

Table 1. Properties of selective coating	22
Table 2. Counter-flow tube dimensions and properties	23
Table 3. X-Tube properties and dimensions	24
Table 4. U-tube pipe dimensions and properties	25
Table 5. North-South design parameters and dimensions	29
Table 6. East-West design parameters and dimensions	30
Table 7. Optical values used in models	38
Table 8. North-South Optical Efficiency Summary	38
Table 9. East-West Optical Efficiency Summary	40
Table 10. Test conditions for efficiency testing.....	53
Table 11. Additional test conditions for testing with calorimeter	53
Table 12. Collector description of North-South Counterflow with Alanod Collector	57
Table 13. Performance Characteristics of North-South Counterflow with Alanod Collector	58
Table 14. Description of East-West Counterflow with Alanod Collector	62
Table 15. Performance Characteristics of East-West Counterflow with Alanod Collector	63
Table 16. Collector Description of North-South U-Tube with Alanod Collector	65
Table 17. Performance Characteristics of North-South U-Tube with Alanod Collector.....	66
Table 18. Description of East-West U-Tube with Alanod Collector.....	68
Table 19. Performance Characteristics of East-West U-Tube with Alanod Collector	69
Table 20. Description of East-West T-Tube with Alanod Collector	71
Table 21. Performance Characteristics of East-West X-Tube with Alanod Collector	72
Table 22. North-South U-Tube with Reflectech Collector	74
Table 23. Performance Characteristics of North-South U-Tube with Reflectech Collector ...	75
Table 24. Stagnation test conditions for North-South U-Tube with Reflectech.....	77
Table 25. Description of East-West U-Tube with Reflectech Collector	78
Table 26. Performance Characteristics of East-West U-Tube with Reflectech Collector	79
Table 27. Performance Summary of All Collectors Based on Effective Irradiation	82
Table 28. Performance Summary of All Collectors Based on Direct Normal Irradiation.....	82
Table 29. Comparison of North-South and East-West Counterflow w/ Alanod collectors.....	86
Table 30. Alanod MIRO90 properties	96
Table 31. Durather 600 properties	96

This Page is Intentionally Left Blank

1. Introduction

Solar energy can be collected and used in a large variety of ways including: passive day-lighting, heating liquids and gasses, or generating electricity. Additionally, many energy sources such as wind, biomass, hydroelectricity, and even fossil fuels originate from the energy provided by the sun [1].

A solar thermal collector is a device that collects and converts sunlight into usable heat. Currently, the vast majority of solar thermal collectors are used to provide hot water at temperatures below 100 °C (212 °F) or steam at 300 °C (572 °F) to generate electricity through a steam driven turbine [1, 2]. The temperature range between 100 °C and 300 °C is currently largely ignored by the solar thermal industry despite the large number of possible applications within that range. In the United States alone, over \$800 billion is spent on energy, annually, on applications that could be addressed by a solar thermal system that could provide heat up to 200 °C [3]. Examples of applications and their temperature ranges can be found in Figure 1 below [2, 3].

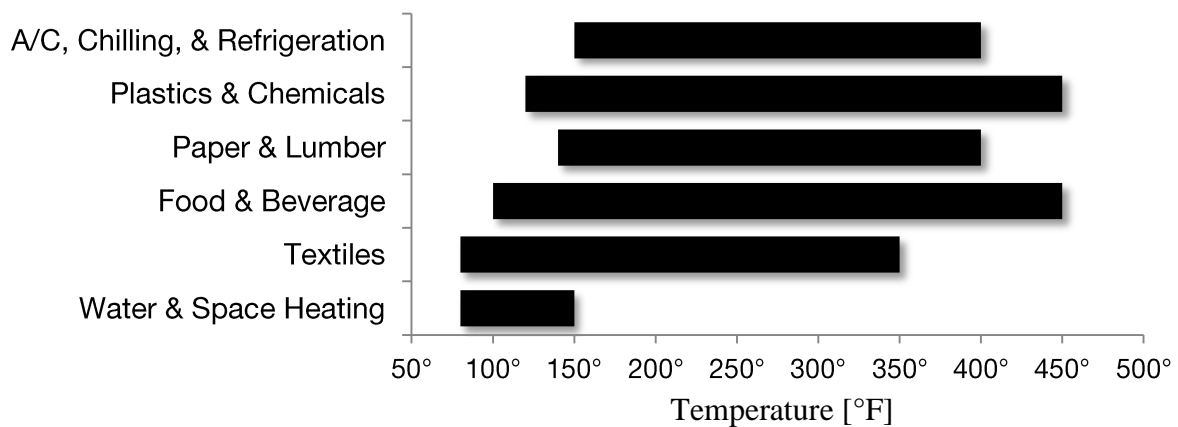


Figure 1. Examples of addressable applications for solar thermal

A likely cause for the lack of adoption of solar thermal for applications between 100 °C and 300 °C is the cost of solar thermal equipment compared to the cost of traditional energy. The solar thermal technologies that currently address temperatures below 100 °C are unable to operate efficiently above 100 °C to warrant the cost of a system. The higher temperature technologies (above 300 °C) require very large-scale projects (above 30 MW_{th})¹ to drive the

¹ The subscript “th” is used to make the distinction between thermal and electric power. The subscript “e” is used to denote electric power.

cost down while most users of applications below 300 °C have a demand of much less than 30 MW_{th}.

This thesis is a part of the ongoing work at UC Merced to develop and apply solar thermal systems capable of efficiently providing temperatures of up to 200 °C. Additionally, the research has been focused on designs that do not require the need of solar tracking in an effort to reduce costs and ultimately allow the technology to be adopted (prototype shown in



Figure 2. Prototype collector

Figure 2). Much of the research done for this thesis was carried out as part of a California Energy Commission grant project (CEC-500-05-021) [4]. Projects by Alfonso Tovar and Jesus Cisneros at UC Merced were also done as part of the grant to develop optical and thermal models of several concepts [5, 6].

Structure of Thesis

Chapter One provides the reader with some of the fundamentals of solar energy, descriptions of sun-Earth geometric relationships, basics of solar thermal systems, and a general understanding of the application of non-imaging optics to develop stationary solar thermal collectors. Chapter Two describes the designs of the External Compound Parabolic Concentrators (XCPC), their components, and properties. Chapter Three describes optical and thermal models of the designs and their results. Chapter Four describes the experiment performed on several designs including its objective, methodology and results. Chapter Five provides the reader with concluding remarks and recommendations by the author.

1.1. Fundamentals of Solar Energy

To effectively take advantage of solar energy, one must first understand the physics that describe the sun as an energy source. Additionally, the same physics that describe the emission of the energy by the sun can be used to understand the collection of the energy by a physical device (i.e. solar collector). In this section, the basics of thermal radiation, solar

radiation, and radiative properties of real surfaces will be explored to give the reader a foundation for much of the discussion within this thesis.

The knowledge of the position of the sun in the sky throughout each day and throughout the year is needed in order to design and describe a solar collection device. Understanding the extremes of the solar position is of an even greater importance for the design of a stationary solar collector.

1.1.1. Physics of Solar Thermal Energy

Blackbody Radiation

Every medium constantly emits thermal radiation depending on the material's properties and its temperature. The radiative heat flux emitted from a surface is called the total emissive power, E , typically expressed in units of W/m^2 . The spectral emissive power, E_λ [$\text{W/m}^2\mu\text{m}$], is used to express the emissive power per wavelength at a given wavelength². The spectral emissive power of an ideal blackbody, $E_{b\lambda}$, can be found by applying Planck's law [7]:

$$E_{b\lambda}(T, \lambda) = \frac{2\pi hc_0^2}{n^2 \lambda^5 (e^{hc_0/n\lambda kT} - 1)}, \quad (n = \text{const}), \quad (1.1)$$

where:

$c_0 = 2.998(10)^8 \text{ m/s}$ (speed of light in a vacuum),

$h = 6.626(10)^{-34} \text{ Js}$ (Planck's constant),

$k = 1.3807(10)^{-23} \text{ J/K}$ (Boltzmann's constant)

and n is the index of refraction of the transparent medium surrounding the blackbody ($n = 1$ in a vacuum). A chart displaying the spectral emissive power of several black bodies at different temperatures can be found in Figure 3.

The maximum power of any curve can be found by using Wien's displacement law [7]:

$$(n\lambda T)_{\max} = 2898 \mu\text{m K}. \quad (1.2)$$

² Alternatively, the spectral emissive power can be expressed as a function of frequency (E_ν) or wave number (E_η).

The dashed line in Figure 3 shows the maximum power as a function of wavelength using Wien's displacement law.

To find the total flux radiated from a blackbody, one must integrate Planck's law over all wavelengths [7]:

$$E_b(T) = \int_0^{\infty} E_b(T, \lambda) d\lambda = n^2 \sigma T^4 \quad (1.3)$$

where $\sigma = 5.670(10)^{-8} \text{ W/m}^2\text{K}^4$. Equation (1.3) above is known as the Stefan-Boltzmann law.

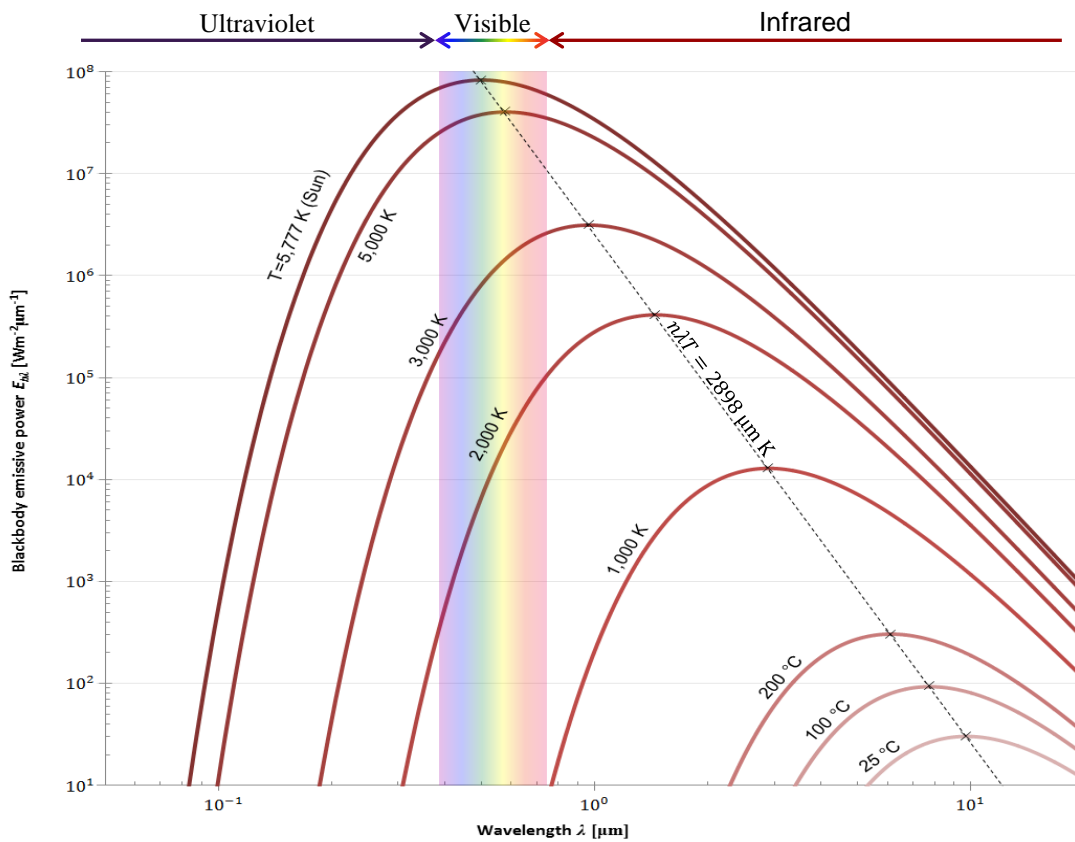


Figure 3. Blackbody emissive power as a function of wavelength

The emissive power of a surface gives the total radiation emitted in all directions. To understand the radiation emitted in a given direction, one must find the radiative intensity, I . The spectral blackbody intensity has the following relationship with the spectral blackbody emissive power [7]:

$$I_{b\lambda}(\mathbf{r}, \lambda) = E_{b\lambda}(\mathbf{r}, \lambda)/\pi, \quad (1.4)$$

where \mathbf{r} is a position vector. For perfectly diffuse surfaces, Lambert's cosine law defines the relationship between emissive power as a function of the angle of incidence (i) and the radiative intensity [1, 7]:

$$E'_{b\lambda}(\mathbf{r}, \lambda, i) = I_{b\lambda}(\mathbf{r}, \lambda) \cos i. \quad (1.5)$$

Solar Radiation

The sun is a large gaseous sphere in space emitting thermal radiation approximating a blackbody with a temperature of 5777 K (see Figure 4) [7]. With Earth located roughly $1.5(10)^{11}$ meters from the sun, its atmosphere intercepts a solar flux of $1,367 \text{ W/m}^2$ [1, 7].

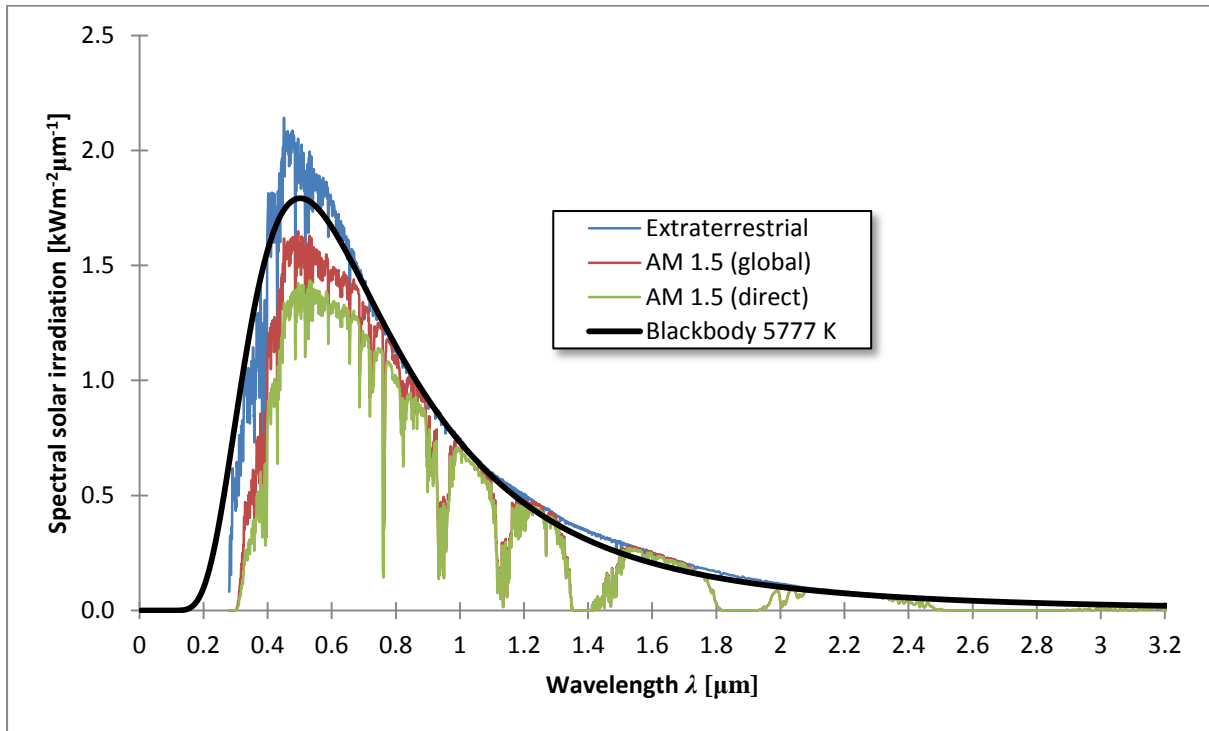


Figure 4. Solar irradiation on Earth [8]

The available solar energy on Earth's surface is less than outside of the atmosphere due to the fact that the media in the atmosphere absorb and reflect incoming radiation at different spectral bands, as can be seen in Figure 4. The total loss due to the atmosphere is dependent on the length of the path that the sunlight must travel. The American Society for Testing and Materials (ASTM) has specified a standard for the spectral irradiance on Earth for the solar industry based on an "air mass" of 1.5 (AM1.5). Air mass is defined by [5]:

$$AM = \frac{1}{\cos z}, \quad (1.6)$$

where z is the solar zenith angle, as defined later in Equation (1.13). ASTM provides spectra for a direct irradiation and for global irradiation on a surface tilted South at latitude. Figure 4 shows the AM1.5 spectra compared to the extraterrestrial and blackbody approximated spectra.

Properties of Real Surfaces

All real surfaces emit thermal radiation at a level less than the theoretical blackbody. A non-dimensional property, emittance, is used to describe a surface's ability to emit thermal radiation relative to that of a blackbody at the same temperature [7, 9]:

$$\epsilon(T) = \frac{E(T)}{E_b(T)}. \quad (1.7)$$

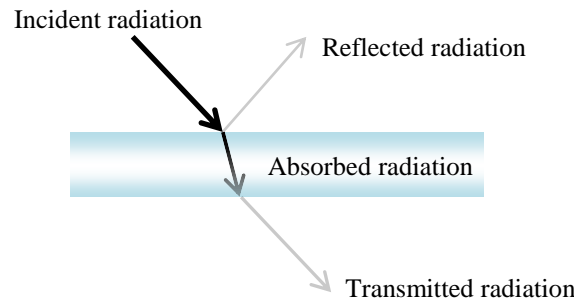


Figure 5. Absorption, reflection, and transmission by a slab

All incident radiation onto a real surface must be reflected, absorbed, and/or transmitted by the medium, as shown in Figure 5. Three non-dimensional radiative properties describe the fraction of the incident radiation that is reflected, absorbed, and transmitted: reflectance, ρ ; absorptance, α ; and transmittance, τ , respectively. By the first law of thermodynamics, the sum of these properties must be exactly one:

$$\rho + \alpha + \tau = 1. \quad (1.8)$$

By Kirchhoff's law, it is known that the absorptance of a body is equal to its emittance at the same wavelength:

$$\alpha(\lambda) = \epsilon(\lambda). \quad (1.9)$$

Selective Surfaces

Ideally, for a solar thermal collector, the absorbing material would be perfectly absorbing throughout the solar spectrum while emitting nearly no radiation throughout the spectral range of a blackbody at the temperature of the absorber. Unfortunately, no surface can have

these ideal properties. This is due, in part, to the fact that the solar spectrum and the spectrum emitted by the absorber have an overlapping section, as can be seen in Figure 6, and that the absorptance and emittance of a surface are equal (1.1). Additionally, the absorptance/emittance curves of a real surface are continuous and do not have a sharp step at the desired wavelength.

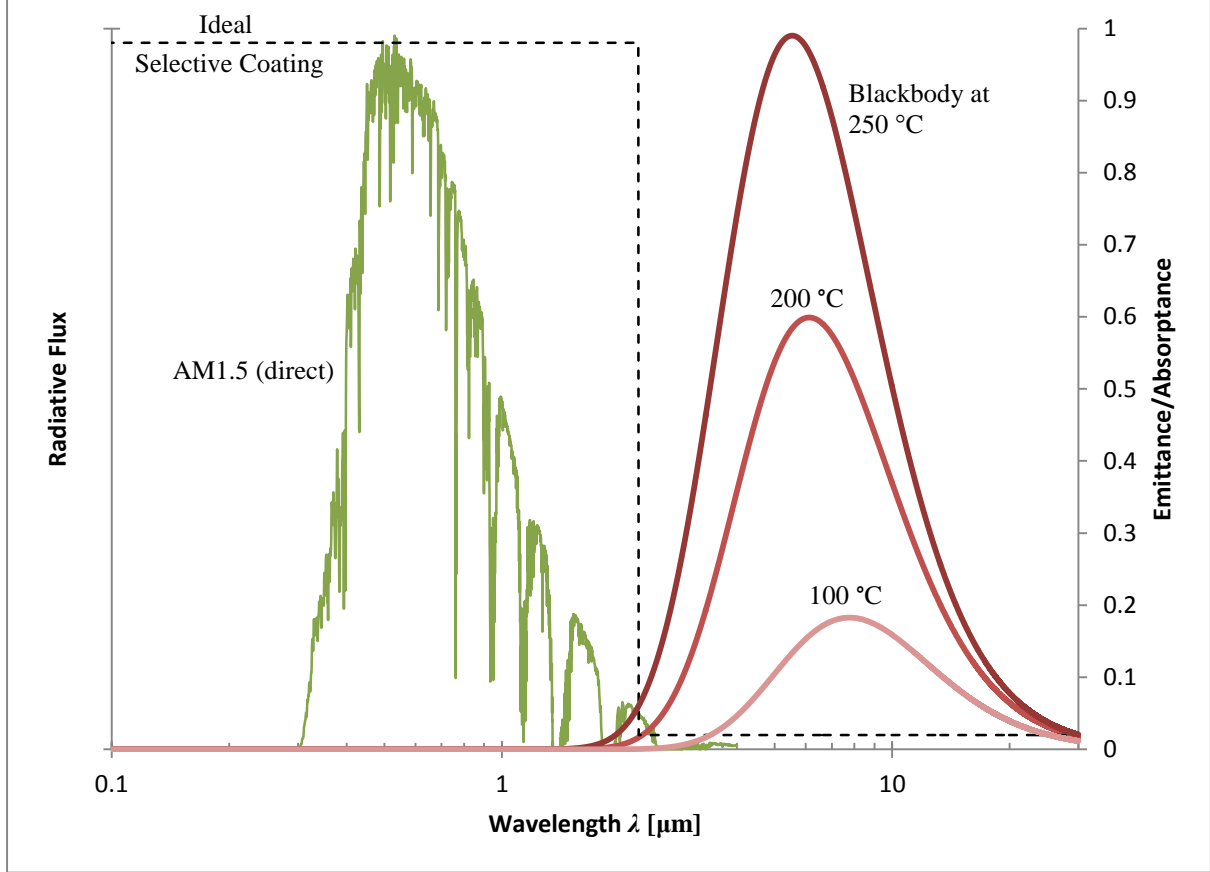


Figure 6. Selective surfaces

As can be seen in Figure 6, as the blackbody spectrum increasingly extends into the lower wavelength regions as the temperature increases, it is clear that selective surfaces can be expected to have increased emittance as temperatures increase.

1.1.2. Sun-Earth Geometry

To understand the design of a non-tracking solar concentrator, one must first understand the geometric relationship between the sun and Earth. To begin, a Cartesian coordinate system can be set up fixed at any location on Earth, as shown in Figure 7. The direction of the sun can be represented by the unit vector, \hat{n}_s , pointing from Earth to the sun [10]:

$$\hat{n}_s = (\sin \delta, \cos \delta \sin \omega, \cos \delta \cos \omega), \quad (1.10)$$

where δ and ω are the declination and hour angle, respectively. δ and ω can be found in the following equations [10]:

$$\sin \delta = -\sin 23.45^\circ \cos \left(\frac{360^\circ(n + 10)}{365.25} \right), \quad (1.11)$$

$$\omega = \frac{360^\circ}{24} t, \quad (1.12)$$

where n is the day of the year starting from January 1st and t is the hour counted from noon with its sign being positive after noon and negative before noon.

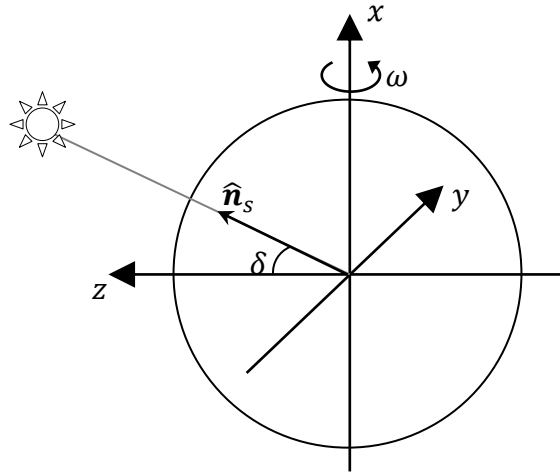


Figure 7. Sun-Earth geometry

Let the corresponding direction cosines for x and y be L and M , respectively. Now the direction of the sun can be described in direction cosine space by a point $(\sin \delta, \cos \delta \sin \omega)$. The direction of the sun over the course of a year is plotted in cosine space in Figure 8.

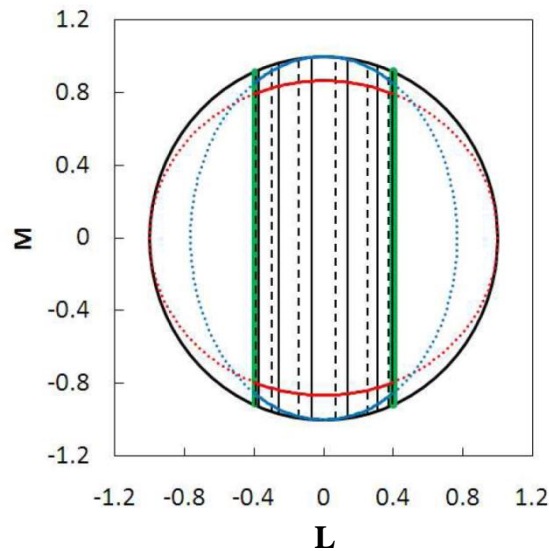


Figure 8. Sun's directions in cosine space [30]

It is also useful to understand the solar zenith angle (z) and solar altitude angle (α_s) for a local position. The solar zenith angle is the angle between the sun and the normal of the Earth's surface at the local position while its complimentary angle is the altitude angle, $z = 90^\circ - \alpha_s$. The solar altitude angle can be found with the following equation [1]:

$$\sin \alpha_s = \sin \phi \sin \delta + \cos \phi \cos \delta \cos \omega, \quad (1.13)$$

where ϕ is the latitude of the local position with positive values above the equator and negative values below the equator.

The angle between the South at the local position and the angle of the sun projected on the surface of the Earth is known as the solar azimuth angle, a_s , and can be found using the following equation [1]:

$$\sin a_s = \frac{\cos \delta \sin \omega}{\cos \alpha_s}. \quad (1.14)$$

Typically, one needs to define the position of the sun relative to a surface tilted by β from the ground and facing directly South (i.e. a solar collector). Specifically, the angle of incidence, i , is of importance due to Lambert's cosine law as described in Equation (1.5). The angle of incidence can be found from the following equation [1]:

$$\cos i = \cos \alpha_s \cos a_s \sin \beta + \sin \alpha_s \cos \beta. \quad (1.15)$$

1.2. Solar Concentration

The concentration of light from entrance aperture area, A (Figure 9), to an exit aperture, A' , can be defined as follows [10, 11, 12]:

$$C = \frac{A}{A'}. \quad (1.16)$$

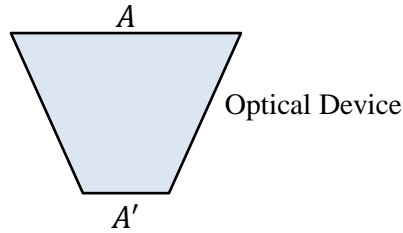


Figure 9. Concentrator

In the following sections, the theoretical maximum concentration will be defined in addition to the benefits of using concentration for solar thermal collectors.

1.2.1. Nonimaging Optics

Nonimaging Optics is the theory of thermodynamically efficient optics and as such depends more on thermodynamics than on optics. A few observations suffice to establish the connection. As can be seen in Figure 4, the solar spectrum fits a black body at 5777 K. The well-known Stefan-Boltzmann law, which also follows from thermodynamics, relates temperature to radiated flux so that the solar surface flux is $\Phi_s \sim 58.6 \text{ W/mm}^2$ while the measured flux at top of the earth's atmosphere is $\sim 0.137 \text{ mW/mm}^2$ [11]. That the ratio, $\sim 44,000$, coincides with $1/\sin^2 \theta_s$ where θ_s is the angular subtense of the sun and is not a coincidence but rather illustrates a deep connection between the two subjects (the sine law of concentration) [11]. Nonimaging Optics is also a design approach that departs from the methods of traditional optical design to develop techniques for maximizing the collecting power of concentrator and illuminator systems. Nonimaging devices substantially outperform conventional imaging lenses and mirrors in these applications, approaching the theoretical (thermodynamic) limit.

This new way of looking at the problem of efficient concentration depends on probabilities, the ingredients of entropy and information theory while “optics” in the conventional sense recedes into the background. The design principle maximizes the probability that radiation

starting at the receiver would be directed to a specific band in the sky we wish to accept. Such are the principles and methods of design adopted in this thesis.

For non-rotationally symmetric designs, the theoretical limit to the concentration can be simplified to [11]:

$$C_{max} = \frac{1}{\sin \theta_s}. \quad (1.17)$$

For stationary collectors, one must understand sun-Earth geometry and decide on the daily and seasonal limits to impose on the design.

1.2.2. Benefits of Concentration for Solar Thermal Collectors

The efficiency of a solar thermal collector, η , can be defined as the ratio of the useful flux collected ($q_{collected}$) to the incident solar flux (G):

$$\eta = \frac{q_{collected}}{G}, \quad (1.18)$$

Additionally, the collector efficiency can be described by its optical and thermal losses:

$$\eta = \eta_o - \frac{q_{loss}}{q_{in}}, \quad (1.19)$$

where η_o is the optical efficiency of the collector, q_{in} is the available concentrated solar flux on the receiver, and q_{loss} is the heat loss of the collector. For a solar collector, the optical efficiency can be defined as:

$$\eta_o = \rho_r^{\langle n \rangle} \tau_g \alpha_a (1 - L), \quad (1.20)$$

where ρ_r is the reflectance of the reflector, $\langle n \rangle$ is the average number of reflections on reflector, τ_g is the transmittance of glass envelope, α_a is the absorptance of the absorber in the solar spectrum, and L is the fraction of light lost due to geometric or practical reasons. The concentrated flux, q_{in} , is simply just the product of the collector's concentration and the incident solar flux:

$$q_{in} = CG. \quad (1.21)$$

Assuming that radiative heat loss is the dominant thermal loss³ and that the emittance of the glass envelope, $\epsilon_g(T_a)$, is unity⁴:

$$q_{loss} \cong \sigma(T_a^4 - T_g^4) \times \epsilon_a(T_a), \quad (1.22)$$

where σ is the Stefan-Boltzmann constant, T_a is the surface temperature of the absorber, T_g is the glass temperature, and $\epsilon_a(T_a)$ is the emittance of the absorber as a function of its temperature. Therefore, the total efficiency of a solar thermal collector can be estimated by the following equation:

$$\eta \cong \rho_r^{(n)} \tau_g \alpha_a (1 - L) - \frac{\sigma(T_a^4 - T_g^4) \times \epsilon_a(T_a)}{CG}. \quad (1.23)$$

As can be seen in equation (1.23), there are several factors that contribute to the efficiency of a collector. With the thermal losses increasing with temperature on the order of $\sim T_a^5$, the concentration of the collector becomes an important factor in maintaining its efficiency at higher temperatures.

1.3. Solar Thermal Designs

As stated earlier, most solar thermal technologies are designed to serve either low temperatures ($< 100^\circ\text{C}$) or high temperatures ($> 300^\circ\text{C}$). Below are descriptions of the common technologies currently on the market.

Low Temperature Collectors

There are three main types of low temperature collectors: unglazed flat plate, glazed flat plate, and evacuated tube collectors.

Unglazed flat plate collectors



Figure 10. FAFCO unglazed flat plate collectors [13]

³ This assumptions most valid for concentrating collectors using evacuated tubes

⁴ If this assumption is not made, (1.22), should be $q_{loss} = \sigma(T_a^4 - T_g^4) / [\epsilon_a^{-1} + \epsilon_g^{-1}(1 - \epsilon_g)(R_a/R_g)]$ assuming that the absorber and the glass envelope are concentric cylinders with infinite length

Unglazed collectors (Figure 10) are, by far, the most common type of solar thermal collector in the United States. These collectors are only used for very low temperature applications, such as pool heating, due to their low efficiencies at temperatures above 50 °C. Unglazed collectors generally are made out of uncoated, black PVC. No insulation, frame, or covering are included with these collectors to reduce costs.

Glazed flat plate collectors

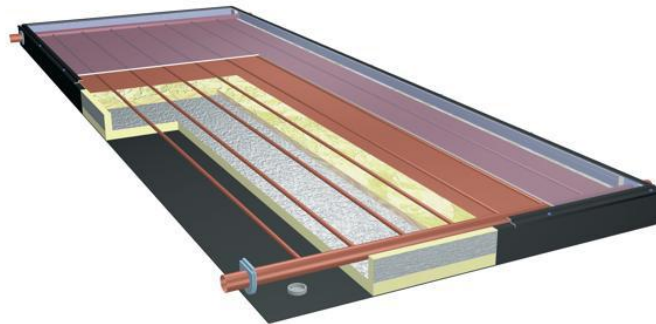


Figure 11. SunEarth glazed flat plate collector [14]

For domestic water heating in the US, glazed collectors are a typical choice. As can be seen in Figure 11, glazed flat plate collectors consist of a metal frame, insulation, copper (sometimes aluminum) absorber plate, copper pipe, and a glass cover. Depending on the manufacturer, different selective coatings are applied to the absorber surface. Due to their simplicity, flat plate collectors generally have high optical efficiencies. Common applications for flat plate collectors include domestic and pool water heating.

Evacuated tube collectors



Figure 12. Apricus evacuated tube collector [15]

Evacuated tube collectors (without concentration) contain an absorbing surface enclosed in an evacuated glass tube (Figure 12). Each evacuated tube consists of two glass tubes made from extremely strong borosilicate glass. The outer tube is transparent allowing light rays to pass through with minimal reflection. The inner tube is coated with a special selective coating. Evacuated tube collectors are very common in China, Israel, Germany, and elsewhere. The evacuated tubes used in these collectors are typically heat pipe tubes with a glass absorber, as can be seen in the example in Figure 13. Additional information on evacuated tubes can be found on page 19.

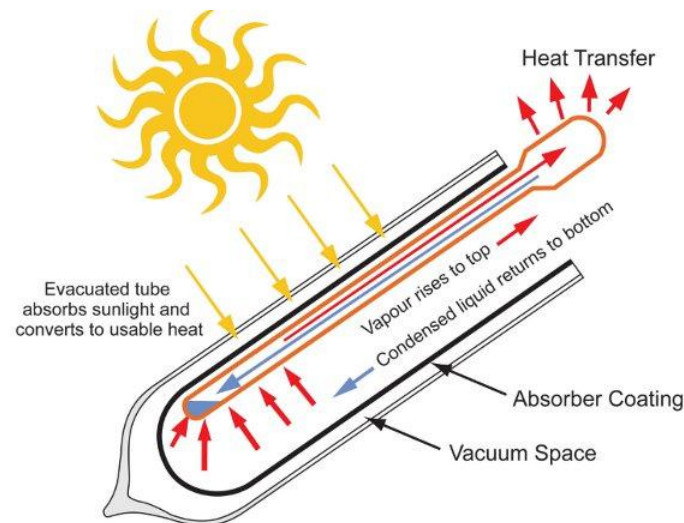


Figure 13. Apricus heat pipe tube [15]

High Temperature Collectors

Three of the most common types of high temperature collectors are the parabolic trough collector, linear Fresnel collector, and the solar tower. All of these high temperature collectors use high concentration and require solar tracking.

Parabolic trough collectors



Figure 14. Parabolic trough collector [16]

Parabolic trough collectors (Figure 14) are generally designed to achieve temperatures between 300 °C to 400 °C, through the use of high concentration ($C > 20$). These collectors consist of large reflectors in the shape of a parabola to concentrate sunlight onto centrally-located high temperature evacuated tubes. The trough is parabolic along one axis and linear in the orthogonal axis. For change of the daily position of the sun perpendicular to the receiver, the trough tilts east to west so that the direct radiation remains focused on the receiver. However, seasonal changes in the in angle of sunlight parallel to the trough does not require adjustment of the mirrors, since the light is simply concentrated elsewhere on the receiver. Thus the trough design does not require tracking on a second axis. A fluid passes through the receiver and becomes very hot. Common fluids are synthetic oil, molten salt and pressurized steam. The fluid containing the heat is transported to a heat engine where about a third of the heat is converted to electricity. Full-scale parabolic trough systems consist of many such troughs laid out in parallel over a large area of land.

Linear Fresnel collectors



Figure 15. AREVA Solar linear Fresnel system [17]

Linear Fresnel Reflector (LFR) and Compact Linear Fresnel Reflector (CLFR) designs use a series of long and flat (or almost flat) mirrors that concentrate sunlight onto one or more central receivers carrying a working fluid. Each mirror independently tracks the sun in order to direct the light onto the receiver as seen in Figure 15. Much like parabolic trough collectors, most LFR and CLFR systems operate above 300 °C and are used to drive steam turbine systems to generate electricity. Smaller versions of the CLFR system have been developed to address the temperature range of 100 °C to 300 °C.

These systems aim to offer lower overall costs by sharing a receiver between several mirrors (as compared with trough concepts), while still using the simple line-focus geometry with one axis for tracking. The LFR differs from that of the parabolic trough in that the absorber is fixed in space above the mirror field. Also, the reflector is composed of many low row segments, which focus collectively on an elevated long tower receiver running parallel to the reflector rotational axis. The receiver is stationary and so fluid couplings are not required (as in troughs). The mirrors also do not need to support the receiver, so they are structurally simpler. When suitable aiming strategies are used (mirrors aimed at different receivers at different times of day), this can allow a denser packing of mirrors on available land area. However, one fundamental difficulty with the LFR technology is the avoidance of shading of incoming solar radiation and blocking of reflected solar radiation by adjacent reflectors. Blocking and shading can be reduced by using absorber towers elevated higher or by increasing the absorber size, which allows increased spacing between reflectors remote from the absorber. Both these solutions increase costs, as larger ground usage is required.

Solar towers



Figure 16. Solar tower [18]

Solar tower systems have large fields of mirrors that concentrate sunlight onto a receiver located on top of a central tower (Figure 16). Each of the mirrors (known as heliostats) tracks the sun in order to direct the light onto the tower's receiver. Within the receiver the concentrated sunlight heats molten salt to over 500 °C. The heated molten salt then flows into a thermal storage tank where it is stored, maintaining 98% thermal efficiency, and eventually pumped to a steam generator. The steam drives a standard turbine to generate electricity.

The advantage of this design above the parabolic trough design is the higher temperature. Thermal energy at higher temperatures can be converted to electricity more efficiently and can be more cheaply stored for later use. Furthermore, there is less need to flatten the ground area. In principle a solar tower can be built on a hillside. Mirrors can be flat and plumbing is concentrated in the tower. The disadvantage is that each mirror must have its own dual-axis control, while in the parabolic trough design one axis can be shared for a large array of mirrors.

Current “Medium Temperature” Collectors

A few companies in the recent past have begun to market their products for medium temperature applications (100 °C to 300 °C). These companies have approached their designs by beginning with a high temperature type design and scaling down and lowering its properties to achieve a lower cost product targeted for medium temperature applications.

Parabolic trough and linear Fresnel are common choices for this scaled-down approach. Examples by Sopogy and Chromasun can be found in Figure 17 and Figure 18.



Figure 17. Sopogy parabolic trough collector [19]

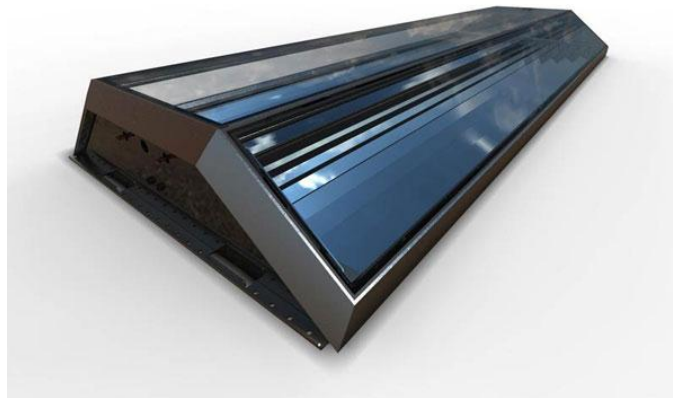


Figure 18. Chromasun linear Fresnel collector [20]

2. XCPC Designs

2.1. Components

The XCPC type collector consists of two primary components: the evacuated tube and the reflector. The evacuated tube serves as a receiver while the reflector effectively concentrates the incoming solar radiation over a wide range of angles.

2.1.1. Evacuated tube

There are several different types of evacuated tubes used in solar thermal collectors. Two of the main types of tubes are the dewar type (all-glass) vacuum tubes and the metal-glass vacuum tubes (Figure 19). Both of these types of tubes have different options for their heat transfer method to a working fluid including thermosyphon, heat pipe, and flow-through.

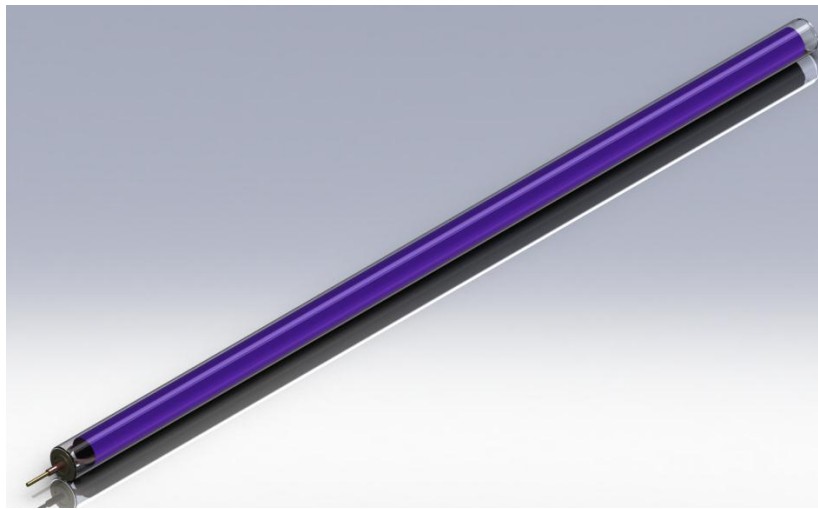


Figure 19. U-Tube evacuated tube

Through the development of the California Energy Commission grant CEC-500-05-021, the metal-glass vacuum tube using flow-through heat transfer was chosen as the best candidate to achieve the grant's goals of reaching 50% efficiency at a cost of \$15/m². Three different tubes were chosen to be developed and tested:

- Counter-flow tube
- X-tube (counter-flow) tube
- U-tube.

Each of these metal-glass vacuum tubes has the following sub-components (Figure 20):

- Glass envelope

- Selective coating and metal absorber
- Copper pipe for fluid transport and manifold connection
- Metal-to-glass vacuum seal.

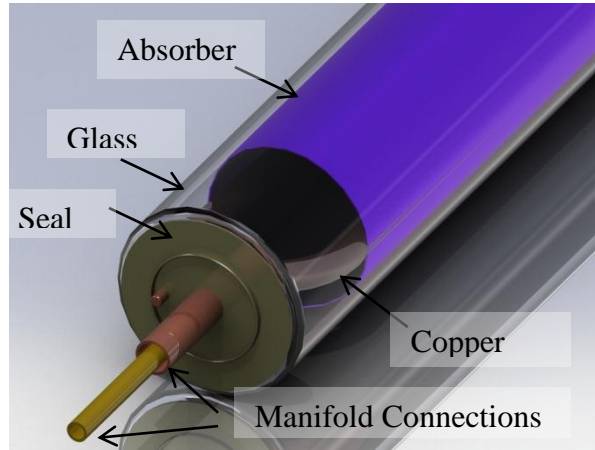


Figure 20. Close-up of evacuated tube

Glass Envelope

The glass envelope (tube) is an evacuated glass cylinder that encloses the absorber and the heat exchanger pipes. The glass should have a high transmittance to allow as much of the incoming solar radiation to pass through and onto the absorber. The vacuum space between the glass and the absorber is intended to eliminate convective heat loss from the absorber to the glass.

The commercially available evacuated tubes that are mass-produced in China use borosilicate glass. Borosilicate glass is a high quality glass with low thermal expansion and excellent solar transmittance. Solar energy absorption within the glass is very small; the optical loss of borosilicate glass is dominated by reflection losses (Fresnel losses) due to the higher index of refraction of glass compared to air. As light passes through a glass cylinder to the absorber surface within it, the light encounters two interfaces: one at the outer surface of the glass and one at the inner surface of the glass. Each interface yields a loss of about 4%, so the total reflectance loss is about 8% [4].

The transmittance of a typical borosilicate glass (Corning 7740) sample is shown in Figure 21.

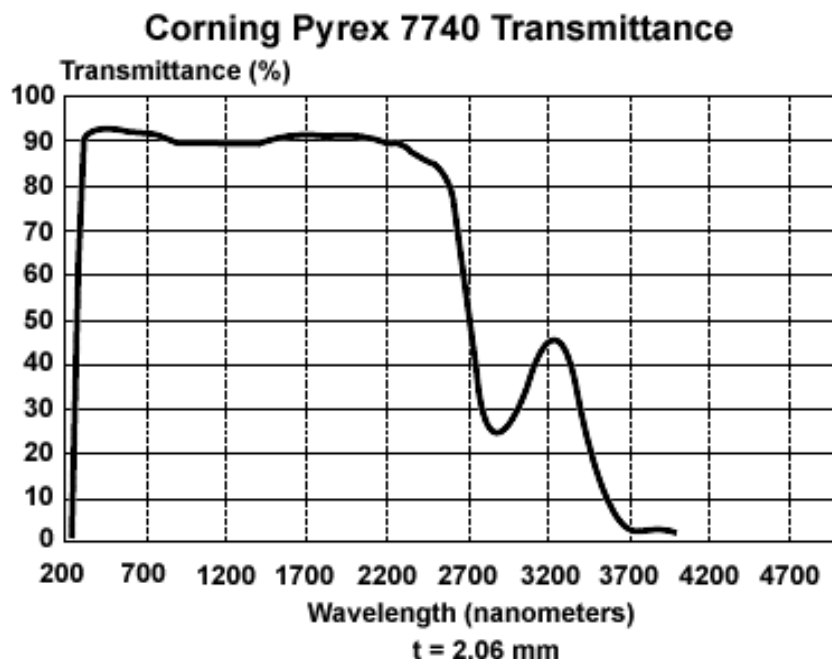


Figure 21. Corning Pyrex 7740 transmittance [4]

To verify that the glass used in the Chinese-manufactured evacuated tubes is of the same quality as Pyrex (Figure 22), samples were taken from a Chinese-manufactured evacuated tube and tested at NREL by Cheryl Kennedy for transmittance with their Perkin-Elmer spectrophotometer [4]. The instrument is pictured in Figure 22a, and a close up of the glass sample, mounted in the instrument, as shown in Figure 22b [4].



Figure 22. Transmittance testing setup

The measured transmittance vs. wavelength is shown in Figure 23. The solar-weighted transmittance, τ_g , was found to be 91.7%.

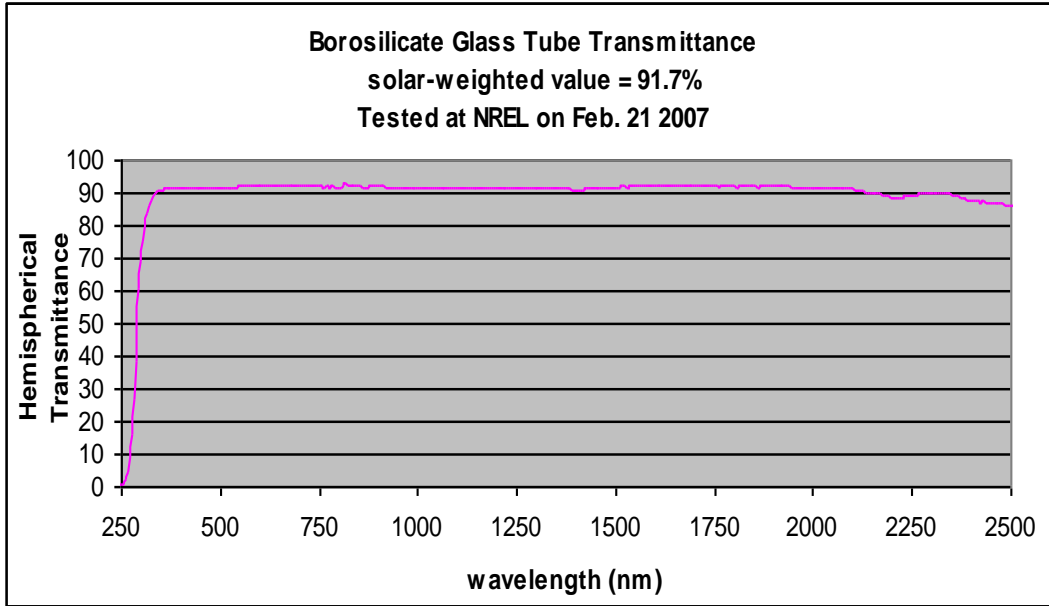


Figure 23. Borosilicate Glass Tube Transmittance [4]

Absorber

The metal absorbers in these metal-glass vacuum tubes are cylindrical that run along the majority of the length of the glass. The surface of the absorber has a vacuum-deposited selective coating to maximize the absorbed solar radiation while minimizing the emitted infrared radiation.

The tubes used in the analyses come from the Chinese tube manufacturer, Eurocon. Eurocon used a custom selective coating on their absorbers. Since the selective coating emittance is a key determinant of the performance of the XCPC collectors, samples were measured at room temperature and 200 °C. Samples were sent to Surface Optics Corporation (SOC) in San Diego to measure the selective properties of the absorber.

The emittance results obtained by SOC for these various selective coatings are provided below in Table 1, along with the solar-weighted absorptance of the coatings. A coatings solar-weighted absorptance is the fraction of the solar spectrum that will be absorbed by the coating.

Table 1. Properties of selective coating [4]

Absorptance, α_A	Emittance (25 °C), ϵ_A	Emittance (200 °C) , ϵ_A
0.902	0.05	0.064

Counter-flow Tube

The counter-flow type tube uses a coaxial copper pipe arrangement as its absorber-to-fluid element as can be seen in Figure 24. The working fluid enters the tube through the inner pipe, flows to the end of the tube, and reverses direction as it travels back to the front of the tube through the annulus between the inner and outer copper pipe.

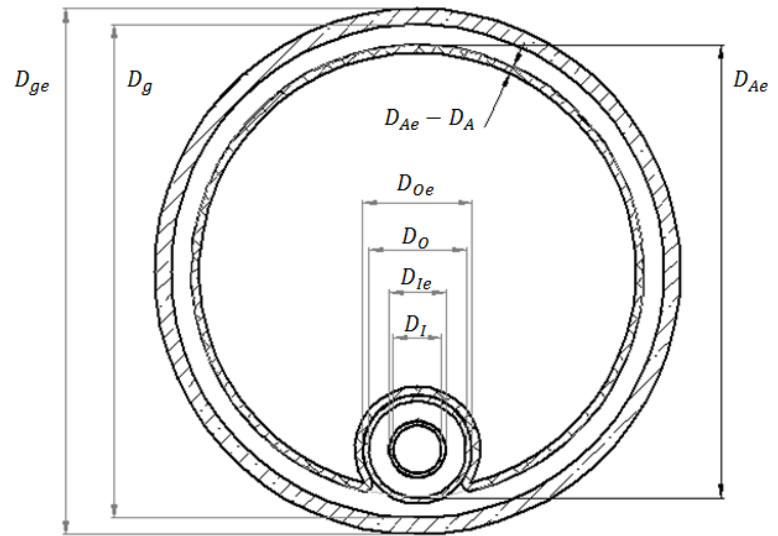


Figure 24. Counter-flow tube dimensions (not to scale)

The outer pipe is in contact with and is welded to the aluminum absorber.

Table 2. Counter-flow tube dimensions and properties [4, 5]

Component	Dimension/Property	Symbol	Value	Unit
Glass envelope	Length	L_g	1,800	mm
	Outer diameter	D_{ge}	65	mm
	Inner diameter	D_g	61.8	mm
	Absorptance	α_g	0.02 (AM 1.5)	
	Transmittance	τ_g	0.90 (AM 1.5)	
	Emittance	ϵ_g	0.85 (IR)	
Absorber	Length	L_A	1,640	mm
	Outer diameter	D_{Ae}	56	mm
	Inner diameter	D_A	54	mm
	Absorptance	α_A (AM 1.5)	0.902	
	Emittance @ 25 °C	$\epsilon_A(25\text{ }^{\circ}\text{C})$	0.05	
	Emittance @ 200 °C	$\epsilon_A(200\text{ }^{\circ}\text{C})$	0.064	
	Thermal conductivity	κ_A	200	W/mK
Coaxial pipe	Outer pipe, OD	D_{Oe}	12	mm
	Outer pipe, ID	D_O	10.5	mm
	Inner pipe, OD	D_{Ie}	8	mm
	Inner pipe, ID	D_I	6	mm
	Hydraulic diameter	D_h	3.5	mm
	Thermal conductivity	κ_{Cu}	320	W/mK

X-Tube

Much like the counter-flow tube, the X-tube uses a coaxial copper pipe arrangement as its absorber-to-fluid element as can be seen in Figure 25. Unlike the counter-flow tube, the outer “pipe” is actually a cylindrical part of the extruded absorber.

Having the aluminum

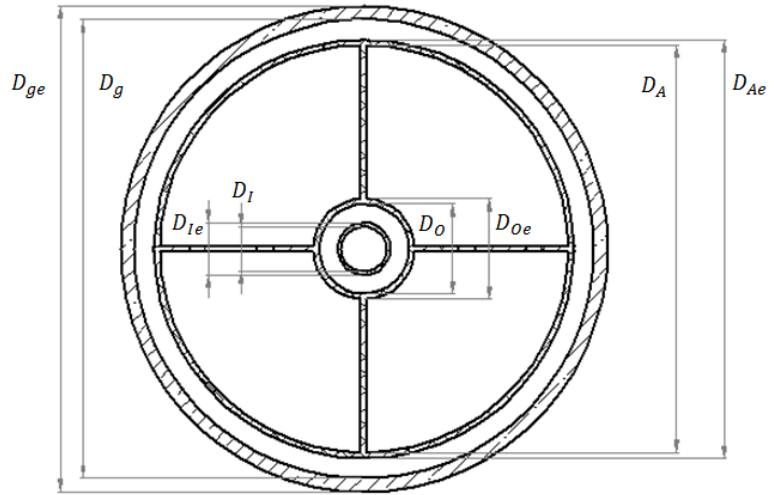


Figure 25. X-tube dimensions

absorber also serving as the outer pipe potentially reduces the thermal resistance from the welds used in the counter-flow tube. The working fluid enters the tube through the inner pipe, flows to the end of the tube, and reverses direction as it travels back to the front of the tube through the annulus between the inner and outer pipe.

Table 3. X-Tube properties and dimensions [4, 5]

Component	Dimension/Property	Symbol	Value	Unit
Glass envelope	Length	L_g	1,800	mm
	Outer diameter	D_{ge}	65	mm
	Inner diameter	D_g	61.8	mm
	Absorptance	α_g	0.02 (AM 1.5)	
	Transmittance	τ_g	0.90 (AM 1.5)	
	Emittance	ϵ_g	0.85 (IR)	
Absorber	Length	L_A	1,640	mm
	Outer diameter	D_{Ae}	56	mm
	Inner diameter	D_A	54	mm
	Absorptance	α_A (AM 1.5)	0.902	
	Emittance @ 25 °C	$\epsilon_A(25\text{ }^{\circ}\text{C})$	0.05	
	Emittance @ 200 °C	$\epsilon_A(200\text{ }^{\circ}\text{C})$	0.064	
	Thermal conductivity	κ_A	200	W/mK
Coaxial pipe	Outer pipe, OD	D_{Oe}	12.5	mm
	Outer pipe, ID	D_O	10.5	mm
	Inner pipe, OD	D_{Ie}	8	mm
	Inner pipe, ID	D_I	6	mm
	Hydraulic diameter	D_h	3.5	mm
	Thermal conductivity	κ_{Cu}	320	W/mK

U-Tube

The U-tube has a much simpler pipe configuration than the counter-flow and the X-type tubes: a single copper pipe runs from the front of the tube to the back where there is a gradual 180° bend to return the pipe to the front of the tube. The pipe is in contact with and is welded to the

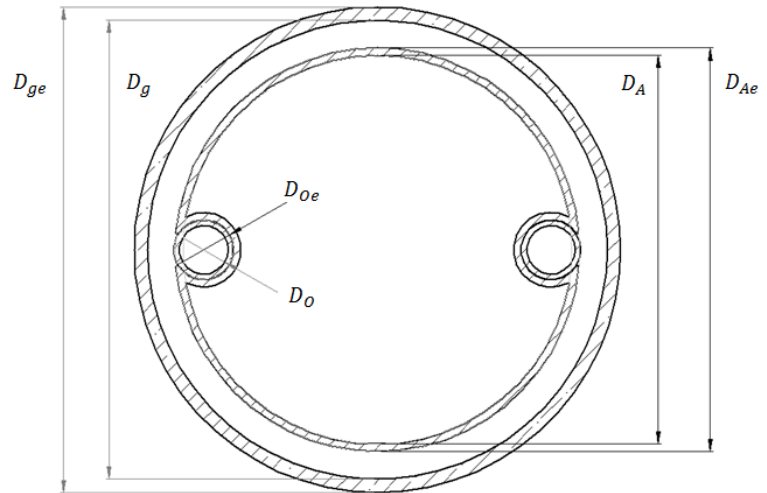


Figure 26. U-tube dimensions

The single pipe is used in place of the coaxial design to increase the performance by doubling the pipe's connection points with the absorber (welds and surface contact) while also preventing the thermal short-circuit introduced by the counter-flow type designs.

Table 4. U-tube pipe dimensions and properties [4, 5]

Component	Dimension/Property	Symbol	Value	Unit
Glass envelope	Length	L_g	1,800	mm
	Outer diameter	D_{ge}	65	mm
	Inner diameter	D_g	61.8	mm
	Absorptance	α_g	0.02 (AM 1.5)	
	Transmittance	τ_g	0.90 (AM 1.5)	
	Emittance	ϵ_g	0.85 (IR)	
Absorber	Length	L_A	1,640	mm
	Outer diameter	D_{Ae}	56	mm
	Inner diameter	D_A	54	mm
	Absorptance	α_A (AM 1.5)	0.902	
	Emittance @ 25 °C	$\epsilon_A(25\text{ °C})$	0.05	
	Emittance @ 200 °C	$\epsilon_A(200\text{ °C})$	0.064	
	Thermal conductivity	κ_A	200	W/mK
Copper Pipe	Outer pipe, OD	D_{Oe}	8	mm
	Outer pipe, ID	D_O	6.5	mm
	Thermal conductivity	κ_{Cu}	320	W/mK

2.1.2. Reflector

The reflector is a reflective surface with its profile in the prescribed shape. The reflective properties of the reflector in the solar spectrum are an important factor in determining the performance of any solar concentrator design.

Two different reflector types were used in the analyses: polished aluminum and metalized (silver) polymer film. Alanod MIRO-SUN 90 was used for the polished aluminum designs and Reflectech was used for the film based designs. These two materials are described in the following sections.

Alanod

Polished aluminum reflectors are generally considered to be the most commercially-available for outdoor solar use. And while polished aluminum is known to lose significant specular reflectance after just 2 to 3 years of outdoor use, Alanod (a German-based company) has made a great deal of technical progress in advancing and improving this approach (Figure 27). Alanod has developed specialized coating techniques that increase the reflectance of their aluminum-based reflective materials, as well as increase outdoor weatherability. Samples of two of Alanod's products were sent to NREL for optical measurement. NREL measured hemispherical reflectance vs. wavelength values is shown in Figure 29 while the manufacturer supplied data can be found in Figure 28.

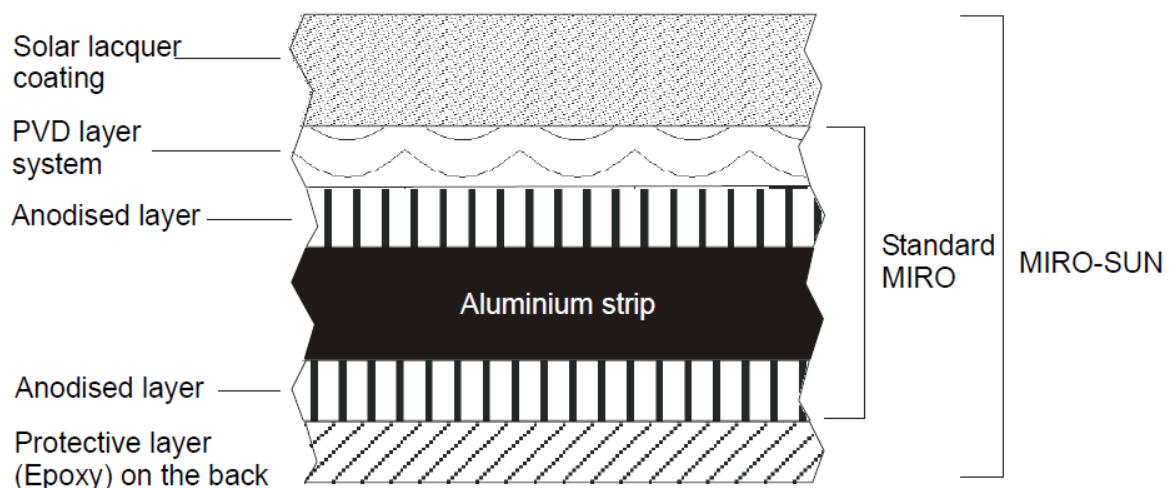


Figure 27. Structure of Alanod MIRO-SUN [4]

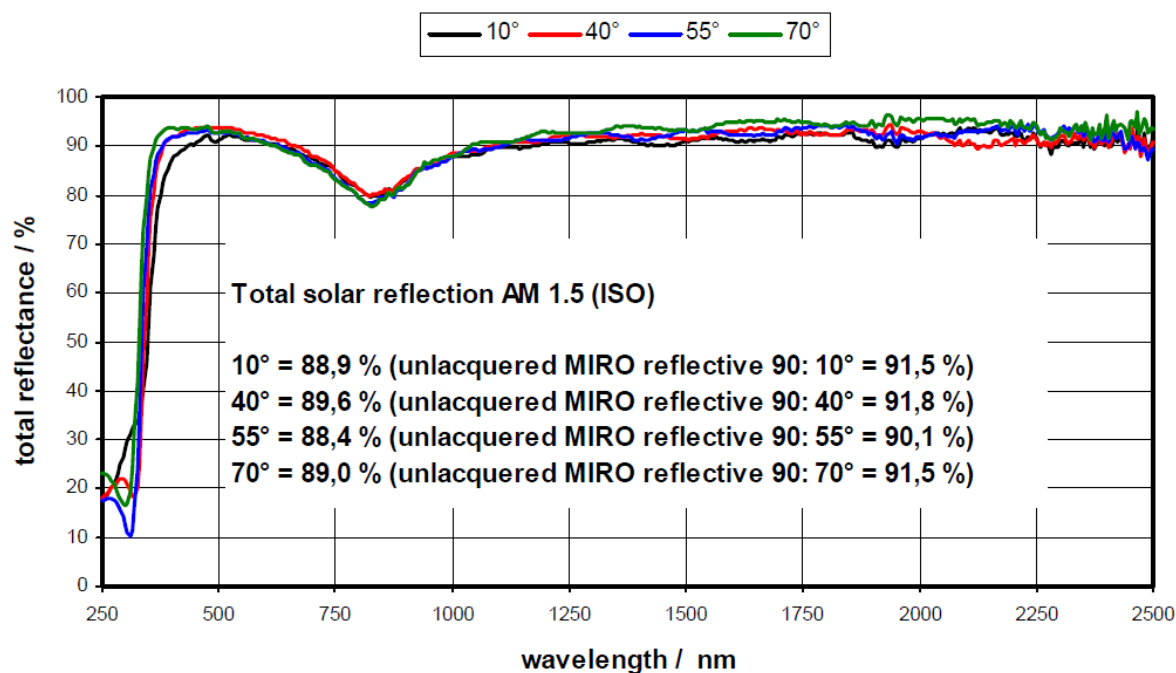


Figure 28. Total spectral reflectance of Alanod MIRO-SUN provided by Alanod Solar [4]

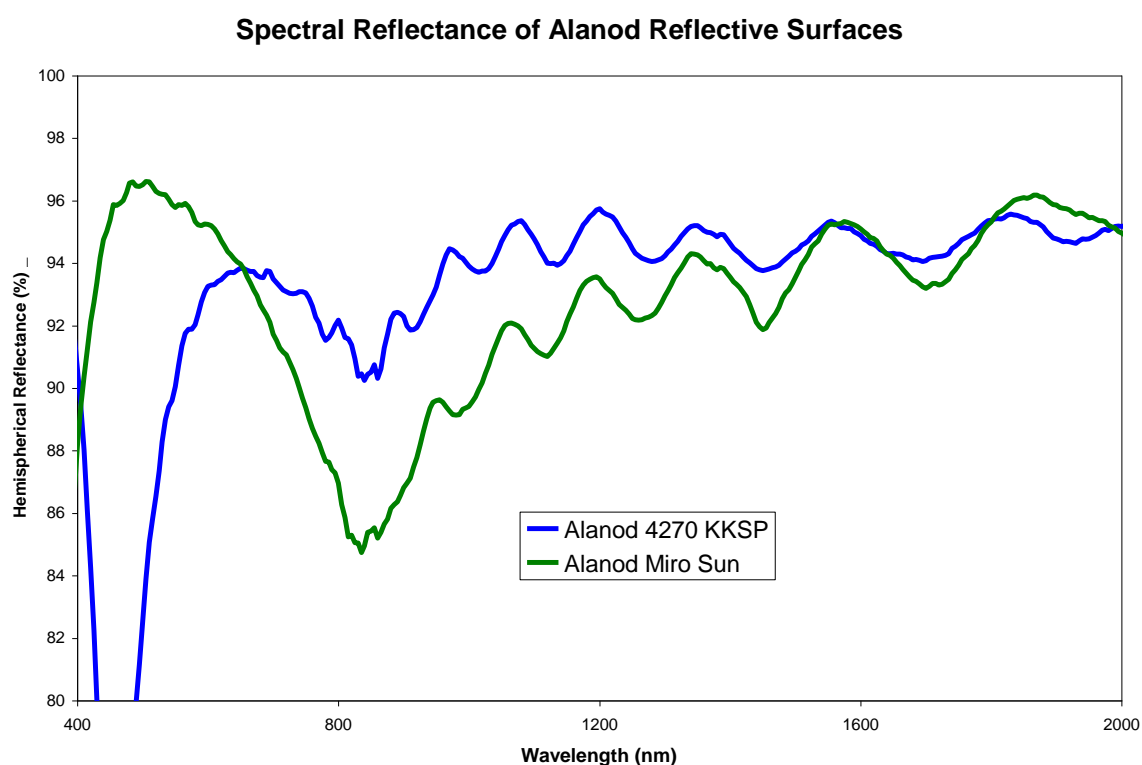


Figure 29. Measured reflectance of Alanod reflective surfaces [4]

Weighting the reflectance values by an airmass-1.5 solar spectrum (AM 1.5) allows determination of the overall hemispherical reflectance for solar thermal applications, since the entire solar spectrum provides useful energy for thermal conversion. The solar-weighted

hemispherical reflectance of Alanod Miro Sun is 91.9% [4]. Hemispherical reflectance includes all reflected light from the sample, regardless of its reflected direction.

Another common way to characterize reflective surfaces is to measure specular reflectance, which excludes reflected light that is scattered, that is, reflected outside a specified acceptance cone angle. The Devices and Services portable specular reflectometer Model 15R provides this measurement, but for a specific wavelength of 660 nm. This instrument was used to measure specular reflectance of both Alanod reflector materials, with the largest acceptance angle (46 milliradians) available on the Model 15R. Alanod MiroSun measured 86% [4]. There is a significant difference between the specular reflectance values at 660 nm and the hemispherical reflectance (also taken at 660 nm), indicating that there is a significant amount of scattering.

The specularity of reflective materials is known to sometimes be affected by material forming operations (such as bending, roll-forming, etc.) since these operations can sometimes alter the front portions of the reflective material. To determine whether this might be the case with Alanod, for the radii needed for our CPC, a virgin piece of flat Alanod was measured with the Devices and Services portable specular reflectometer, then formed/rolled to a radius of 1.12 inches (28 mm).

The formed sheet was then flattened, and measurements were obtained again with the D&S specular reflectometer. These measurements were within 0.1% of the original values, indicating that specular loss is not anticipated to be an issue for the amount of roll-forming required to form the CPC profiles.

Reflectech

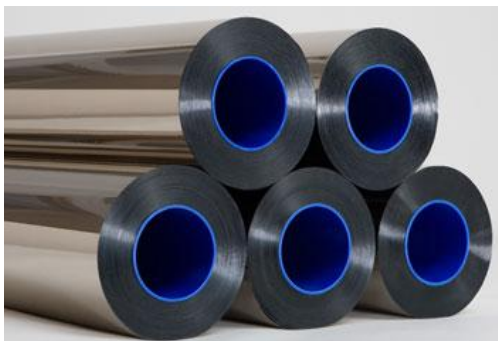


Figure 30. Rolls of Reflectech film [21]

Metallized polymer films are another class of reflective surfaces (Figure 30). A relatively recent silvered film has been developed by NREL and ReflecTech that has recently reached commercial status after years of R&D. The hemispherical reflectance and the specular reflectance (using the D&S) of Reflectech film both exceed 94% [4]. The measured hemispherical reflectance vs. wavelength

values are shown in Figure 31 for Alanod's MIRO-SUN and the Reflectech film. These measurements were obtained at NREL.

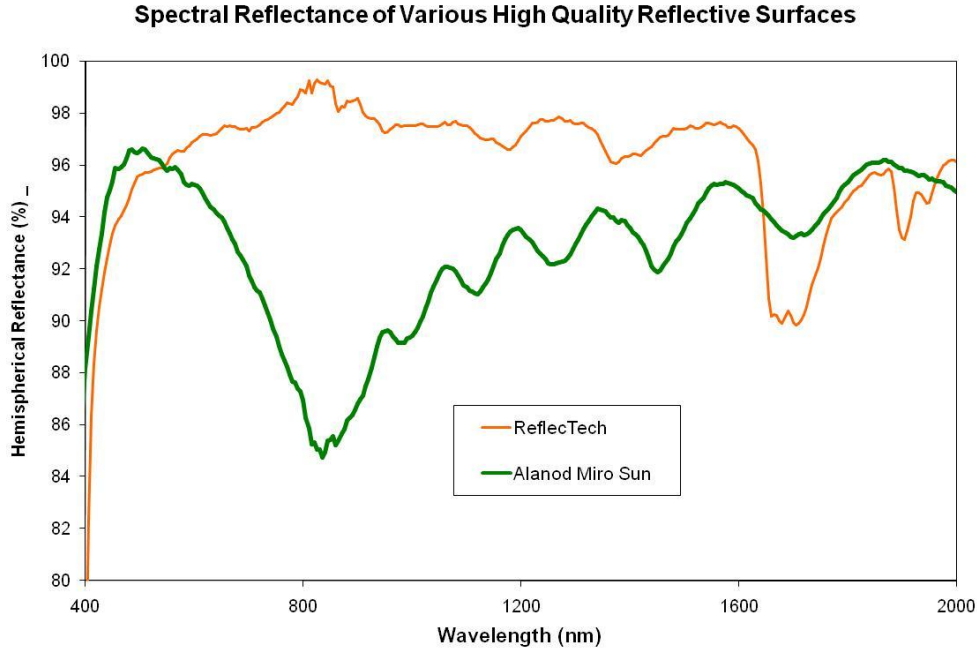


Figure 31. Spectral reflectance of Reflectech and Alanod

2.2. Concentrator Designs

Two different concentrator designs were created: North-South and East-West. Each design is described in the following sections.

2.2.1. North-South

The North-South concentrator was designed to concentrate onto a 56 mm receiver with an acceptance angle of 60° . The resulting design was truncated by 20% to reduce reflector costs. A summary of the design parameters and dimensions can be found in Table 5 and Figure 32.

Table 5. North-South design parameters and dimensions [6]

Receiver diameter, D_{Ae}	56 mm
Acceptance angle, θ_{NS}	60°
Truncation	20%
Concentration, C_{NS}	1.15
Width	201.48 mm
Height	97.04 mm

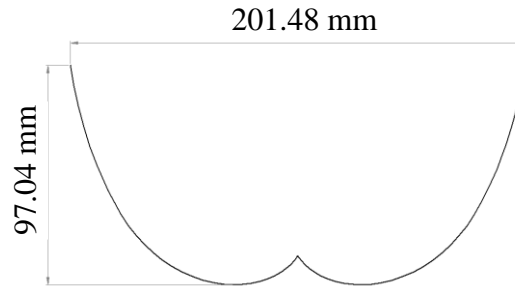


Figure 32. Cross section of North-South design

2.2.2. East-West

The East-West concentrator was designed to concentrate onto a 56 mm receiver with an acceptance angle of 34° . The resulting design was truncated by 20% to reduce reflector costs. A summary of the design parameters and dimensions can be found in Table 6 and Figure 33.

Table 6. East-West design parameters and dimensions [6]

Receiver diameter, D_{Ae}	56 mm
Acceptance angle, θ_{NS}	34°
Truncation	20%
Concentration, C_{NS}	1.179
Width	316.15 mm
Height	260.70 mm

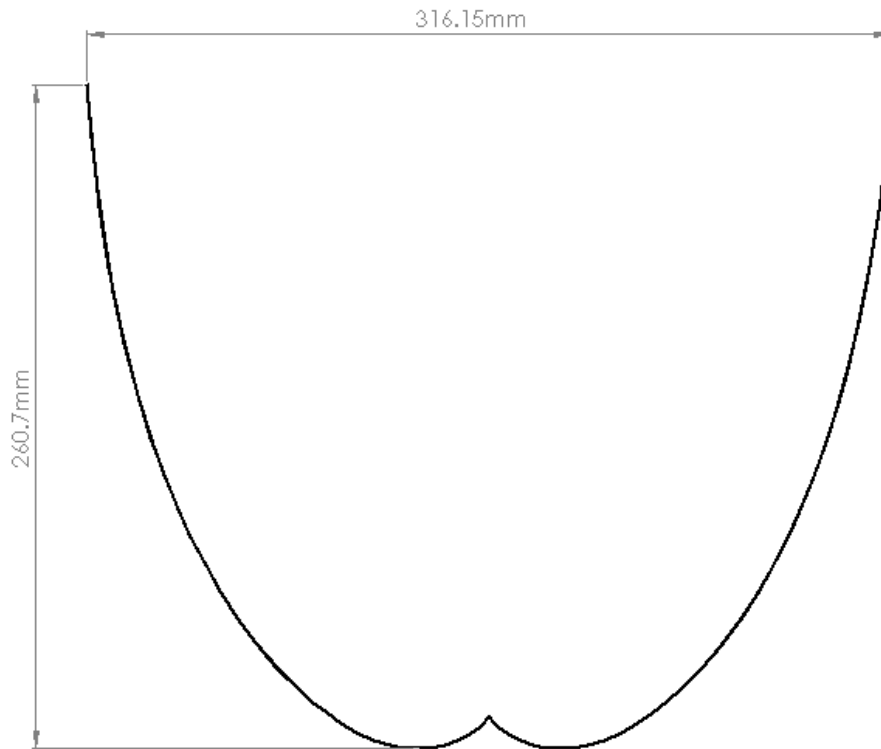


Figure 33. Cross section of East-West design

2.3. Collectors

A total of seven collectors designs have been considered for analysis in this paper:

1. North-South with counter-flow tube with Alanod reflectors (NS AL CF)
2. North-South with U-tube with Alanod reflectors (NS AL UT)
3. North-South with U-tube with Reflectech reflectors (NS RT UT)
4. East-West with counter-flow tube with Alanod reflectors (EW AL CF)
5. East-West with X-tube with Alanod reflectors (EW AL XT)
6. East-West with U-tube with Alanod reflectors (EW AL UT)
7. East-West with U-tube with Reflectech reflectors (EW RT UT)

3. Models

For the sake of simplicity, optical and thermal models were separated. First, optical models were performed on the different designs and evaluated for their efficiencies. Next, thermal models were performed using the optical efficiency values as inputs.

3.1. Optical Models

Optical models were carried out for the four basic configurations: North-South with Alanod Reflectors, North-South with Reflectech Reflectors, East-West with Alanod Reflectors, and East-West with Reflectech Reflectors. In addition to simulations using realistic conditions, models were also created assuming perfect reflective and transmissive properties to gain an understanding of possible optical losses. No additional simulations were conducted to understand the difference between tube types due to the fact that there are only minor differences in the geometry from one type to the other.

Each simulation was carried out using the non-sequential optical modeling software LightTools [22]. LightTools allows the user to build an optical environment and run several different types of simulations to gain an understanding of the optical characteristics of a system. The software performs Monte Carlo simulations to allow the user to do accurate ray-tracing.

Specular and Diffuse Reflection

Different reflection models were used depending on the known material properties for the reflective surfaces. LightTools provides several options to model various levels of specular and diffuse reflection. Each model creating for real materials utilized the advanced scattering model (Figure 34) as can be seen in the example in Figure 35.

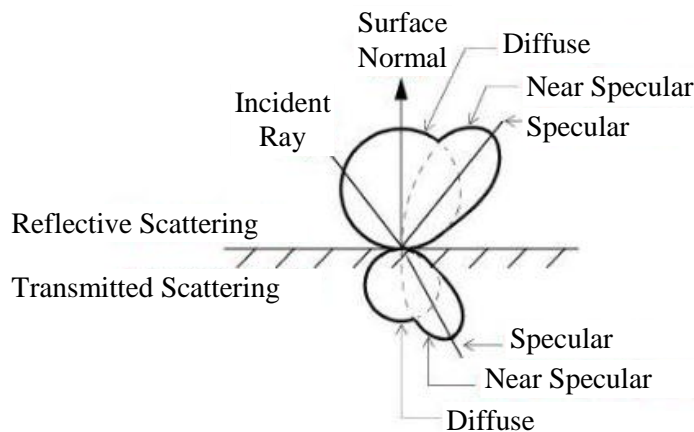


Figure 34. Advanced scattering model as defined by LightTools [22]

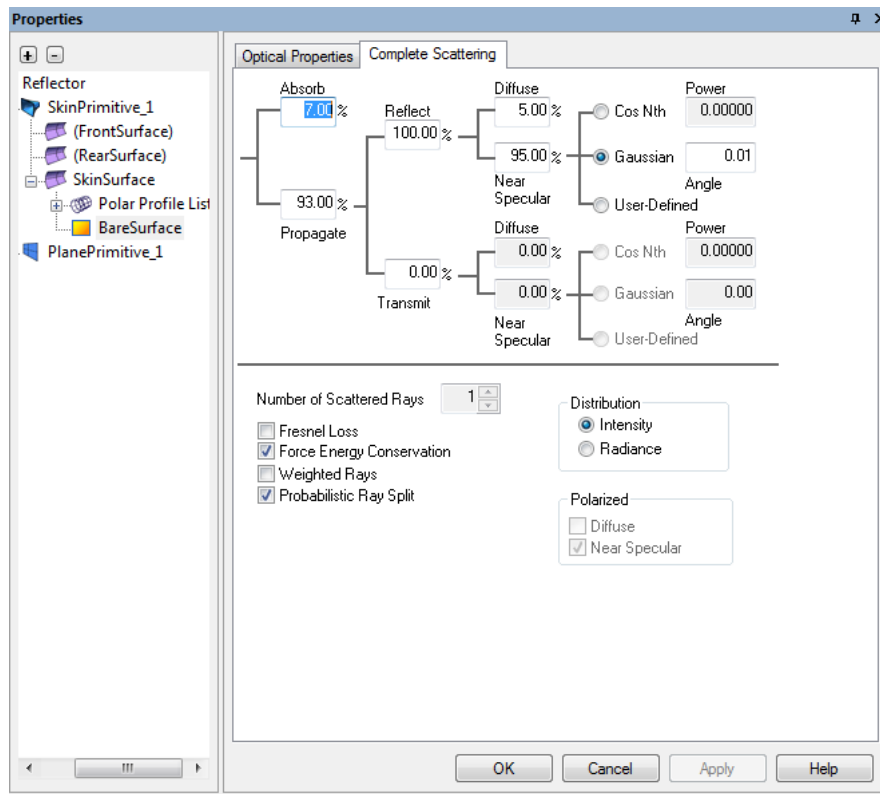


Figure 35. LightTools Advanced Scattering Model properties window

3.1.1. Procedures

Build Model

Each model was built in LightTools using the following procedure:

1. Create new model
2. Create reflector
 - a. Create skinned solid centered on the z-axis
 - b. Toggle “Skin Mode”
 - c. Modify dimensions to match design
 - d. Import profile coordinates
 - e. Assign material to the appropriate type
 - f. Assign optical properties
3. Create glass tube
 - a. Create cylinder centered on the z-axis with the correct length of the glass tube
 - b. Assign the radius to that of the outer radius of the glass tube
 - c. Create an additional concentric cylinder

- d. Assign the radius of the new cylinder to that of the inner radius of the glass tube
 - e. Perform a boolean subtraction
 - f. Assign material to the appropriate type
 - g. Assign optical properties
4. Create absorber
- a. Create cylinder centered on the z-axis with the correct length of the absorber (shorter than the glass tube length) (Figure 38)
 - b. Offset the absorber to the correct position along the optical axis
 - c. Assign the radius to that of the outer radius of the absorber
 - d. Assign material to the appropriate type
 - e. Assign optical properties
 - f. Assign the cylindrical surface as a receiver
5. Create reflective ends
- a. Create a thin rectangular object at the origin
 - b. Assign the height to be that of the reflector height
 - c. Assign the width to be that of the reflector width
 - d. Assign optical properties
 - e. Copy object to the other end of the collector
6. Create solar source
- a. Create rectangular surface emitting source at the aperture height
 - b. Assign the length to be that of the full length of glass tube
 - c. Assign the width to be that of the full width of the aperture
 - d. Assign thickness to be 1mm
 - e. Set the spectral region to AM 1.5 Solar Spectrum (Figure 37)
 - f. Assign the radiometric power to be “1” Watt (Figure 36)
 - g. Assign “Measured Over” to “Aim Region”
 - h. Use default settings for all other “Emittance” properties
 - i. Change the Aim Sphere “Lower Angle” to be the largest angle emitted from the source (0 degrees for a perfectly parallel source, 0.247 degrees for a direct solar source, or 90 degrees when simulating diffuse light)
 - j. Adjust the orientation angles to the desired values
 - k. Assign only the appropriate surface to emit

Immersion	Spectral Region	Spectral Region Chart	Surfaces	Display
Coordinates	Emittance	Aim Sphere	Geometry	Ray Trace
<p>Total Flux/Power</p> <p> <input checked="" type="radio"/> Radiometric Power 1.0000 Watts <input type="radio"/> Photometric Flux 110.31 Lumen </p> <p>Measured Over: Aim Region</p> <p>Ideal Luminance: 5.5933e-007 W/sr.mm²</p> <p>Total Emitting Area: 5.6909e+005 mm²</p> <p> Starting Point Classification <input type="radio"/> Automatic <input type="radio"/> Immersing Element <input checked="" type="radio"/> Semi-automatic </p> <p> <input checked="" type="checkbox"/> Enabled Weight Factor: 1.0000 </p>				

OK Cancel Apply Help

Figure 36. Emittance properties of source in LightTools

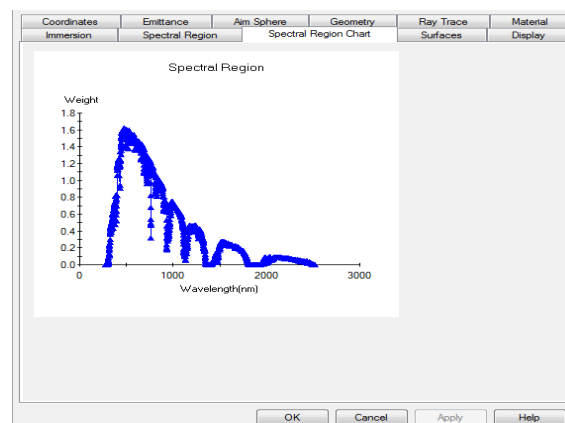


Figure 37. AM 1.5 spectrum used for simulations

7. Create aperture receiver
 - a. Create a “Dummy Surface” at the aperture height (Figure 39)
 - b. Assign the width to that of the full aperture width
 - c. Assign the length to that of the absorber tube length
 - d. Assign the surface to have a receiver

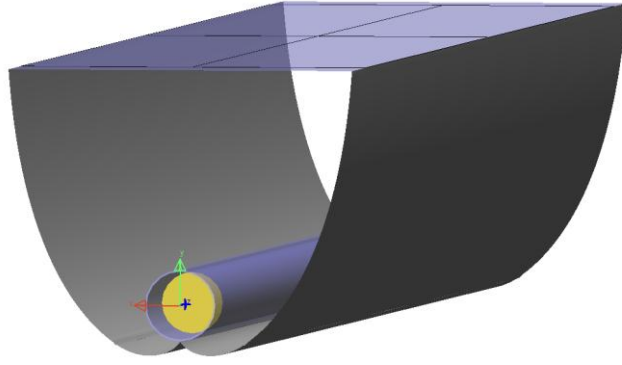


Figure 38. East-West model in LightTools

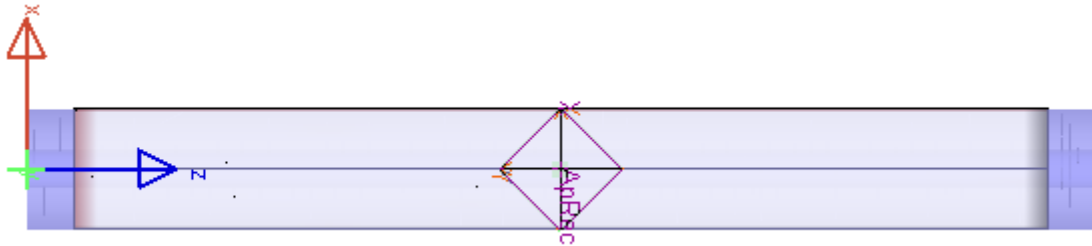


Figure 39. Top view of North-South model

On-axis Simulation Procedure

Each model was simulated for its on-axis performance using the following procedure:

1. Input the desired number of rays to be simulated
2. Assign the “Lower Angle” of the source’s “Aim Sphere” to be 0.247 degrees
3. Assign the orientation angles of the source to be in the negative y-direction
4. Run simulation
5. Calculate the effective efficiency by taking the ratio of the power incident on the absorber and the power incident on the aperture receiver multiplied by the Absorptance of the absorber: $\eta = \frac{P_{abs}}{P_{ap}} \alpha_{abs}$

Diffuse Light Simulation Procedure

Each model was simulated for its diffuse light performance using the following procedure:

1. Input the desired number of rays to be simulated
2. Assign the “Lower Angle” of the source’s “Aim Sphere” to be 90 degrees
3. Assign the orientation angles of the source to be in the negative y-direction
4. Run simulation

- Absorptance of the absorber: $\eta = \frac{P_{abs}}{P_{ap}} \alpha_{abs}$

Off-axis Simulation Procedure

Each model was simulated for its off-axis performance using the following procedure:

- $$\eta = \frac{P_{abs}}{P_{ap}} \alpha_{abs}$$

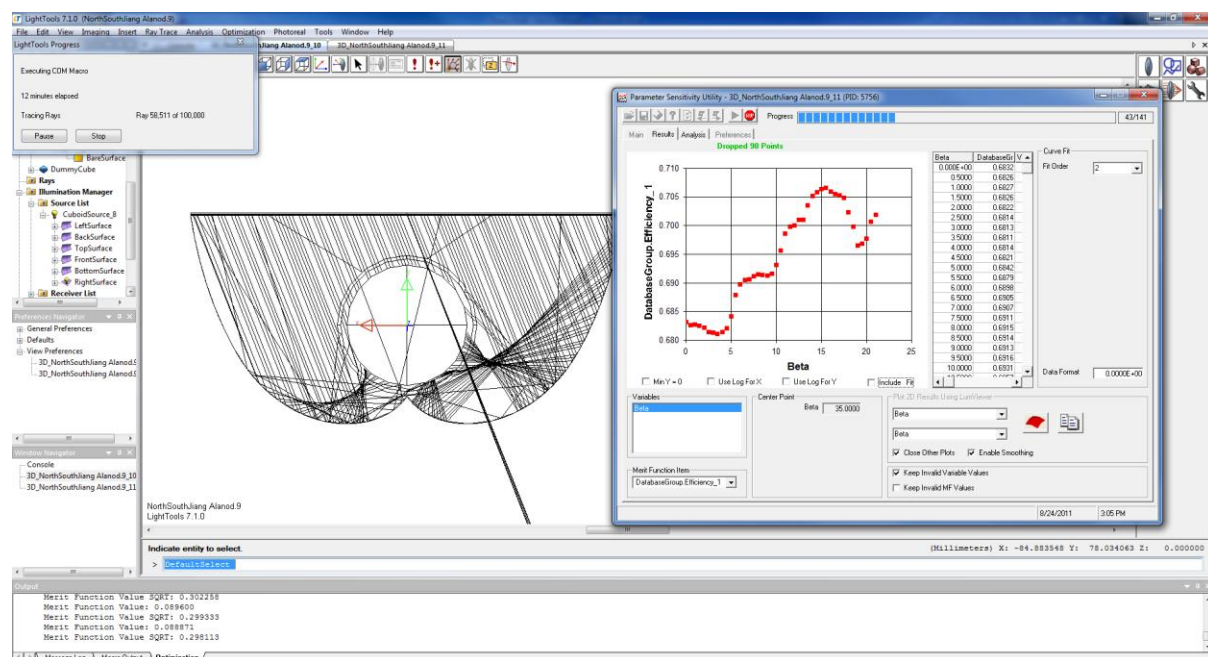


Figure 40. Off-axis simulation in LightTools

Optical Values

Table 7. Optical values used in models

		NS AL	NS RT	NS P	EW AL	EW RT	EW P
Reflector	Hemispherical reflectance	91.9%	94.0%	100%	91.9%	94.0%	100%
	%Specular	92.0%	95.0%	100%	92.0%	95.0%	100%
Glass	Transmittance, τ_g	91.7%	91.7%	100%	91.7%	91.7%	100%
	Reflectance, ρ_g	8.0%	8.0%	0%	8.0%	8.0%	0%
Absorber	Absorptance, α_A	90.2%	90.2%	100%	90.2%	90.2%	100%

3.1.2. Results and Discussion

Each scenario was modeled to understand its on-axis optical efficiency, diffuse optical efficiency, total optical efficiency, acceptance angle, and the average number of reflections. Both the East-West and North-South concentrators were modeled using three different scenarios: Alanod, Reflectech, and Perfect. Examples of ray traces can be seen in (Figures 41 and 43).

North-South Collector

Table 8. North-South Optical Efficiency Summary

Scenario	On Axis Efficiency $\eta(\theta = 0^\circ, \alpha = 0.247^\circ)$	Diffuse Efficiency $\eta(\theta = 0^\circ, \alpha = 90^\circ)$	Total Efficiency η_o	Acceptance Angle θ_{max}
NS AL	68.20%	64.57%	69.01%	59.88°
NS RT	70.80%	66.38%	71.54%	59.88°
NS P	88.58%	78.11%	88.75%	59.85°

As can be seen in Table 8, the on-axis optical efficiencies for the North-South Alanod (NS AL), Reflectech (NS RT), and Perfect (NS P) scenarios were 68.2%, 70.8%, and 88.6%; respectively. The North-South results show that a Reflectech reflector should have a 3.8% improvement over Alanod in on-axis optical efficiency. Also, the North-South results from the Perfect scenario show a loss of 11.4% due to geometric, gap, and refractive losses.

Using the diffuse efficiency results, the known concentration, and assuming a percentage of the light coming from a diffuse source; the total optical efficiency of each scenario using the following equation [23]:

$$\eta_o = \frac{\%Direct \cdot \eta(0, 0.247) + \%Diffuse \cdot \eta(0, 90)}{\%Direct + \frac{\%Diffuse}{C}}, \quad (3.1)$$

where $\%Direct = 85\%$, $\%Diffuse = 15\%$, and $C = 1.15$. As can be seen in Table 8, the total efficiencies were modeled to be 69.0%, 71.5%, and 88.8% for the Alanod, Reflectech, and Perfect scenarios respectively⁵. The Reflectech version shows an improvement of 3.6% over the Alanod version of the collector in terms of total efficiency.

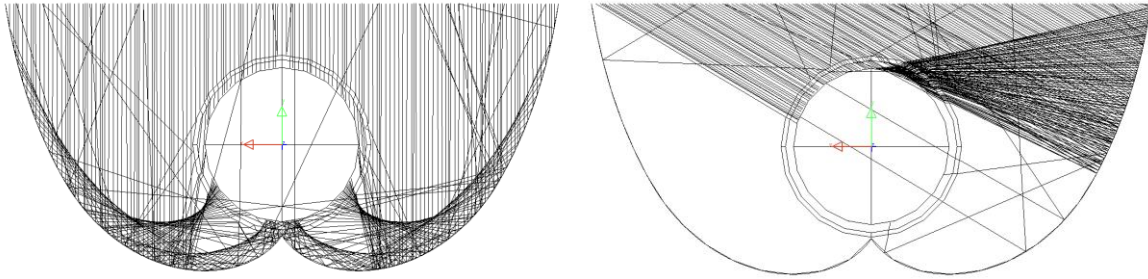


Figure 41. Ray-tracing for North-South Reflectech collectors

The off-axis performance was modeled for each of the North-South scenarios resulting in virtually the same acceptance angle as expected: 59.9° compared to the designed acceptance angle of 60° . As can be seen in the incidence angle modifier chart for the NS collectors in Figure 42, each of the models showed an improvement of up to 10% as the angle approaches the acceptance angle.

The increase in the relative efficiency in the off-axis performance can be attributed the reduction of the average number of reflections. The chart shows that the “imperfect” models fair better relative off-axis performance than the Perfect collector. It can be inferred that fact that Alanod and Reflectech models include diffuse reflection that diffuse

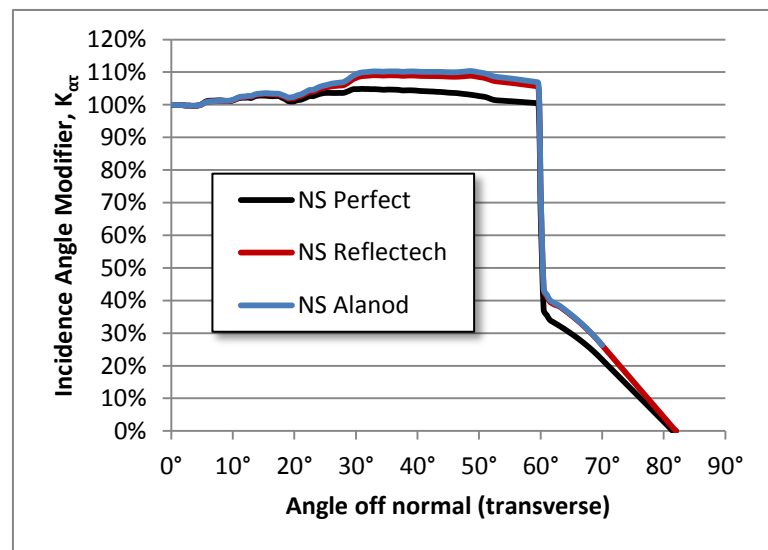


Figure 42. North-South Modeled IAM Chart

reflection actually contributes to

the off-axis performance. A “tail” can be seen in the data from 60° to around 82° which is due to the fact that the concentrator was truncated.

⁵ As can be seen in the results, the “total optical efficiency” can result in a higher value than on-axis or diffuse efficiency independently; this is due to the fact that the $1/C$ assumption is only an approximation of how well the collector can concentrate diffuse light.

East-West Collector

Table 9. East-West Optical Efficiency Summary

Scenario	On Axis Efficiency	Diffuse Efficiency	Total Efficiency	Acceptance Angle
EW AL	64.69%	39.77%	65.31%	33.85°
EW RT	68.11%	41.08%	68.63%	33.85°
EW P	85.23%	49.25%	85.54%	33.80°

As can be seen in Table 9, the on-axis optical efficiencies for the East-West Alanod (EW AL), Reflectech (EW RT), and Perfect (EW P) scenarios were 64.7%, 68.1%, and 85.2%; respectively. The East-West results show that a Reflectech reflector should have a 5.3% improvement over Alanod in on-axis optical efficiency. Also, the East-West results from the Perfect scenario show a loss of 11.4% due to geometric, gap, and refractive losses.

Using the diffuse efficiency results, the known concentration, and assuming a percentage of the light coming from a diffuse source; the total optical efficiency of each scenario using the following equation:

$$\eta_0 = \frac{\%Direct \cdot \eta(0, 0.247) + \%Diffuse \cdot \eta(0, 90)}{\%Direct + \frac{\%Diffuse}{C}}, \quad (3.2)$$

where $\%Direct = 85\%$, $\%Diffuse = 15\%$, and $C = 1.8$. As can be seen in Table 9, the total efficiencies were modeled to be 65.3%, 68.6%, and 85.5% for the Alanod, Reflectech, and Perfect scenarios respectively. The Reflectech version shows an improvement of 5.0% over the Alanod version of the collector in terms of total efficiency.

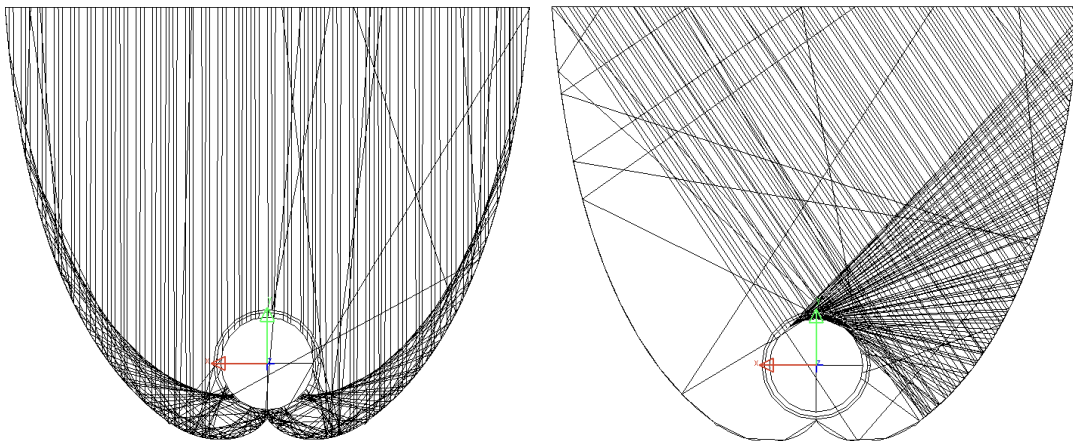


Figure 43. Ray-tracing for East-West Alanod collectors

The off-axis performance was modeled for each of the North-South scenarios resulting in virtually the same acceptance angle as expected: roughly 33.9° compared to the designed acceptance angle of 34° . As can be seen in the incidence angle modifier chart for the EW collectors in Figure 44, each of the models showed an improvement of up to 11% as the angle approaches the acceptance angle. The increase in the relative efficiency in the off-axis performance can be attributed the reduction of the average number of reflections. The chart shows that the “imperfect” models fair better relative off-axis performance than the Perfect collector. It can be inferred that fact that Alanod and Reflectech models include diffuse reflection that diffuse reflection actually contributes to the off-axis performance. A “tail” can be seen in the data from 34° to around 43° which is due to the fact that the concentrator was truncated.

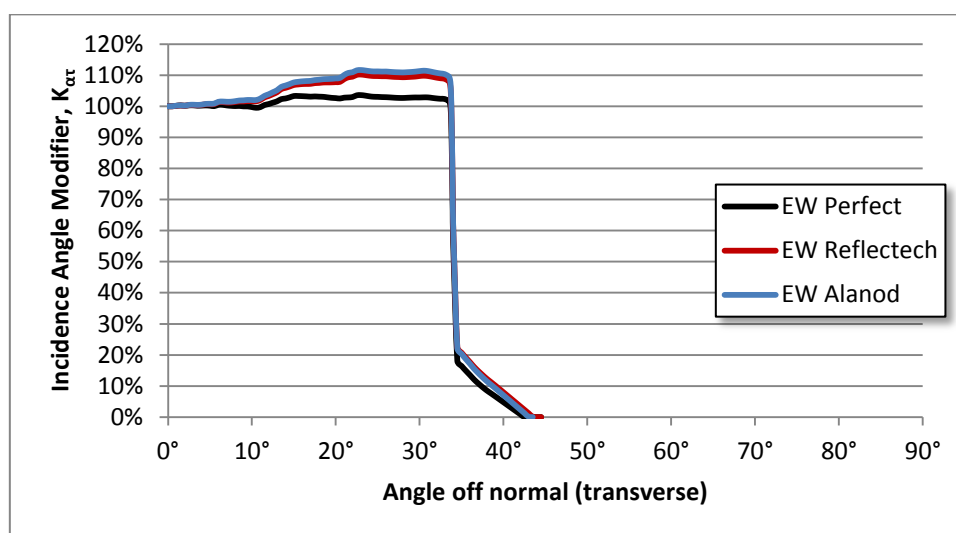


Figure 44. East-West Modeled IAM Charts

3.2. Thermal Models

Thermal analyses of XCPC designs were previously carried out by Alfonso Tovar, Randy Gee, and others in Tovar’s master’s thesis and in the California Energy Commission project.

This thesis intends to highlight the results of the previous thermal models and use the results as a basis to understand and compare the experimental results. Some modifications to the models were made to update the models to reflect the most current information available.

Unless stated otherwise, the following assumptions were made in the thermal models:

- Steady state conditions
- Fully developed conditions throughout

- The flux incident on the absorber is considered constant over all temperatures
- The flux incident on the absorber is considered to be uniform
- The flux incident on the absorber comes from separate optical models
- Heat gained by the glass from direct sunlight is considered constant
- Working fluids are incompressible
- Heat loss from conduction to environment is considered negligible
- Heat loss from manifold is not considered
- Heat loss from the ends of the tube is neglected
- Resistance from welds and imperfect connections between pipe and absorber are not considered
- Convective heat loss coefficient from glass to environment is considered constant
- Potential and kinetic energy changes are neglected
- Fouling factors are neglected

3.2.1. Bulk Model Setup

The thermal model can be broken into separate control volumes to understand the heat transfer relationships between different components inside of the tube through an energy balance.

Glass

Applying an energy balance on a control volume about the glass [5]:

$$q''_{in} + q''_{rad} - [q''_{conv} + q''_{rad,sky}] = 0, \quad (3.3)$$

where:

$$q''_{in} = \alpha_g G_c, \quad (3.4)$$

$$q''_{rad} = h_{rad} \sigma (T_A^4 - T_g^4), \quad (3.5)$$

$$q''_{conv} = h(T_g - T_\infty), \quad (3.6)$$

$$q''_{rad,sky} = \epsilon_g \sigma (T_g^4 - T_{sky}^4), \quad (3.7)$$

$$h_{rad} = \frac{1}{\frac{1}{\epsilon_A} + \frac{1 - \epsilon_g}{\epsilon_g} \frac{D_{Ae}}{D_{gi}}}, \quad (3.8)$$

$$T_{sky} = 0.0552 T_\infty^{1.5}, \quad (3.9)$$

G_c = flux incident on glass.

Substituting definitions [5]:

$$\alpha_g G_c + h_{rad} \sigma (T_A^4 - T_g^4) - h(T_g - T_\infty) - \epsilon_g \sigma (T_g^4 - T_{sky}^4) = 0, \quad (3.10)$$

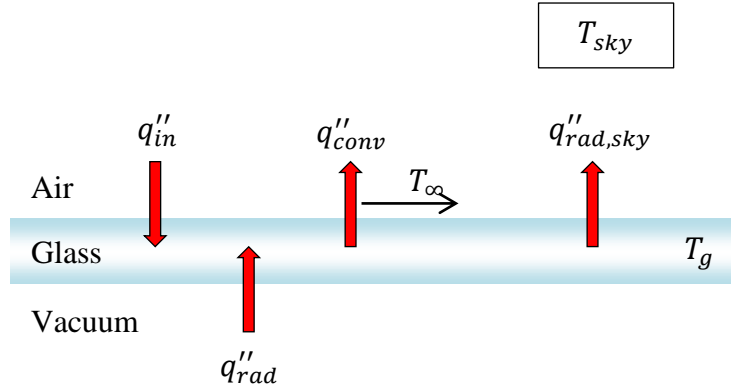


Figure 45. Heat balance at glass

Absorber

Applying an energy balance on a control volume about the absorber [5]:

$$q''_{abs} - q''_{rad} - q''_{cond} = 0, \quad (3.11)$$

where:

$$q''_{abs} = \eta_0 G, \quad (3.12)$$

$$q''_{rad} = h_{rad} \sigma (T_A^4 - T_g^4), \quad (3.13)$$

$$h_{rad} = \frac{1}{\frac{1}{\epsilon_A} + \frac{1 - \epsilon_g}{\epsilon_g} \frac{D_{Ae}}{D_{gi}}}. \quad (3.14)$$

After substitution:

$$\eta_0 G - \frac{1}{\frac{1}{\epsilon_A} + \frac{1 - \epsilon_g}{\epsilon_g} \frac{D_{Ae}}{D_{gi}}} \sigma (T_A^4 - T_g^4) - q''_{cond} = 0, \quad (3.15)$$

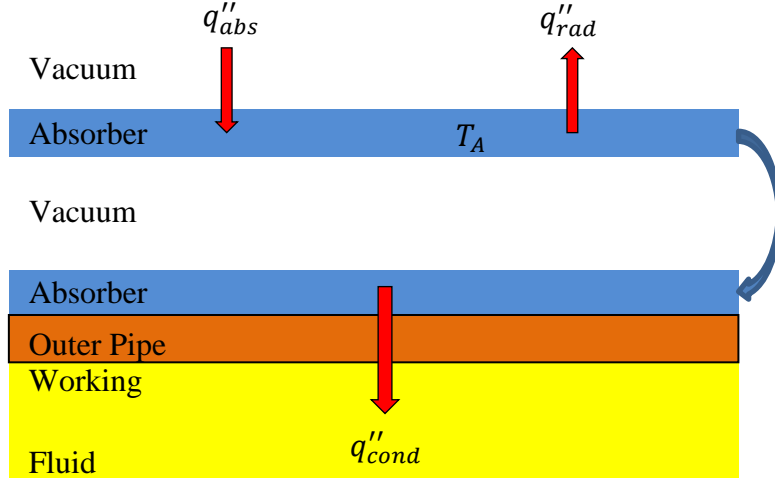


Figure 46. Heat balance at the absorber

Heat Transfer from Absorber to Fluid (q''_{cond}):

The total resistance between the exterior of the absorber to the fluid can be defined by [5]:

$$R = \frac{\ln D_{oe}/D_o}{2\pi Lk} + \frac{1}{\pi D_o L h_f}, \quad (3.16)$$

Therefore:

$$q_{cond} = \frac{\Delta T}{R} = \frac{T_b - T_{out}}{R}, \quad (3.17)$$

$$T_b = T_A - L \frac{q''_{cond}}{2\kappa A_t} \left(\frac{\pi D_A}{2} \right)^2, \quad (3.18)$$

Heat Gained by Fluid:

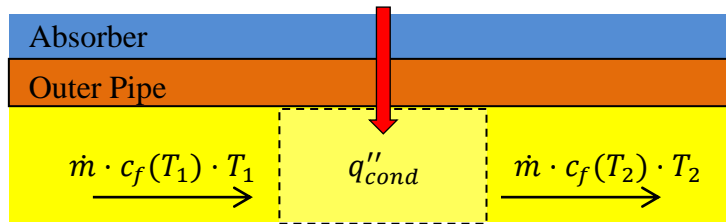


Figure 47. Heat gained by fluid

Through conservation of energy, the heat gained by the fluid can be defined as:

$$\Delta T = \frac{q_{cond}}{\dot{m} C_p}, \quad (3.19)$$

where:

$$\Delta T = T_{out} - T_{in}, \quad (3.20)$$

Summary of Coupled Equations [5]

$$A_g \alpha_g G_c + A_A h_{rad} \sigma (T_A^4 - T_g^4) - A_g h (T_g - T_\infty) - A_g \epsilon_g \sigma (T_g^4 - T_{sky}^4) = 0, \quad (3.21)$$

$$A_A \eta_0 G - A_A \frac{1}{\frac{1}{\epsilon_A} + \frac{1 - \epsilon_g}{\epsilon_g} \frac{D_{Ae}}{D_{gi}}} \sigma (T_A^4 - T_g^4) - q_{cond} = 0, \quad (3.22)$$

$$q_{cond} = \frac{T_b - T_{out}}{\frac{\ln(D_{oe}/D_o)}{2\pi L \kappa} + \frac{1}{\pi D_o L h_f}}, \quad (3.23)$$

$$T_b = T_A - L \frac{q_{cond}''}{2\kappa A_t} \left(\frac{\pi D_A}{2} \right)^2, \quad (3.24)$$

$$\Delta T = \frac{q_{cond}}{\dot{m} C_p}, \quad (3.25)$$

$$T_{out} = \Delta T + T_{in}. \quad (3.26)$$

Equations (3.21) through (3.26) were solved numerically using the software EES (Engineering Equation Solver) [5].

3.2.2. Finite Difference Model Setup (Counter-flow Tube)

To understand the temperature of the tube as a function of length and to further understand the contributing factors to the collectors' efficiency, a finite difference thermal model was developed.

The origin of the model's coordinate system was placed at the center of the inner pipe at the front end of the tube where x goes from 0 to L along the length of the tube. The tube was divided into n sections along the x axis, each representing a length of Δx . Each section carries nodes for the temperature of all of the relevant surfaces and volumes within the tube: fluid in inner pipe $T_{di}(x)$, inner surface of inner pipe $T_{ii}(x)$, outer surface of inner pipe $T_{io}(x)$, fluid in annulus $T_{do}(x)$, inner surface of outer pipe $T_{oi}(x)$, outer surface of outer pipe $T_{oo}(x)$, and the outer surface of the absorber $T_a(x)$. The inner and outer surfaces of the glass (T_{gi} and T_{go}) were assumed to be constant along the length of the tube to simplify the radiative exchange between the absorber and the glass. This leads to $7n + 2$ unknown temperatures in the modeled system.

Energy balances and other relations were found at each node leading to $7n + 2$ equations capable of solving all of the unknown temperatures. These equations were put into matrix

form and solved simultaneously using a MatLab code. Since many of the properties are temperature dependent, temperatures are assumed before initial solution and then the process is iterated.

Equation Set 1:

Set input temperature into tube

$$T_{di}(0) = T_{initial}$$

Heat balance of inner oil at x:

[Heat gained by fluid by convection]

+ [Heat moved by fluid]=0

$$h_{ii}A_{ii}[T_{ii}(x) - T_{di}(x)] \\ + \dot{m}c_p[T_{di}(x - \Delta x) - T_{di}(x)] = 0$$

Equation Set 2:

Heat balance at inner side of inner pipe:

[Heat transferred to inner fluid] + [Heat conducted from inner to outer side of inner pipe] = 0

$$h_{ii}A_{ii}[T_{ii}(x) - T_{di}(x)] + \frac{2\pi\kappa_{cu}\Delta x}{\ln\left(\frac{D_{ie}}{D_i}\right)}[T_{ii}(x) - T_{io}(x)] = 0$$

Equation Set 3:

Heat balance at outer oil:

[Heat convected to oil by inner pipe] + [Heat moved to next node in oil] + [Heat convected to oil by outer pipe] = 0

$$h_{io}A_{io}[T_{io}(x) - T_{do}(x)] + \dot{m}c_p[T_{do}(x) - T_{do}(x - \Delta x)] + h_{oi}A_{oi}[T_{oi}(x) - T_{do}(x)] = 0$$

Equation Set 4:

Heat balance at inner side of outer pipe:

[Heat convected to oil by outer pipe] + [Heat conducted through outer pipe radially] = 0

$$h_{oi}A_{oi}[T_{oi}(x) - T_{do}(x)] + \frac{2\pi\kappa_{cu}\Delta x}{\ln\left(\frac{D_{oe}}{D_o}\right)}[T_{oi}(x) - T_{oo}(x)] = 0$$

Constrain the outer oil value at the end of the tube to equal the temperature of the inner oil:

$$T_{do}(L) = T_{di}(L)$$

Equation Set 5:

Heat balance at outer side of outer pipe:

[Heat conducted through outer pipe] + [Heat conducted to absorber] = 0

$$\frac{2\pi\kappa_{cu}\Delta x}{\ln\left(\frac{D_o}{D_{oe}}\right)}[T_{oo}(x) - T_{oi}(x)] + \frac{\pi D_{oe}h_{cont}\Delta x}{2}[T_{oo}(x) - T_a(x)] = 0$$

Equation Set 6:

Heat balance at absorber surface:

[Heat transferred from outer pipe] + [Heat lost from radiation to glass] = [Heat gained from incoming flux]

$$\frac{\pi D_{oe}h_{cont}\Delta x}{2}[T_{oo}(x) - T_a(x)] + \epsilon_a\sigma[T_a(x)^4 - T_{gi}(x)^4] = \alpha_a H_{oa}$$

Linearize radiation using guesses and rearrange:

$$\frac{\pi D_{oe}h_{cont}\Delta x}{2}T_{oo}(x) + \left[\epsilon_a\sigma T_{a,guess}^3 - \frac{\pi D_{oe}h_{cont}\Delta x}{2}\right]T_a(x) - \epsilon_a\sigma T_{gi,guess}^3 T_{gi}(x) = \alpha_a H_{oa}$$

Assumptions used to create the model include: steady state conditions, none of the solids store energy, constant glass temperature along its length, glass is black in the infrared range, conduction only occurs radially, contact resistance between absorber and outer pipe is assumed, heat transfer coefficients from the pipes to the fluid are assumed constant, no heat is radiated at the ends of the absorber, radiative exchange between absorber and glass occurs diffusely.

3.3. Combined Model Results

3.3.1. On-Axis Efficiency

Using the optical efficiency model results in Section 4.1 as inputs into the thermal models described in Section 4.2, the efficiency of each collector can be assessed as a function of temperature as can be seen in Figure 48 below.

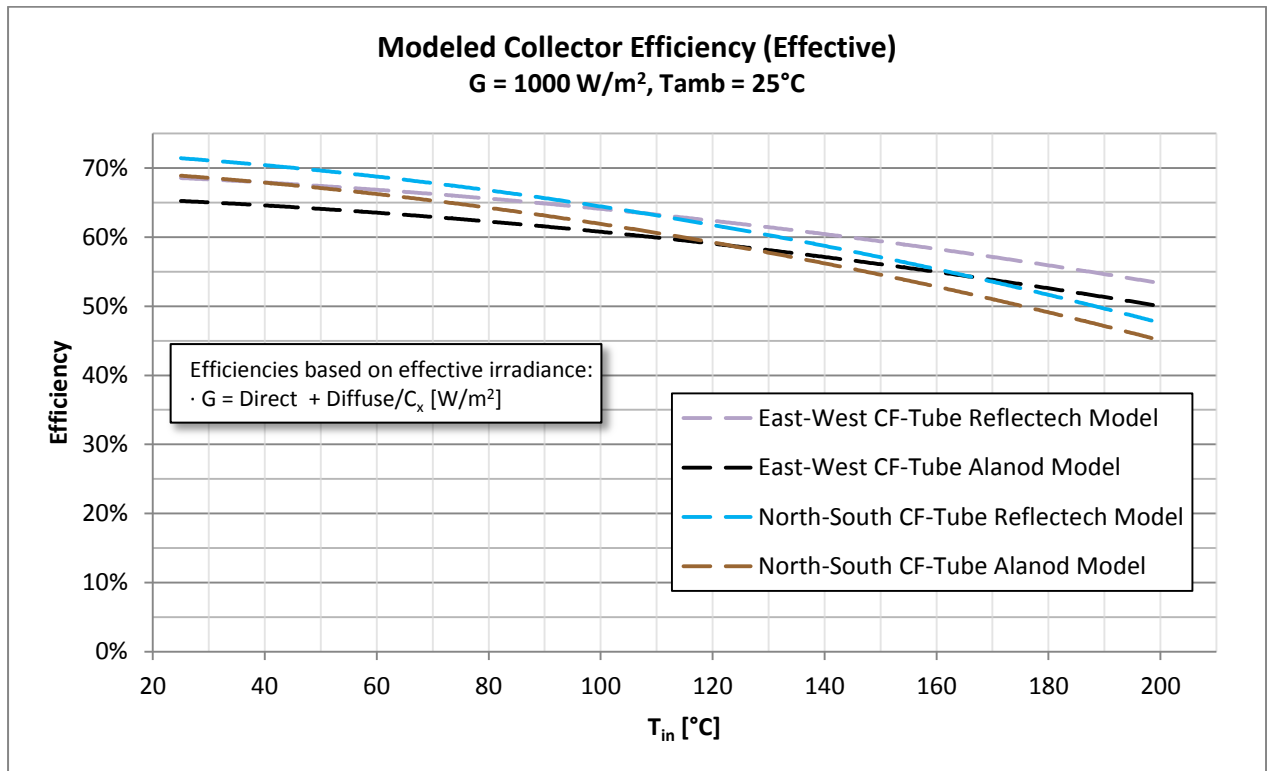


Figure 48. Modeled on-axis efficiencies of Counter-flow tube collectors

3.3.2. Temperature Profile of Tube

The temperature profile of the tube was modeled using the finite difference model. The results for the North-South and East-West models with Alanod reflectors can be found in Figure 49 and Figure 50 assuming an input temperature of 200°C .

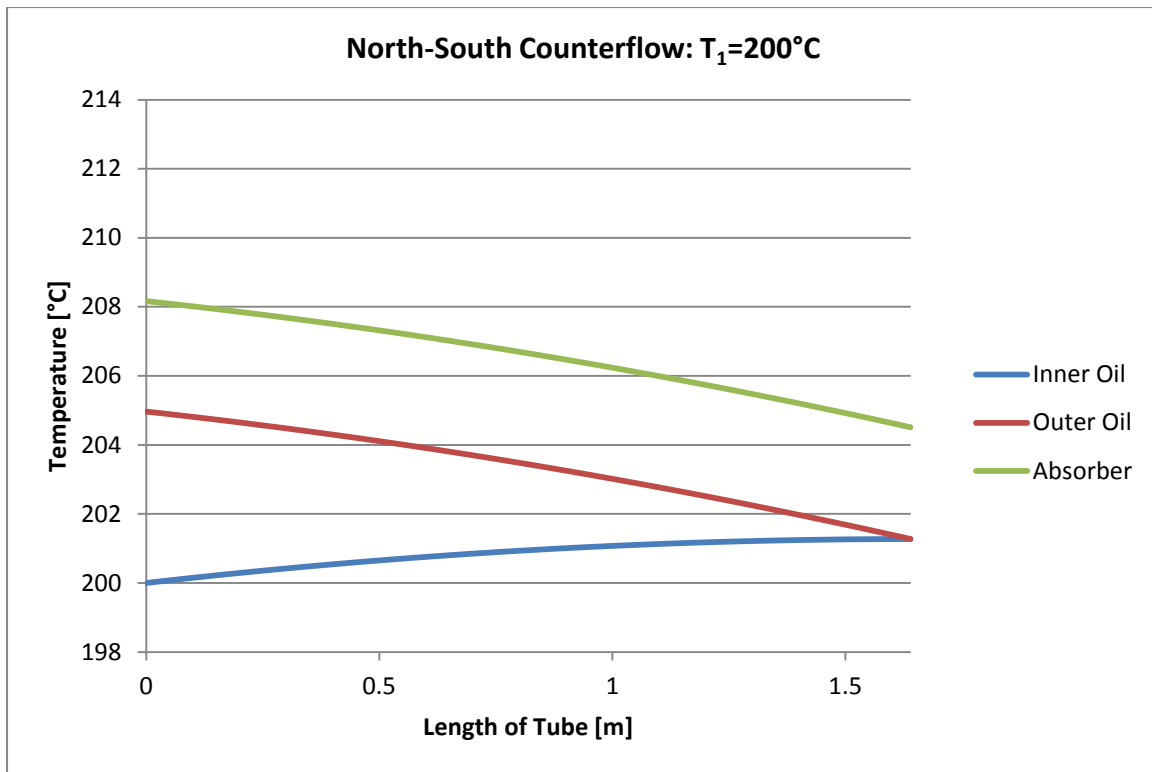


Figure 49. Modeled temperature profile for North-South counter-flow

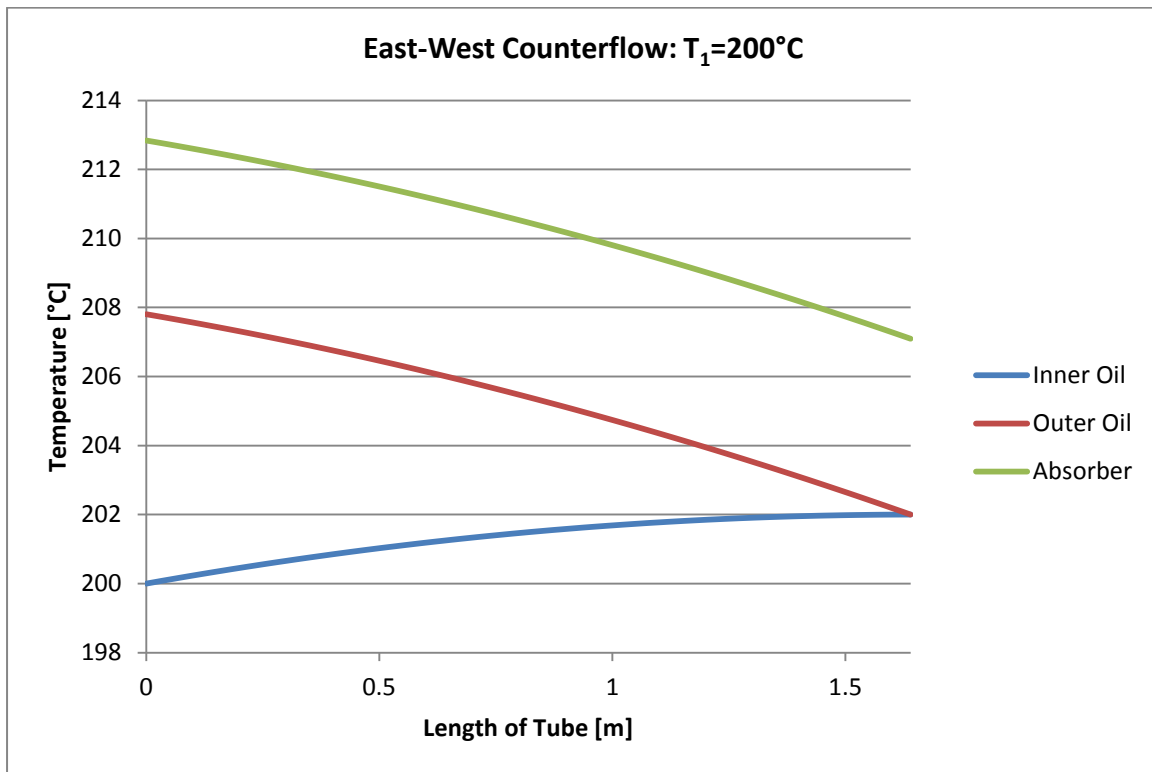


Figure 50. Modeled temperature profile for East-West counter-flow

4. Experiment

The seven collectors listed section 2.3 were tested for their performance. The objectives of these experiments were to validate the optical and thermal models, characterize the collectors, and to determine their feasibility in real-world applications. Experiments were carried out to understand the collectors' optical efficiency, thermal efficiency, angular response, and time response.

4.1. Methodology

4.1.1. Description of Facilities

The test facility uses is a closed loop system that includes a circulating oil temperature controller with integrated pump and expansion tank (see Figure 51). The circulating oil temperature controller provides a selectable constant temperature (up to 500°F) to the heat transfer fluid that is circulated through the collector. The loop further includes a flow meter, temperature sensors before and after the collector, and a calorimeter. The calorimeter is described in detail below. The solar collector is mounted on a dual axis tracker to allow the measurement of collector performance under controlled incidence angles.

The test facility further includes a meteorological station with a Precision Spectral Pyranometer (PSP) that is mounted on the same tracker as the solar collector, a Normal Incidence Pyrheliometer (NIP) mounted on a separate dual-axis tracker, a thermometer to measure the ambient temperature, and an anemometer.

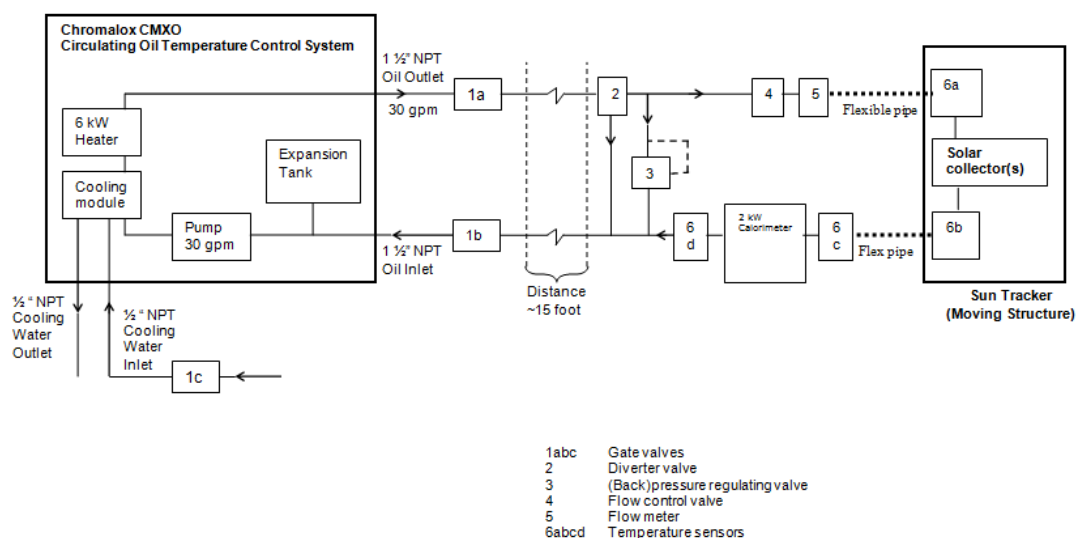


Figure 51. Schematic of test site [4]

Instrumentation and Materials

1. Circulating oil temperature controller: Chromalox CMXO 6kW
2. Pump: 3hp centrifugal pump integrated with Chromalox CMXO heater system
3. Expansion tank: 15 gallon expansion tank packaged with Chromalox CMXO placed roughly 10 feet above pump
4. Flow meter: Micro Motion Coriolis F-Series sensor
 - a. Mass flow accuracy: +/- 0.10% to 0.20%
5. Flow control valve: Valtek ½" Flow Top Control Valve
6. Back pressure regulating valve: Jordan: 1" 50-100-S6-I5-S6-Y-8-21-S6-MD Pressure Control Valve
7. Temperature sensors:
 - a. Type K Probe Thermocouple from Omega: 1/8" diameter, 12" length
 - b. 100 ohm 4-wire RTD from Omega: 1/8" diameter, 9" length
8. Sun tracker: Wattsun AZ-125 dual axis tracker
9. Pyranometer: Eppley Precision Spectral Pyranometer
10. Pyrhelimeter: Eppley Normal Incidence Pyrhelimeter
11. Calorimeter: custom made by Valin, Inc.
 - a. Core heater: Tubular Heater Round Cross-Section, 30 watts/square inch, 2,000 Watts
 - b. Jacket heater
 - c. Controller
 - d. Jacket temperature sensor (controller): 100 ohm 3-wire RTD from Omega
 - e. Jacket temperature sensor (data): Type K Surface Thermocouple from Omega
 - f. DC Power Supply
 - g. Power meter: custom made
12. Data logger:
 - a. Agilent 34970A Data Acquisition/Switch Unit
 - b. Obvius Acquisuite A8811 and A8923
13. Working fluid: Duratherm 600

4.1.2. Test Protocols

Collector Dimensions

The collector's area is commonly measured for its gross collector, effective aperture, and absorber area. The gross collector area, A_G , is defined as the product of the entire length and width of the collector including portions that do not contribute to the collection of sunlight. The effective aperture area, A_A , is defined as the product of the length and width of the collector less the portions of the collector that do not contribute to the collection of sunlight. The absorber area, A_{abs} , is the total surface area of all of the absorbers in the collector.

The concentration ratio, C , is defined as the ratio between the effective aperture area and the surface area of absorber area [24]:

$$C = \frac{A_A}{A_{abs}}. \quad (4.1)$$

Solar Irradiance

Two major components of the solar irradiance are measured throughout all testing: direct normal irradiance (DNI) and normal hemispherical irradiance. The DNI component of the irradiance, G_{DNI} , is measured using an Eppley Normal Incidence Pyrheliometer (NIP) placed in-plane with the tracking collector⁶. The normal hemispherical irradiance, G_{NHI} , is measured using an Eppley Precision Spectral Pyranometer (PSP) mounted in-plane with the tracking collector. Additionally, the normal diffuse irradiance, $G_{diffuse}$, is defined as the difference between the normal hemispherical and the direct normal irradiance

$$G_{diffuse} = G_{NHI} - G_{DNI}. \quad (4.2)$$

For high concentration systems ($C > 2$), the available irradiance to the collector is defined to only include the direct component of the irradiance: $G = G_{DNI}$. For flat plate collectors ($C = 1$), the normal hemispherical irradiance is often used as the available solar flux: $G = G_{NHI}$. For low concentration systems ($1 < C \leq 2$), it is often appropriate to define the available irradiance to include the diffuse component modified by the collector's concentration ratio [23, 25, 25]:

$$G = G_{eff} = G_{DNI} + \frac{G_{diffuse}}{C}. \quad (4.3)$$

⁶ For some testing procedures, an additional NIP was placed on a separate tracker nearby to measure the DNI.

The majority of the data presented in this report uses the effective irradiance, G_{eff} , to determine efficiencies. To compare directly with other technologies the direct and hemispherical values of irradiance are sometimes used and will be indicated when this is the case.

The output of the PSP's and NIP's are measured in voltage by the Agilent data logger. Each instrument is labeled with a calibration factor which allows the researcher to convert the voltage reading into an irradiance reading in the units of watts per square meter [W/m^2] in the following manner: $G = f_{cal} \times V$.

Test Conditions

All test conditions must be met during the course of each test. Table 10 describes the test conditions repeated for all efficiency testing (unless otherwise indicated). The conditions outlined in Table 11 are for any testing that involves the calorimeter.

Table 10. Test conditions for efficiency testing

Collector inlet temperature, T_1	$\pm 1^\circ\text{C}$ of target temperature. $T_{target} - 1 \leq T_1 \leq T_{target} + 1$
Collector inlet temperature, T_1	Must not vary by more than $\pm 1^\circ\text{C}$ during the course of test
Mass flow rate, \dot{m}	$\pm 1 \text{ g/s}$ of target flow rate. $\dot{m}_{target} - 1 \leq \dot{m} \leq \dot{m}_{target} + 1$
Mass flow rate, \dot{m}	Must not vary by more than $\pm 1 \text{ g/s}$ during the course of test
DNI, G_{DNI}	$G_{DNI} \geq 800 \text{ W/m}^2$
DNI, G_{DNI}	Must not vary by more than $\pm 25 \text{ W/m}^2$ during the course of test
Diffuse Irradiance, $G_{diffuse}$	$\frac{G_{diffuse}}{G_{DNI}} \leq 20\%$

Table 11. Additional test conditions for testing with calorimeter

Calorimeter power, \dot{Q}_{cal}	Must not vary by more than 30 W
Calorimeter jacket, T_{jacket}	$\pm 5^\circ\text{C}$ of calorimeter median temperature

Collector Thermal Efficiency: Flow Rate Method

The instantaneous collector efficiency η_{coll} is defined as

$$\eta_{coll} = \frac{\dot{Q}}{A G}, \quad (4.4)$$

with

$$\dot{Q} = \dot{m} c_p \Delta T_{coll}. \quad (4.5)$$

The collector efficiency can be calculated using any of the previously defined collector areas and irradiance values. For the sake of simplicity, only the effective aperture, A_A , is used in the results. Therefore, three different definitions of collector efficiency can be defined:

$$\eta_{eff} = \frac{\dot{Q}}{A_A G_{eff}}, \quad (4.6)$$

$$\eta_{direct} = \frac{\dot{Q}}{A_A G_{DNI}}, \quad (4.7)$$

$$\eta_{hem} = \frac{\dot{Q}}{A_A G_{NHI}}, \quad (4.8)$$

as effective, direct, and hemispherical efficiency, respectively.

The determination of the instantaneous collector efficiency based on the formulas above requires the measurement of the mass flow rate of heat transfer fluid, the temperature difference between the heat transfer fluid at the collector outlet and inlet, and the solar irradiance in addition to the aperture area of collector. The specific heat capacity is found using a linear curve fit to the data provided by the fluid's manufacturer (see Appendix): $c_p = T_m 0.0032266 + 1.84$.

Collector thermal efficiencies are measured at various inlet temperatures ranging from 80 to 200 °C.

Test procedure:

- Start pump and set desired temperature
- Remove cover from collector
- Clean any necessary surfaces on collector, PSP, and NIPS
- Switch tracker to “Automatic”
 - Once tracker is in position, check indicator on NIP to ensure that the tracker is tracking accurately. Adjust tracker sensor if needed.
- Adjust flow rate to desired value
- Initiate data gathering on computer for 30-second intervals. Measurements:
 - Mass flow rate: \dot{m}
 - Inlet and outlet collector temperatures: T_1 and T_2
 - Ambient temperature: T_{amb}
 - Wind speed: v_{wind}

- NIP: G_{DNI}
- PSP: G_{NHI}
- Once test conditions are met (Table 10), log time
- Continue gathering data for 30 minutes of stable data. Log time.

Collector Thermal Efficiency: Calorimeter Method

The instantaneous collector efficiency, η_{coll} , has been defined above in equation (4.4). If one prefers not to rely on the measurement accuracy of \dot{m} and the accuracy of the tabulated values of the heat capacity c_f of the heat transfer medium, an alternative approach can be used to determine η_{coll} . This is by using a calorimeter, which is a “perfectly” insulated electric heater placed in series after the solar collector. In this case, the heat loss of the calorimeter is assumed to be zero, and the useful power extracted from the calorimeter $\dot{Q}_{calorimeter}$ is equal to the electric power consumption of the calorimeter, which can be measured very accurately.

With

$$\dot{Q}_{cal} = \dot{m}c_f\Delta T_{cal} \quad (4.9)$$

where

\dot{Q}_{cal} : useful power extracted from collector (power consumption of calorimeter);

ΔT_{cal} : temperature difference of fluid between calorimeter outlet and inlet.

Thus, the instantaneous collector efficiency becomes:

$$\eta_{coll} = \frac{1}{A_A G} \cdot \dot{Q}_{cal} \cdot \frac{\Delta T_{coll}}{\Delta T_{cal}}. \quad (4.10)$$

The determination of the instantaneous collector efficiency based on the method using a calorimeter requires the measurement of the temperature difference of the heat transfer fluid at the collector outlet and inlet, the temperature difference of the heat transfer fluid at the calorimeter outlet and inlet, the aperture area of collector, and the solar irradiance. It is not necessary to measure the mass flow rate of heat transfer fluid and to know the specific heat capacity of the heat transfer fluid.

Test Procedure:

- Start pump and set desired temperature
- Remove cover from collector
- Clean any necessary surfaces on collector, PSP, and NIPS
- Switch tracker to “Automatic”
 - Once tracker is in position, check indicator on NIP to ensure that the tracker is tracking accurately. Adjust tracker sensor if needed.
- Adjust flow rate to desired value
- Turn on DC power supply for calorimeter
- Set jacket temperature to the expected calorimeter median temperature
- Initiate data gathering on computer for 30-second intervals. Measurements:
 - Mass flow rate: \dot{m}
 - Inlet and outlet collector temperatures: T_1 and T_2
 - Ambient temperature: T_{amb}
 - Wind speed: v_{wind}
 - NIP: G_{DNI}
 - PSP: G_{NHI}
 - Calorimeter power: \dot{Q}_{cal}
 - Inlet and outlet calorimeter temperatures: $T_{cal,1}$ and $T_{cal,2}$
 - Calorimeter jacket temperature: T_{jacket}
- Once test conditions are met, log time

Continue gathering data for 30 minutes of stable data. Log time.

Temperature dependence on collector efficiency

The temperature dependence of the instantaneous efficiency η_{coll} can be represented graphically as a function of the reduced temperature T^* . The thermal performance of the collector can then be characterized by the two coefficients a_1 and a_2 , which are determined by a least square parabolic curve fit:

$$\eta_{coll} = \eta_o - a_1 T^* - a_2 G(T^*)^2, \quad (4.11)$$

with

η_o : optical efficiency

T^* : reduced temperature

$$T^* = \frac{T_{in} - T_{amb}}{G}$$

where

a_1 and a_2 : coefficients determined from least squares parabolic curve fit, and the value of G in the formula above is assumed to be 1000 W/m².

4.2. Results

4.2.1. North-South Counterflow with Alanod Collector

Collector description

Table 12. Collector description of North-South Counterflow with Alanod Collector

Orientation	North-South
Concentration C_x	1.15
Effective Collector Area A_A	2.0 m ²
Tube Type	Counterflow-Tube
Number of Tubes	6
Reflector	Alanod (90%)

Collector optical efficiency

The optical efficiency of the collector was measured with 21-23 °C water. The heat capacity of the water was assumed to be 4.18 kJ/kg-K.

The optical efficiency based on an effective irradiance, G_{eff} , was found to be 69.5%. The optical efficiency based on direct normal irradiance, G_{DNI} was found to be 87.7%.

Collector thermal efficiency

The efficiency of the XCPC was measured at the following collector inlet temperatures: 80°C, 100°C, 120°C, 140°C, 160°C, 180°C, and 200°C; and at the following flow rates: 40-45 g/s, and 80 g/s of Duratherm 600 mineral oil.

The heat capacity of the oil was measured by Rose Consulting in November 2007. A linear approximation to the measurements was used to calculate the efficiency of the collector: $c_p = 0.002261 \cdot T_m + 1.896$.

The performance characteristics are tabulated in Table 13 and the collector efficiencies are depicted in Figure 52 through Figure 56. Figure 52 displays the raw values for the

efficiencies. Figure 53 displays the efficiencies based on the effective irradiance G_E while Figure 54 displays the efficiencies based on the direct normal irradiance (DNI) G_{DNI} .

Table 13. Performance Characteristics of North-South Counterflow with Alanod Collector

	$G=G_{\text{eff}}$	$G=G_{\text{DNI}}$
Optical Efficiency η_o	69.5%	87.7%
Efficiency at 100 °C	57.2%	72.2%
Efficiency at 200 °C	36.3%	45.2%
Loss coefficient (1) a_1	1.445 W/m ² -K	1.793 W/m ² -K
Loss coefficient (2) a_2	0.00285 W/m ² -K ²	0.00363 W/m ² -K ²
Overall heat loss coefficient U	1.910 W/m ² -K	1.973 W/m ² -K

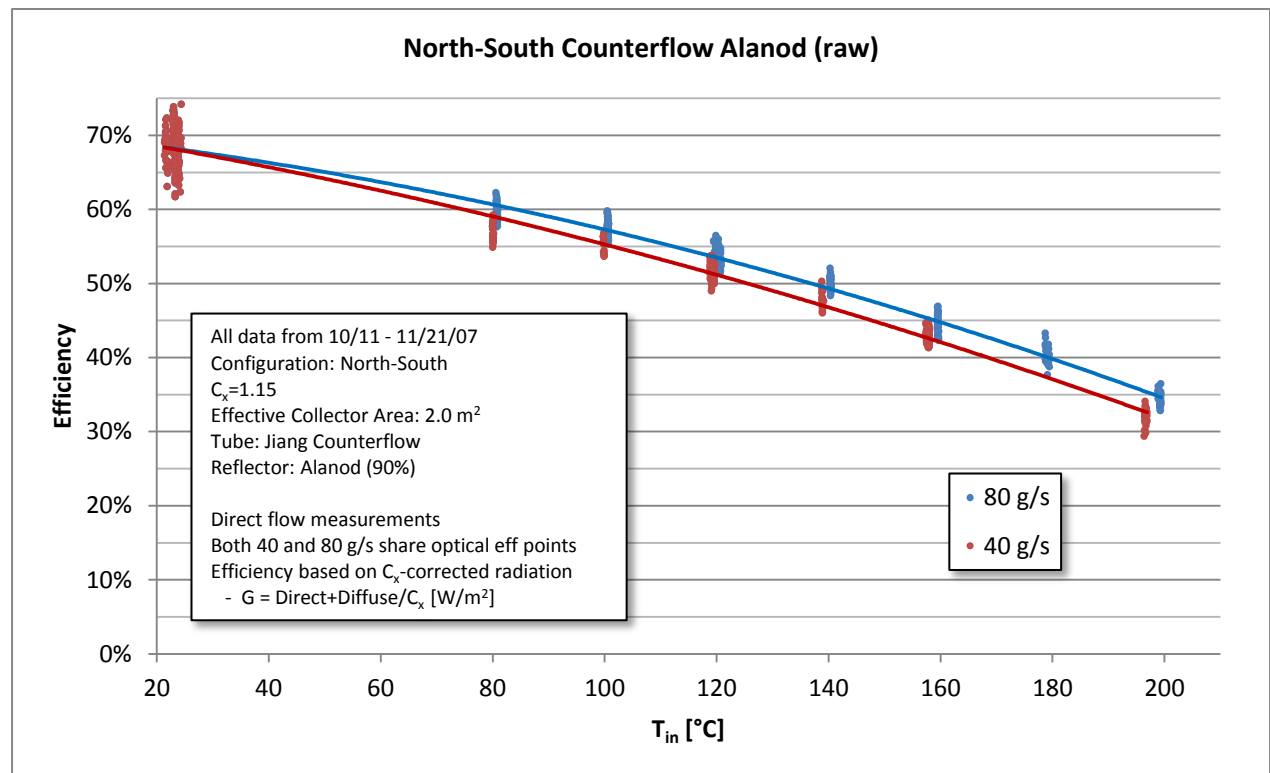


Figure 52. North-South Counterflow with Alanod Effective Raw Efficiency Curve

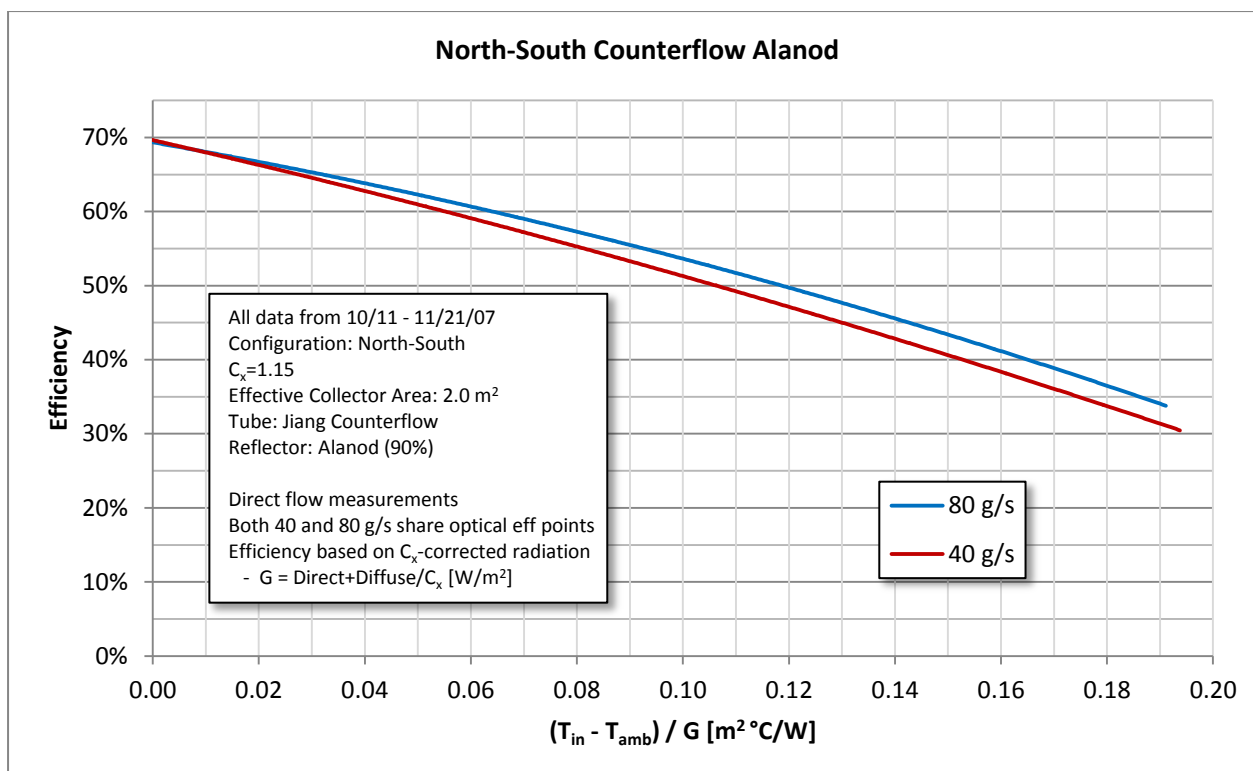


Figure 53. North-South Counterflow with Alanod Effective Reduced Efficiency Curve

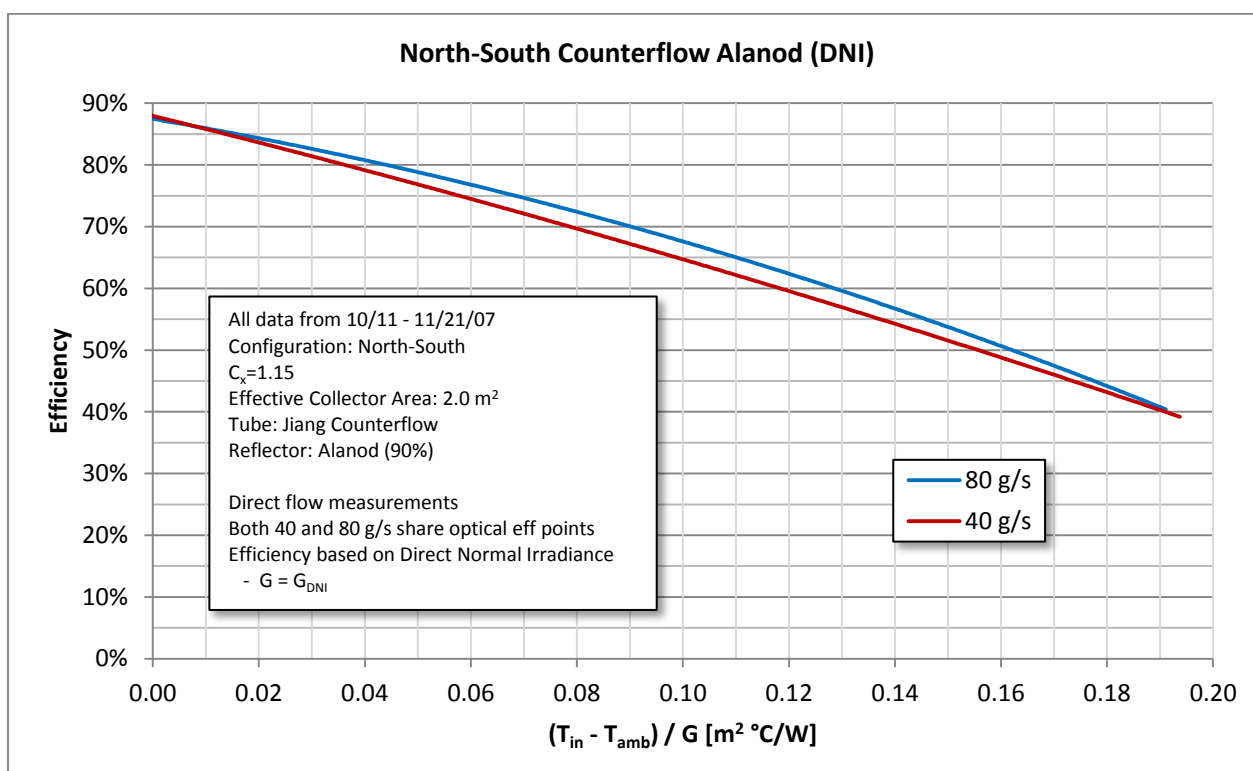


Figure 54. North-South Counterflow with Alanod Direct Reduced Efficiency Curve

Collector Incident Angle Modifier (IAM) and All-Day Performance

The IAM was measured by positioning the collector due south and tilted to be normal to the sun at solar noon (not tracking) and recording the instantaneous thermal collector efficiency at a collector inlet temperature of 140 °C over the course of the day. In this measurement the instantaneous efficiency was based on the direct normal insolation only that was measured with a Normal Incidence Pyrheliometer on a separate tracker. Figure 55 shows the relative drop in efficiency during the day as the sun angle varies between -51° and +59° at 90% relative to normal incidence. The acceptance angle was measured as +/- 55°.

The test used to determine the IAM chart and the acceptance angle can also be used to understand the collector's all-day performance. During the test, the collector performed within 90% of the nominal efficiency for roughly 7.3 hours.

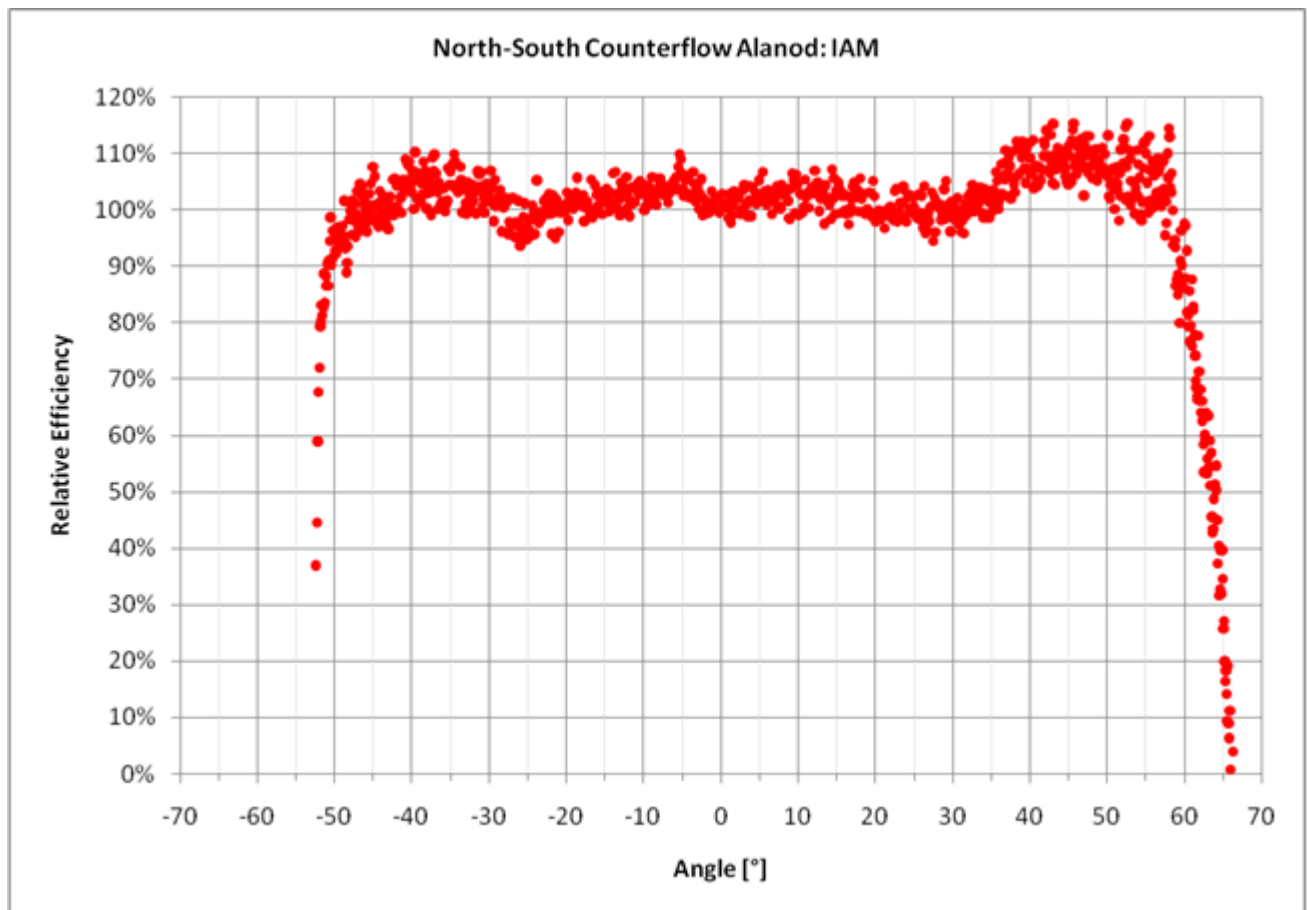


Figure 55. North-South Counterflow with Alanod: IAM Chart

Time Constant

The time constant was measured at 100°C and 35 g/s on 10/18/07. Measurements were taken for roughly twenty minutes after the collector cover was removed. Figure 56 shows the results of the test where the time constant τ_c was found to be 100 seconds.

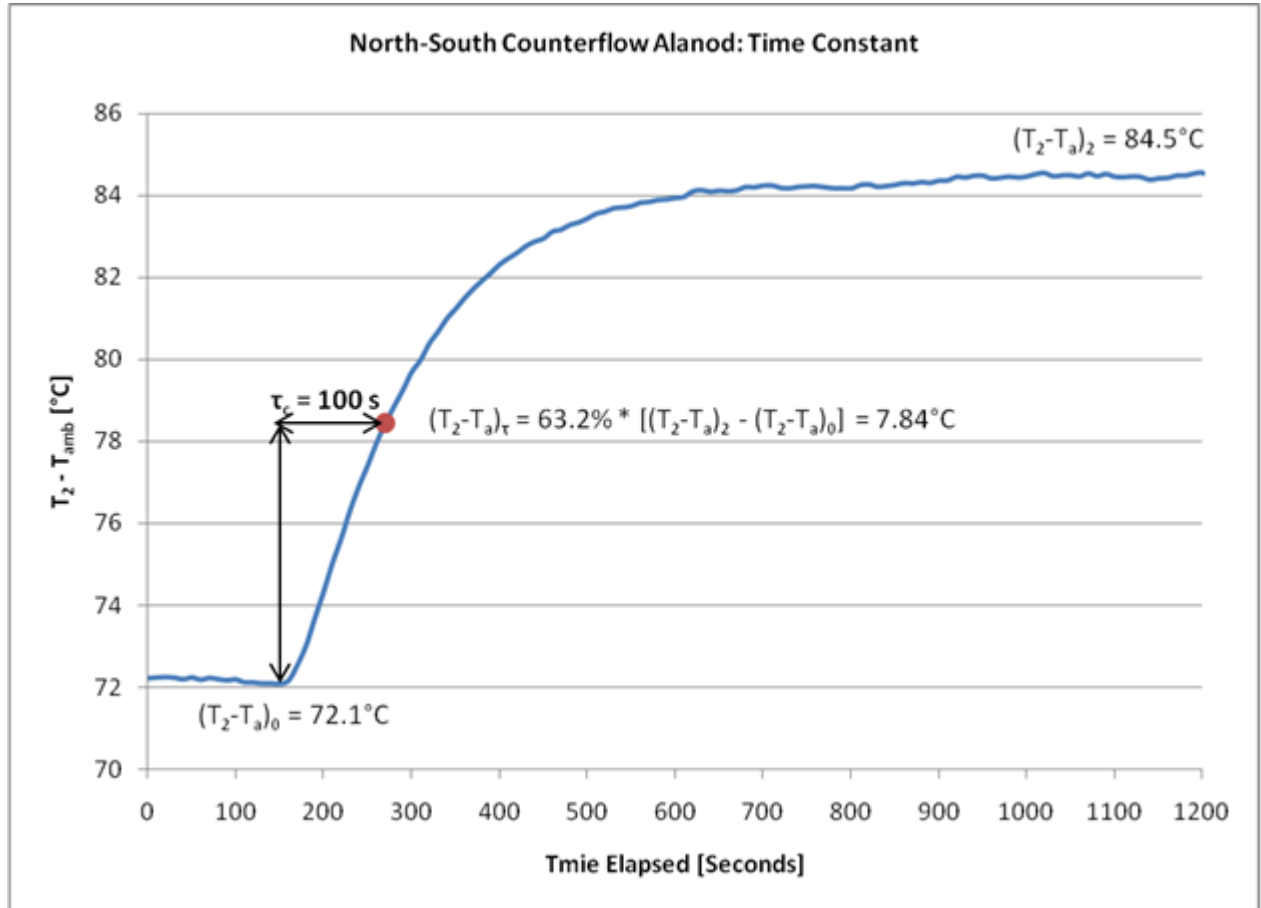


Figure 56. North-South Counterflow Time Constant Plot

Pressure drop across the collector

The pressure drop across the collector (6 absorber tubes) was measured to be between 6.9 kPa (at an oil temperature of 200°C) and 96.5 kPa (at an oil temperature of 8°C) at a flow rate of 80 g/s. The pressure drop measurements were done with the flow mixing devices inserted into the loop before the temperature sensors. It should be noted that the flow mixers increase the flow resistance.

4.2.2. East-West Counterflow with Alanod Collector

Collector Description

Table 14. Description of East-West Counterflow with Alanod Collector

Orientation	East-West
Concentration C_x	1.80
Effective Collector Area A_A	3.1 m ²
Tube Type	Counterflow-Tube
Number of Tubes	6
Reflector	Alanod (90%)

Collector optical efficiency

The optical efficiency was not measured directly for this collector. The optical efficiency used in the analysis of this collector was assumed to be the average of a linear extrapolation of the thermal efficiency and the modeled optical efficiency.

The optical efficiency based on an effective irradiance, G_{eff} , was assumed to be 64.4%. The optical efficiency based on direct normal irradiance, G_{DNI} , was assumed to be 69.3%.

Collector thermal efficiency

The efficiency of the XCPC was measured at the following collector inlet temperatures: 120°C, 140°C, 160°C, 180°C, and 200°C; and at the following flow rates: 80 g/s and 120 g/s of Duratherm 600 mineral oil [27].

The heat capacity of the oil was assumed to be consistent with the data tables provided by Duratherm. A linear approximation to the table was used to calculate the efficiency of the collector: $c_p = 0.0032266 \cdot T_m + 1.84$.

The performance characteristics are tabulated in Table 15 and the collector efficiencies are depicted in Figure 57 through Figure 59. Figure 57 displays the raw values for the efficiencies. Figure 58 displays the efficiencies based on the effective irradiance G_E while Figure 59 displays the efficiencies based on the direct normal irradiance (DNI) G_{DNI} .

Table 15. Performance Characteristics of East-West Counterflow with Alanod Collector

	$G=G_{\text{eff}}$	$G=G_{\text{DNI}}$
Optical Efficiency η_o	64.6%	69.3%
Efficiency at 100 °C	54.6%	59.9%
Efficiency at 200 °C	40.3%	44.3%
Loss coefficient (1) a_1	1.293 W/m ² -K	1.139 W/m ² -K
Loss coefficient (2) a_2	0.0007 W/m ² -K ²	0.00207 W/m ² -K ²
Overall heat loss coefficient U	1.393 W/m ² -K	1.436 W/m ² -K

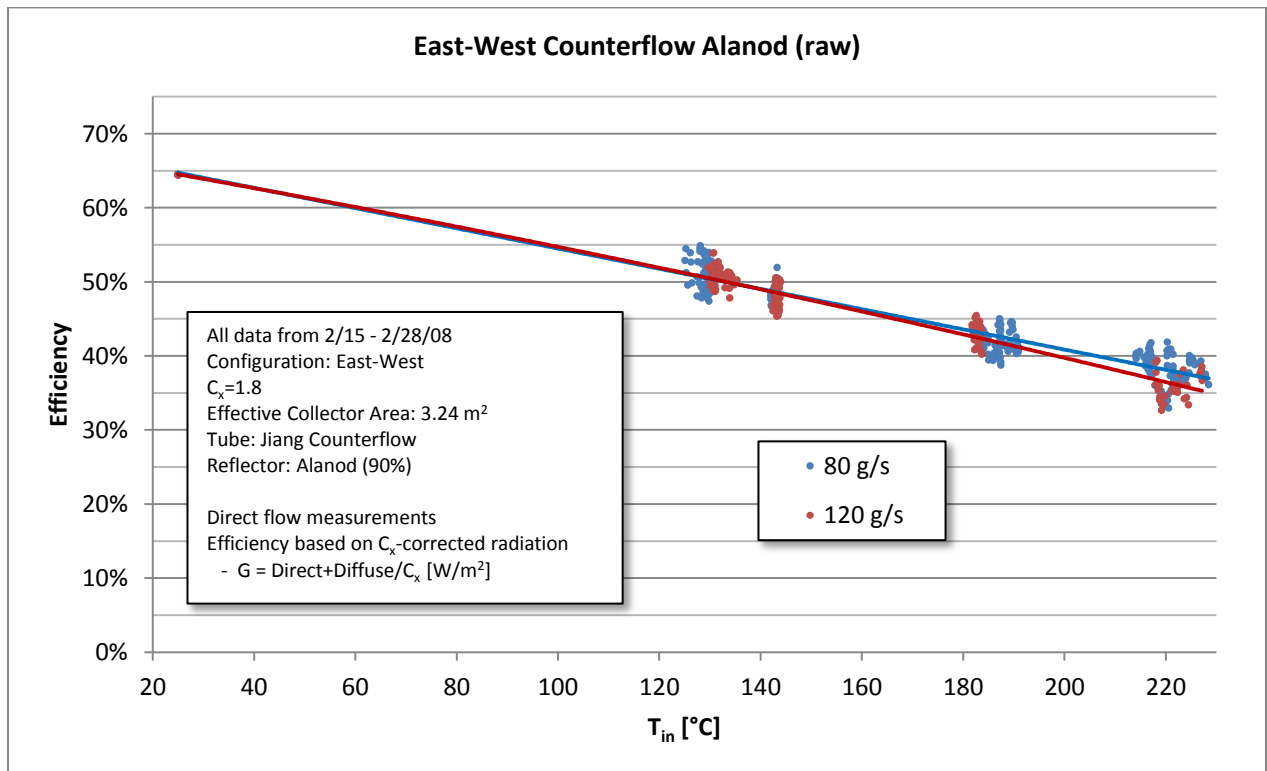


Figure 57. East-West Counterflow with Alanod Raw Efficiency Curve

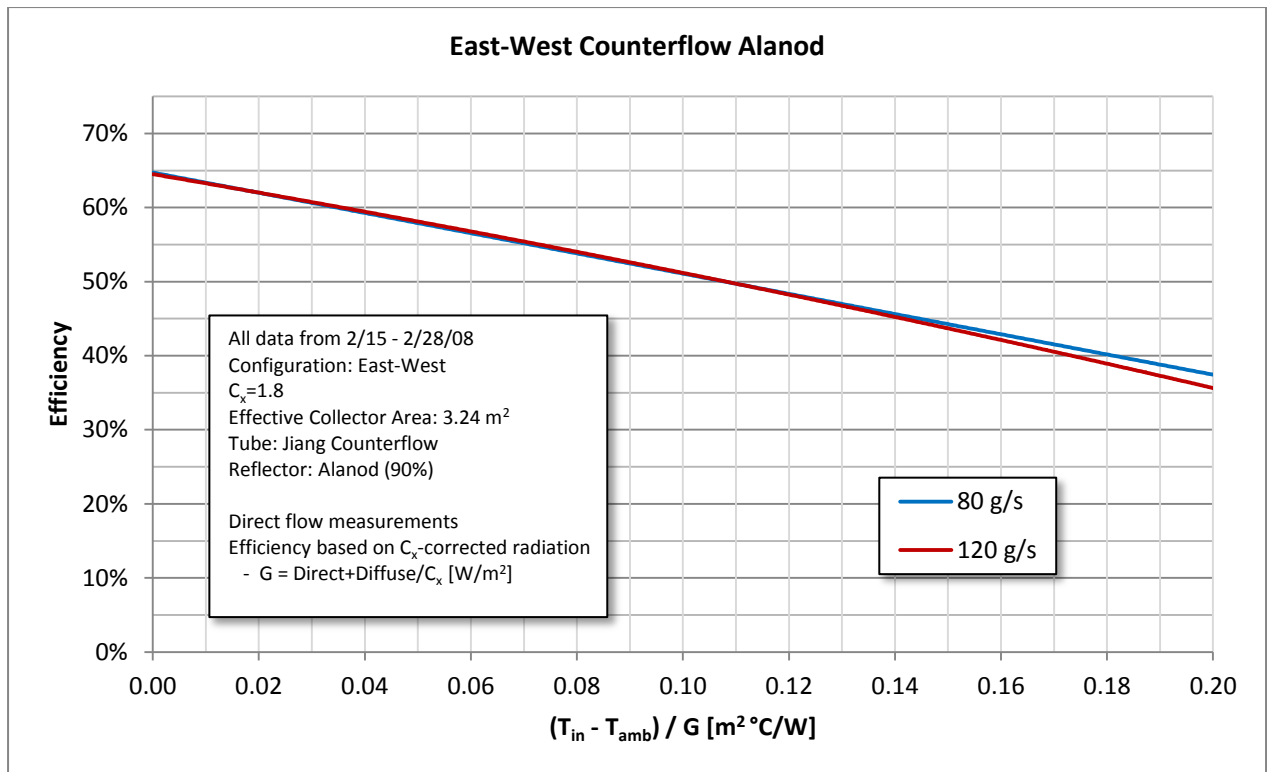


Figure 58. East-West Counterflow with Alanod Effective Reduced Efficiency Curve

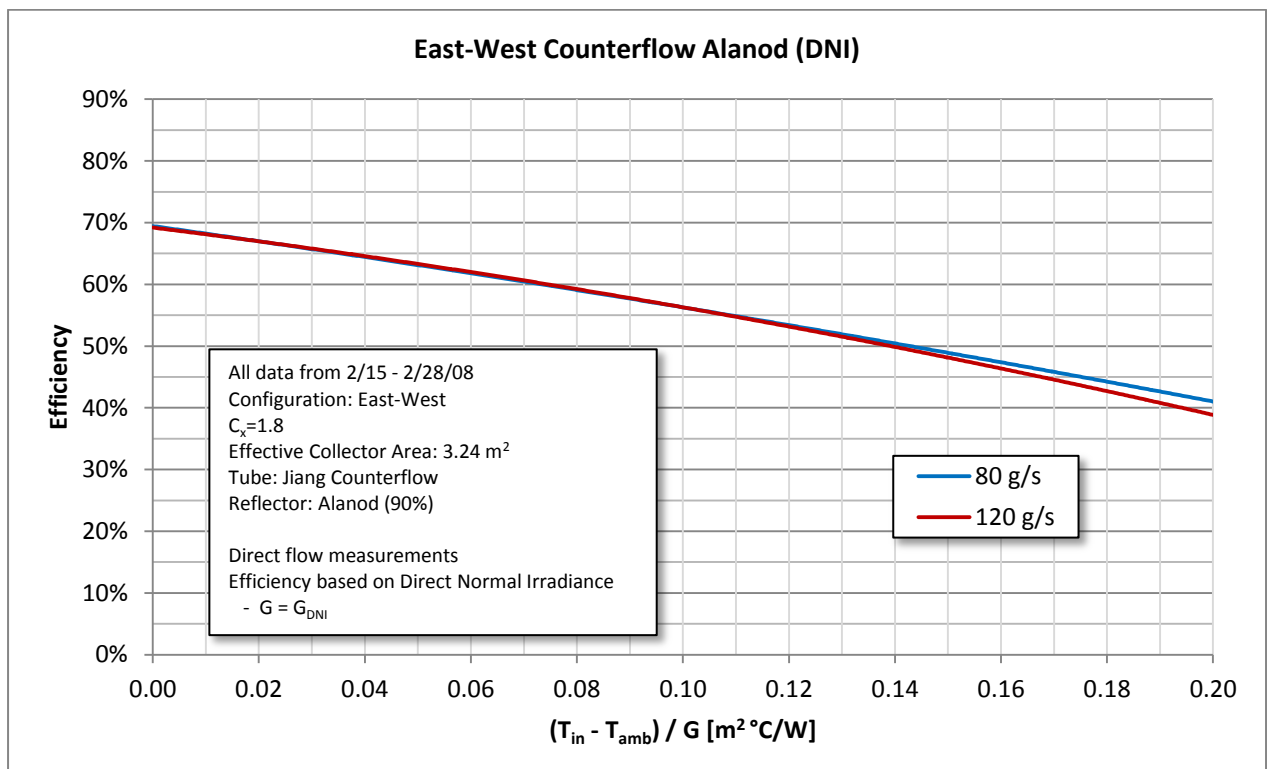


Figure 59. East-West Counterflow with Alanod Direct Reduced Efficiency Curve

Collector Incident Angle Modifier (IAM)

The IAM was not measured for this specific configuration. The IAM was measured for the East-West U-Tube with Reflectech collector with virtually identical geometrical optics and can be used to describe the East-West Counterflow with Alanod collector. Refer to Figure 76 for the IAM chart.

4.2.3. North-South U-Tube with Alanod Collector

Collector description

Table 16. Collector Description of North-South U-Tube with Alanod Collector

Orientation	North-South
Concentration C_x	1.15
Effective Collector Area A_A	2.076 m ²
Tube Type	U-Tube
Number of Tubes	6
Reflector	Alanod (90%)

Collector optical efficiency

The optical efficiency of the North-South Counterflow with Alanod collector was used as an assumed value of the optical efficiency of the North-South U-Tube with Alanod since the geometry and optical properties of the system were assumed to be unchanged.

The optical efficiency based on an effective irradiance, G_{eff} , was assumed to be 69.1%. The optical efficiency based on direct normal irradiance, G_{DNI} , was assumed to be 79.3%.

Collector thermal efficiency

The efficiency of the XCPC was measured from 6/30 - 7/3/08 using the direct flow method at the following collector inlet temperatures: 80°C, 100°C, 120°C, 140°C, 160°C, 180°C, and 200°C; and at the following flow rates: 80 g/s, 100 g/s, 120 g/s, and 140 g/s.

The heat capacity of the oil was measured in August 2008 using the calorimeter during the East-West U-Tube with Alanod tests. A linear approximation to the measurements was used to calculate the efficiency of the collector: $c_p = 0.00489 \cdot T_m + 1.815$.

The performance characteristics are tabulated in Table 17 and the collector efficiencies are depicted in Figure 60 through Figure 62. Figure 60 displays the raw values for the efficiencies. Figure 61 displays the efficiencies based on the effective irradiance G_E while Figure 62 displays the efficiencies based on the direct normal irradiance (DNI) G_{DNI} .

Table 17. Performance Characteristics of North-South U-Tube with Alanod Collector

	$G=G_{\text{eff}}$	$G=G_{\text{DNI}}$
Optical Efficiency η_o	69.1%	79.3%
Efficiency at 100 °C	58.5%	69.3%
Efficiency at 200 °C	36.4%	36.4%
Loss coefficient (1) a_1	1.080 W/m ² -K	0.595 W/m ² -K
Loss coefficient (2) a_2	0.00351 W/m ² -K ²	0.00993 W/m ² -K ²
Overall heat loss coefficient U	1.891 W/m ² -K	2.382 W/m ² -K

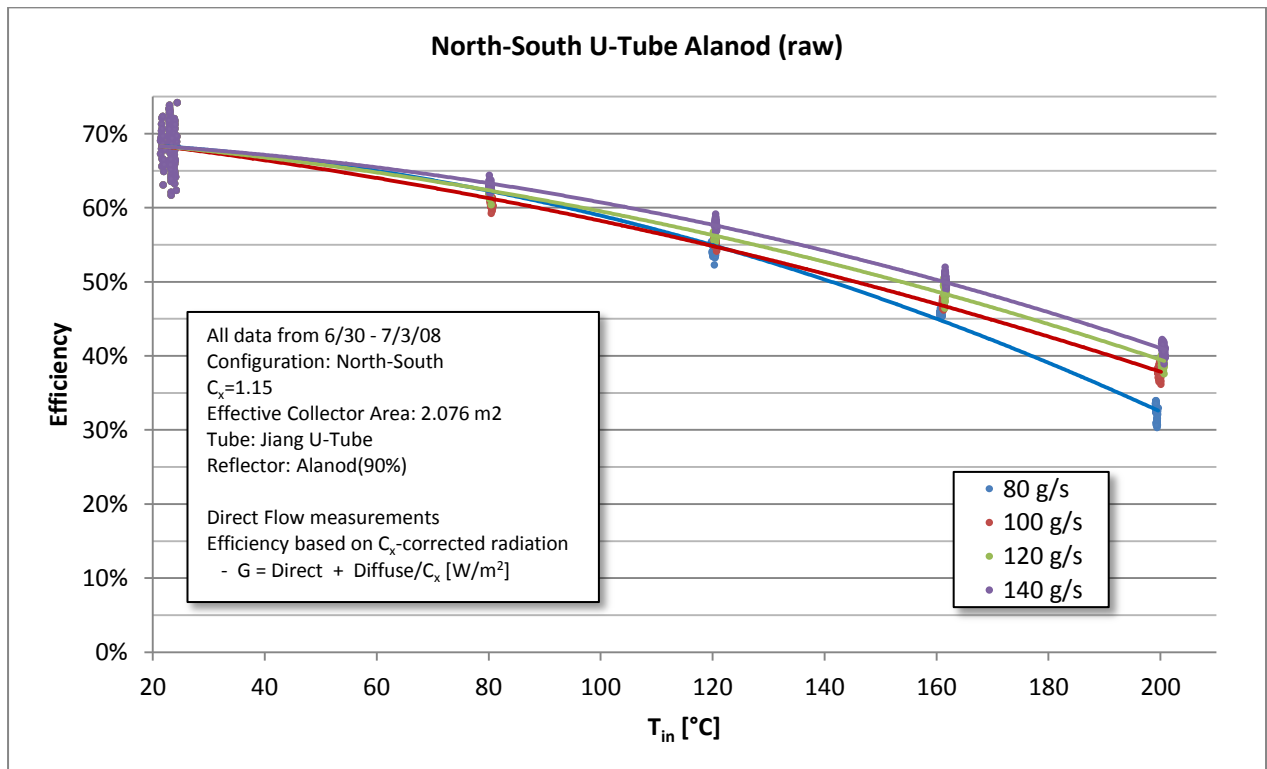


Figure 60. North-South U-Tube with Alanod Raw Efficiency Curve

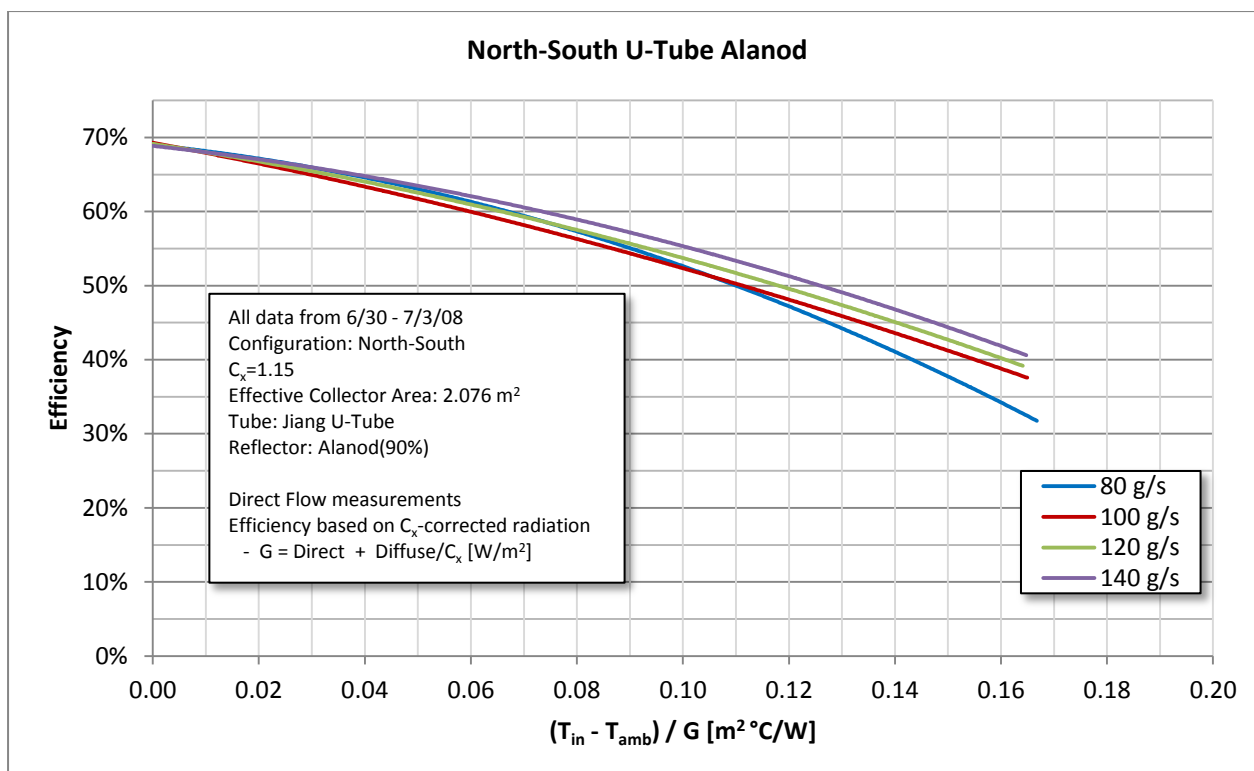


Figure 61. North-South U-Tube with Alanod Effective Reduced Efficiency Curve

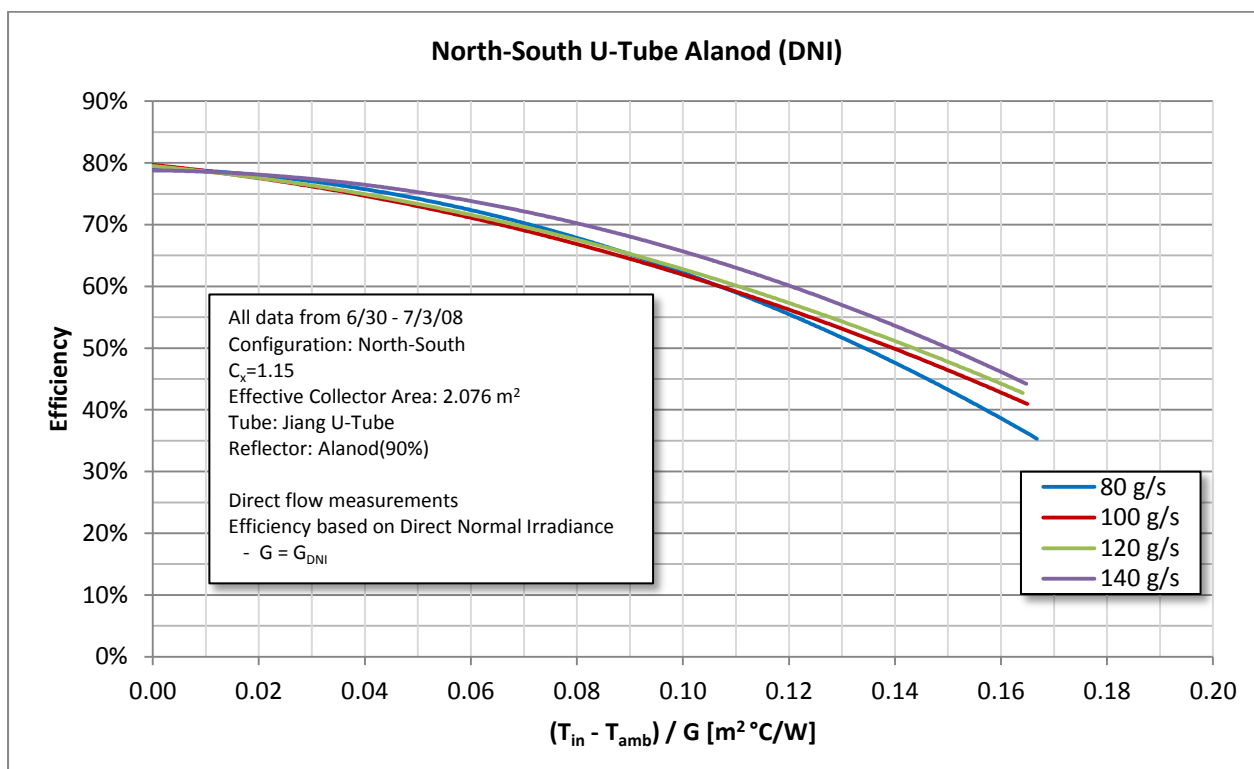


Figure 62. North-South U-Tube with Alanod Direct Reduced Efficiency Curve

Collector Incident Angle Modifier (IAM)

The incident angle modifier (IAM) was not measured for this specific configuration. Since IAM is almost completely dependent on the geometric shape of the reflector and the placement of the tubes, it is reasonable to use the previously measured IAM to describe this collector.

4.2.4. East-West U-Tube with Alanod Collector

Collector description

Table 18. Description of East-West U-Tube with Alanod Collector

Orientation	East-West
Concentration C_x	1.80
Effective Collector Area A_A	3.24 m ²
Tube Type	U-Tube
Number of Tubes	6
Reflector	Alanod (90%)

Collector optical efficiency

The optical efficiency of the East-West U-Tube with Alanod collector was assumed to be the value taken from a linear extrapolation.

The optical efficiency based on an effective irradiance, G_{eff} , was assumed to be 66.4%. The optical efficiency based on direct normal irradiance, G_{DNI} , was assumed to be 71.5%.

Collector thermal efficiency

The efficiency of the XCPC was measured from 8/13 – 8/27/08 using both the direct flow and the calorimetry methods at the following collector inlet temperatures: 80°C, 100°C, 120°C, 140°C, 160°C, 180°C, and 200°C; and at the following flow rates: 80 g/s, 100 g/s, 120 g/s, and 140 g/s. All efficiencies reported are based on the calorimetry method.

The performance characteristics are tabulated in Table 19 and the collector efficiencies are depicted in Figure 63 through Figure 65. Figure 63 displays the raw values for the efficiencies. Figure 64 displays the efficiencies based on the effective irradiance G_E while Figure 65 displays the efficiencies based on the direct normal irradiance (DNI) G_{DNI} .

Table 19. Performance Characteristics of East-West U-Tube with Alanod Collector

	$G=G_{\text{eff}}$	$G=G_{\text{DNI}}$
Optical Efficiency η_o	66.4%	71.5%
Efficiency at 100 °C	58.3%	63.1%
Efficiency at 200 °C	43.2%	45.2%%
Loss coefficient (1) a_1	0.908 W/m ² -K	0.822 W/m ² -K
Loss coefficient (2) a_2	0.00239 W/m ² -K ²	0.00387 W/m ² -K ²
Overall heat loss coefficient U	1.339 W/m ² -K	1.519 W/m ² -K

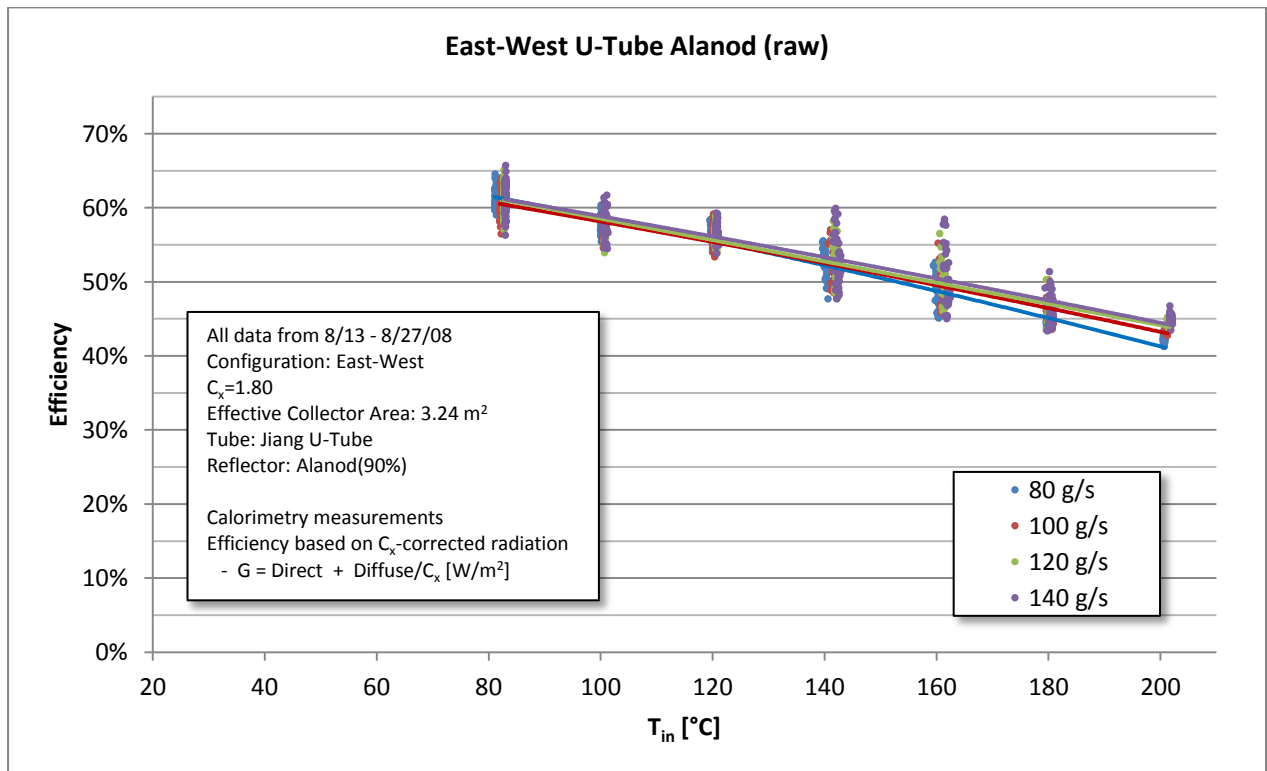


Figure 63. East-West U-Tube with Alanod Raw Efficiency Curve

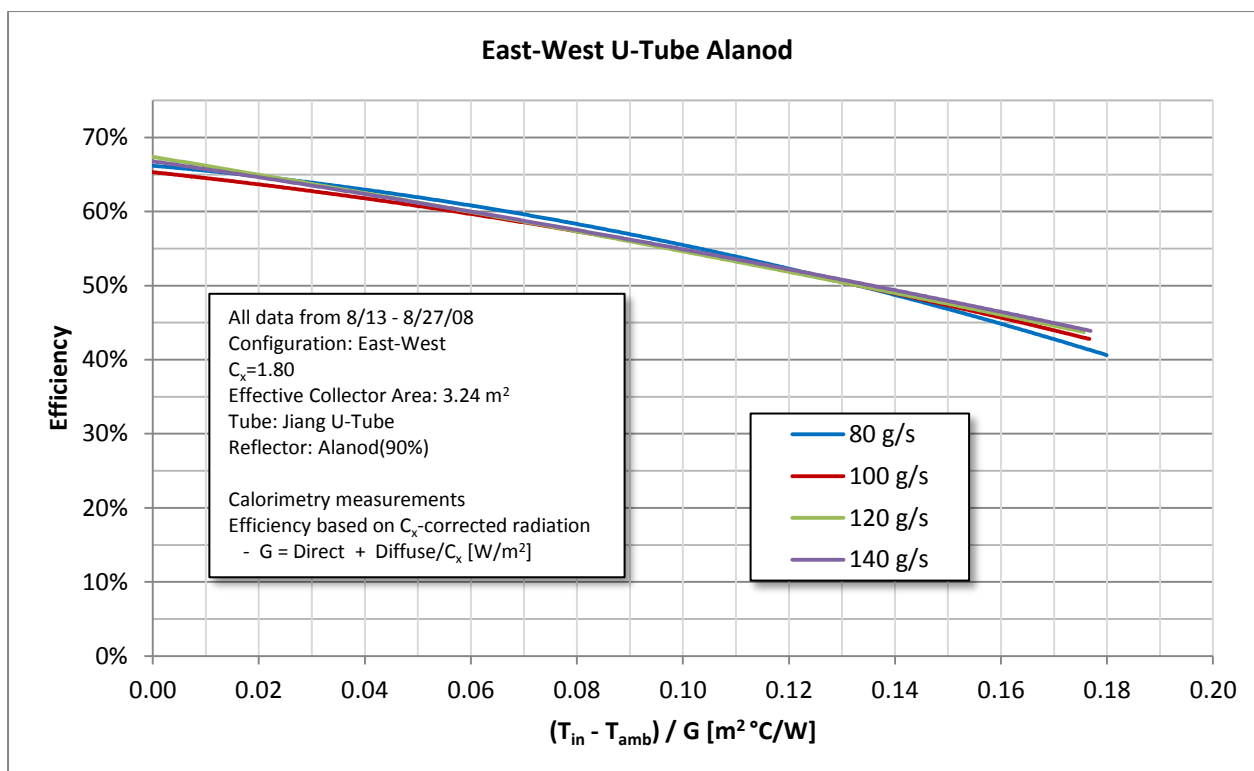


Figure 64. East-West U-Tube with Alanod Effective Reduced Efficiency Curve

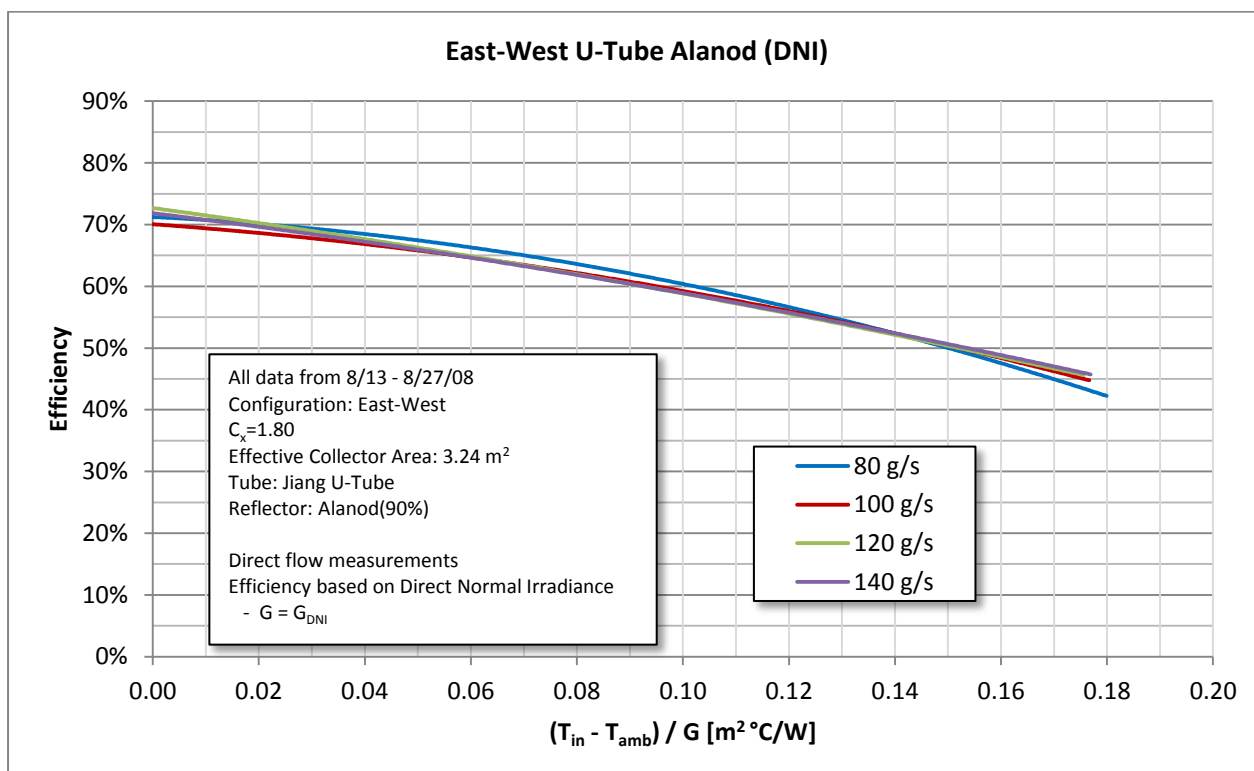


Figure 65. East-West U-Tube with Alanod Direct Reduced Efficiency Curve

Collector Incident Angle Modifier (IAM)

The incident angle modifier (IAM) was not measured for this specific configuration. Since IAM is almost completely dependent on the geometric shape of the reflector and the placement of the tubes, it is reasonable to use the measured IAM from the U-Tube with Reflectech Reflectors in East-West collector to describe this collector.

4.2.5. East-West X-Tube with Alanod Collector

Description of collector

Table 20. Description of East-West T-Tube with Alanod Collector

Orientation	East-West
Concentration C_x	1.80
Effective Collector Area A_A	3.1 m ²
Tube Type	X-Tube
Number of Tubes	6
Reflector	Alanod (90%)

Collector optical efficiency

The optical efficiency of the East-West X-Tube with Alanod collector was assumed to be the value taken from a linear extrapolation.

The optical efficiency based on an effective irradiance, G_{eff} , was assumed to be 68.6%. The optical efficiency based on direct normal irradiance, G_{DNI} , was assumed to be 75.0%.

Collector thermal efficiency

The efficiency of the XCPC was measured from 9/18 – 10/13/08 using both the direct flow and the calorimetry methods at the following collector inlet temperatures: 80°C, 100°C, 120°C, 140°C, 160°C, 180°C, and 200°C; and at the following flow rates: 80 g/s, 100 g/s, 120 g/s, 140 g/s, and 160 g/s. All efficiencies reported are based on calorimetry method.

The performance characteristics are tabulated in Table 21 and the collector efficiencies are depicted in Figure 66 through Figure 68. Figure 66 displays the raw values for the efficiencies. Figure 67 displays the efficiencies based on the effective irradiance G_E while Figure 68 displays the efficiencies based on the direct normal irradiance (DNI) G_{DNI} .

Table 21. Performance Characteristics of East-West X-Tube with Alanod Collector

	$G=G_{\text{eff}}$	$G=G_{\text{DNI}}$
Optical Efficiency η_o	68.6%	75.0%
Efficiency at 100 °C	59.9%	65.9%
Efficiency at 200 °C	39.9%	43.4%
Loss coefficient (1) a_1	0.799 W/m ² -K	0.799 W/m ² -K
Loss coefficient (2) a_2	0.00481 W/m ² -K ²	0.00481 W/m ² -K ²
Overall heat loss coefficient U	1.664 W/m ² -K	1.838 W/m ² -K

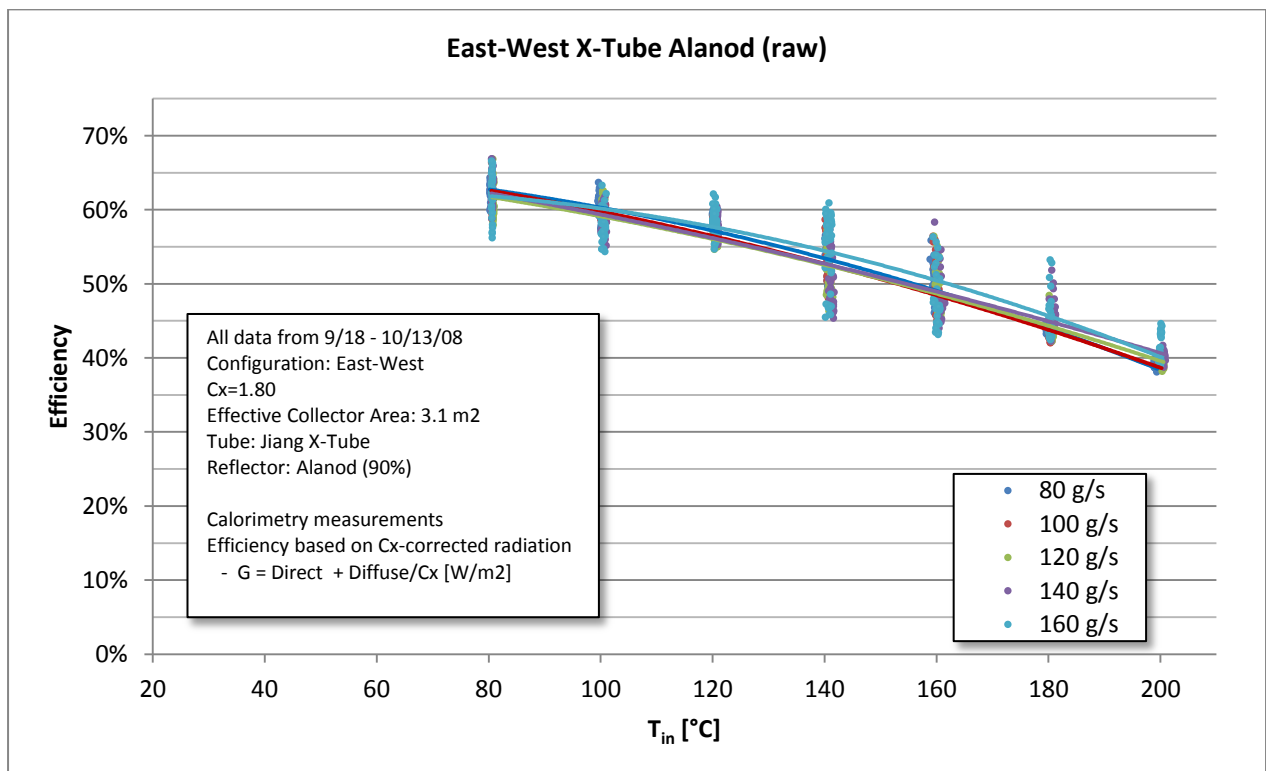


Figure 66. East-West X-Tube with Alanod Raw Efficiency Curve

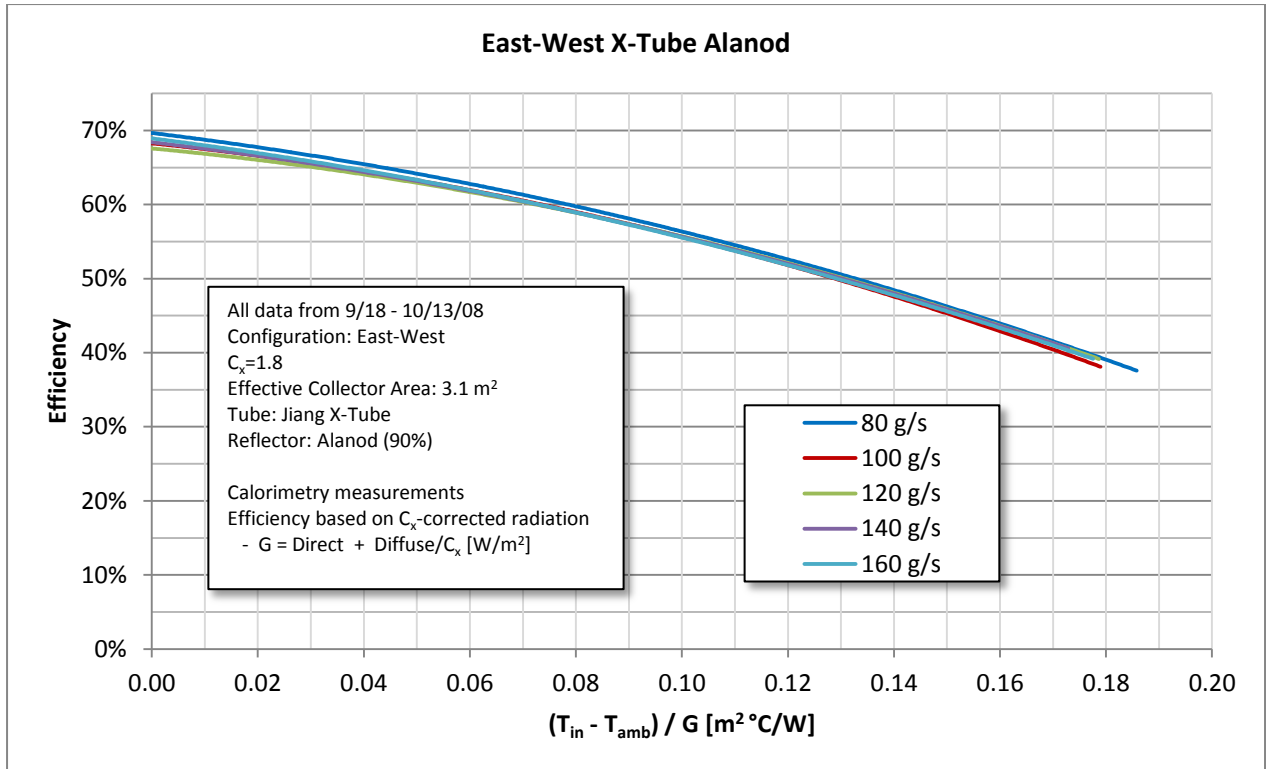


Figure 67. East-West X-Tube with Alanod Effective Reduced Efficiency Curve

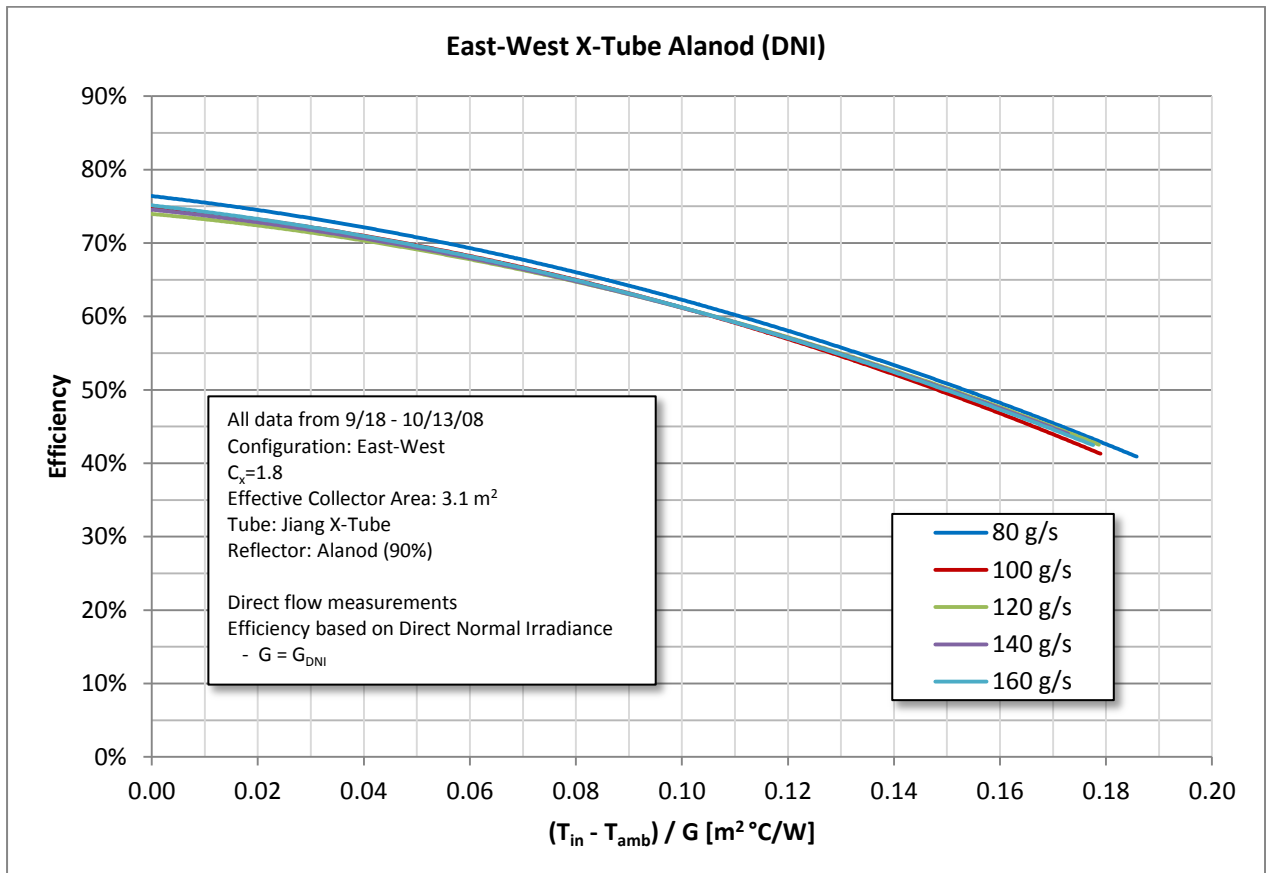


Figure 68. East-West X-Tube with Alanod Direct Reduced Efficiency Curve

Collector Incident Angle Modifier (IAM)

The incident angle modifier (IAM) was not measured for this specific configuration. Since IAM is almost completely dependent on the geometric shape of the reflector and the placement of the tubes, it is reasonable to use the measured IAM from the U-Tube with Reflectech Reflectors in East-West collector to describe this collector.

4.2.6. North-South U-Tube with Reflectech Collector

Collector description

Table 22. North-South U-Tube with Reflectech Collector

Orientation	North-South
Concentration C_x	1.15
Effective Collector Area A_A	2.076 m ²
Tube Type	U-Tube
Number of Tubes	6
Reflector	Reflectech

Collector optical efficiency

The optical efficiency of the North-South U-Tube with Reflectech collector was measured on 10/23/08 with an average inlet temperature of 30°C and an average ambient temperature of 21°C.

The optical efficiency based on an effective irradiance, G_{eff} , was found to be 71.3%. The optical efficiency based on direct normal irradiance, G_{DNI} , was found to be 88.5%.

Collector thermal efficiency

The efficiency of the XCPC was measured from 10/23/08 – 3/19/09 using both the direct flow and the calorimetry methods at the following collector inlet temperatures: 80°C, 100°C, 120°C, 140°C, 160°C, 180°C, and 200°C; and at the following flow rates: 80 g/s, 100 g/s, 120 g/s, 140 g/s, and 160 g/s. All efficiencies reported are based on the calorimetry method.

The performance characteristics are tabulated in Table 23 and the collector efficiencies are depicted in Figure 69 through Figure 71. Figure 69 displays the raw values for the efficiencies. Figure 70 displays the efficiencies based on the effective irradiance G_E while Figure 71 displays the efficiencies based on the direct normal irradiance (DNI) G_{DNI} .

Table 23. Performance Characteristics of North-South U-Tube with Reflectech Collector

	$G=G_{\text{eff}}$	$G=G_{\text{DNI}}$
Optical Efficiency η_o	71.3%	88.5%
Efficiency at 100 °C	61.9%	71.7%
Efficiency at 200 °C	35.8%	43.3%
Loss coefficient (1) a_1	0.664 W/m ² -K	1.975 W/m ² -K
Loss coefficient (2) a_2	0.00780 W/m ² -K ²	0.00348 W/m ² -K ²
Overall heat loss coefficient U	2.068 W/m ² -K	2.602 W/m ² -K

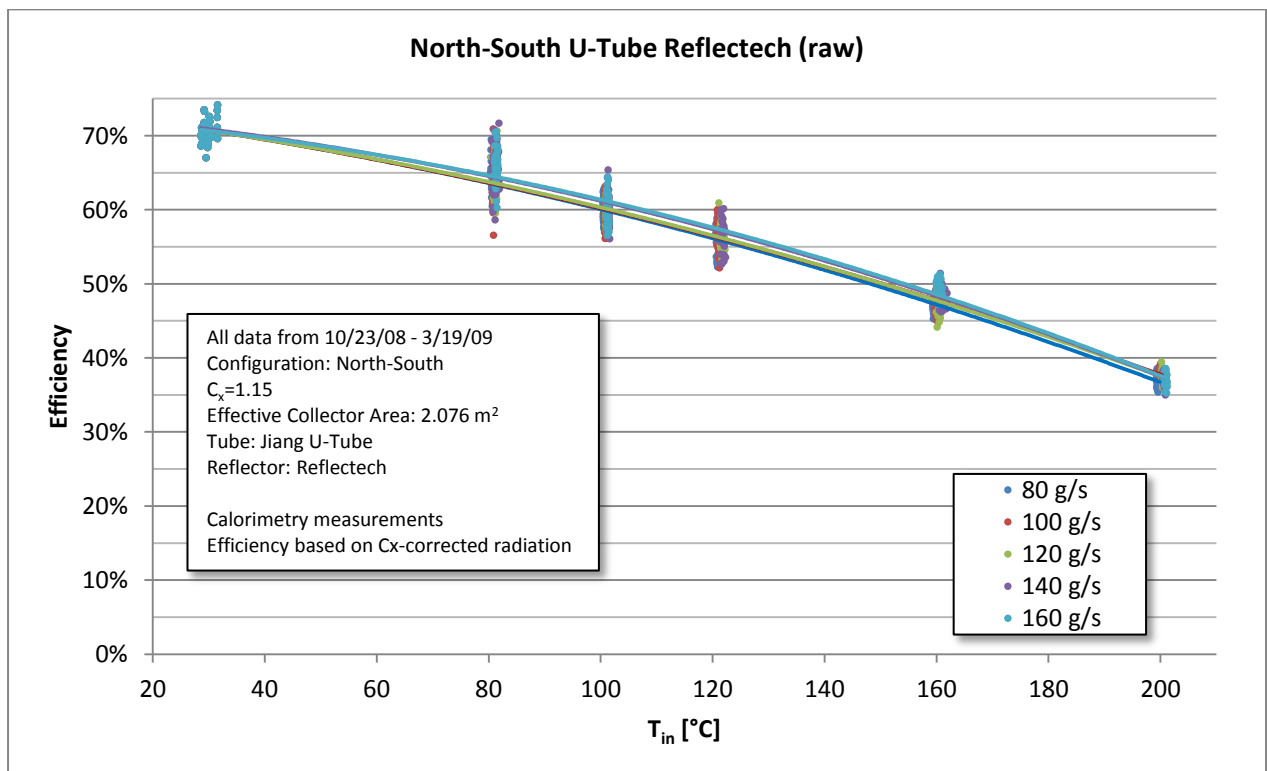


Figure 69. North-South U-Tube with Reflectech Raw Efficiency Curve

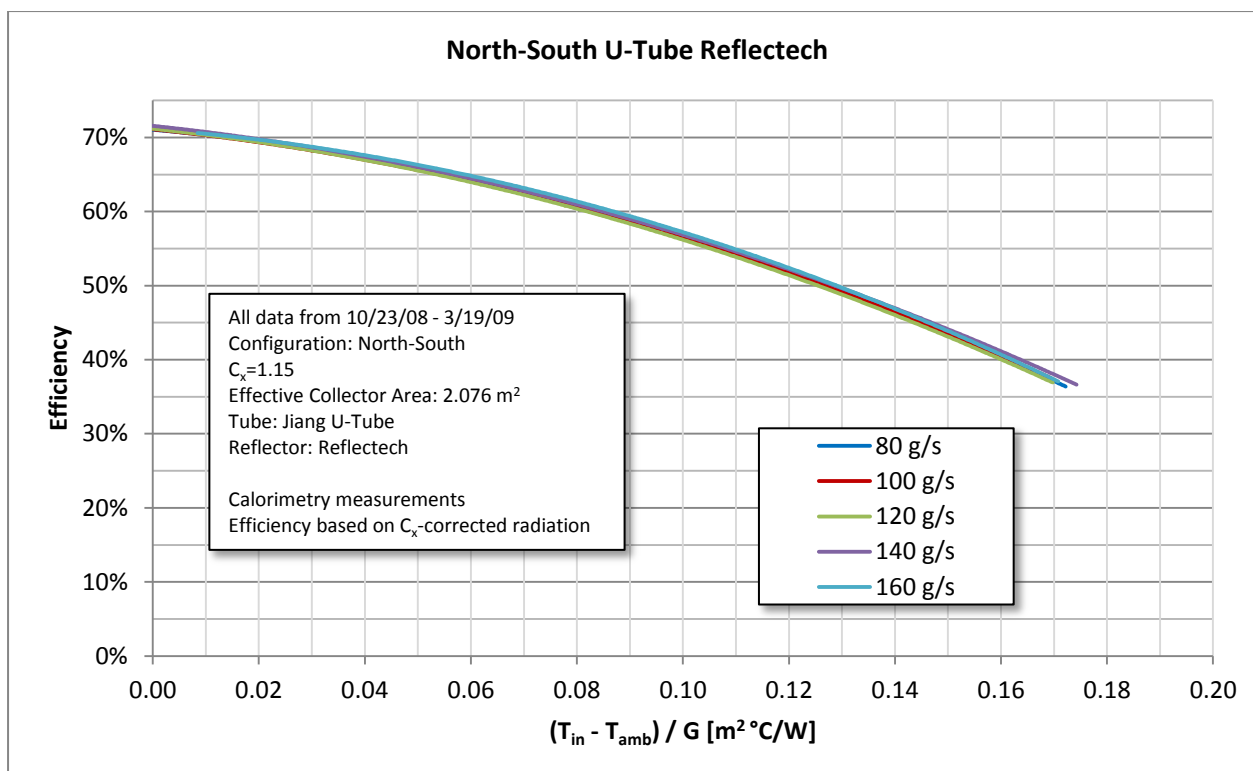


Figure 70. North-South U-Tube with Reflectech Effective Reduced Efficiency Curve

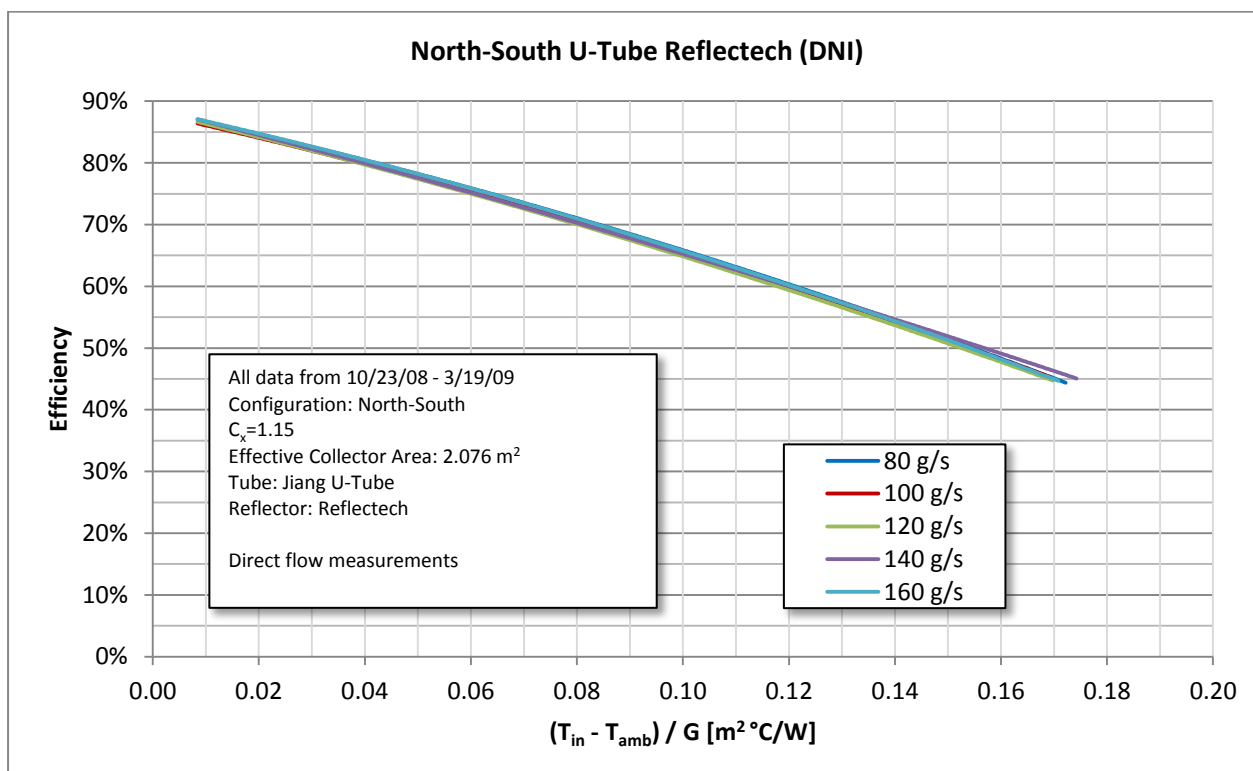


Figure 71. North-South U-Tube with Reflectech Direct Reduced Efficiency Curve

Stagnation Test

A U-tube filled with oil was mounted in an individual collector on a separate tracker to test for stagnation. Temperatures were measured on the tube's glass T_{glass} , on the outside of the pipe-to-manifold connection T_{outer} , and roughly two feet into the oil-filled inlet pipe T_{inside} . Ambient temperature, PSP, NIP, wind speed and direction measurements were also taken. The test conditions are described in Table 24.

Table 24. Stagnation test conditions for North-South U-Tube with Reflectech

Average T_{amb}	25°C
Average G_{direct}	823 W/m ²
Average G_{hemi}	1030 W/m ²
Average %Diffuse	20%
Average wind speed	1.6 m/s

The maximum temperature measured inside the tube was 289°C. The inside temperature reached 283°C 60 minutes after the tube was exposed to sunlight. No apparent damage to the tube was reported after the test was completed.

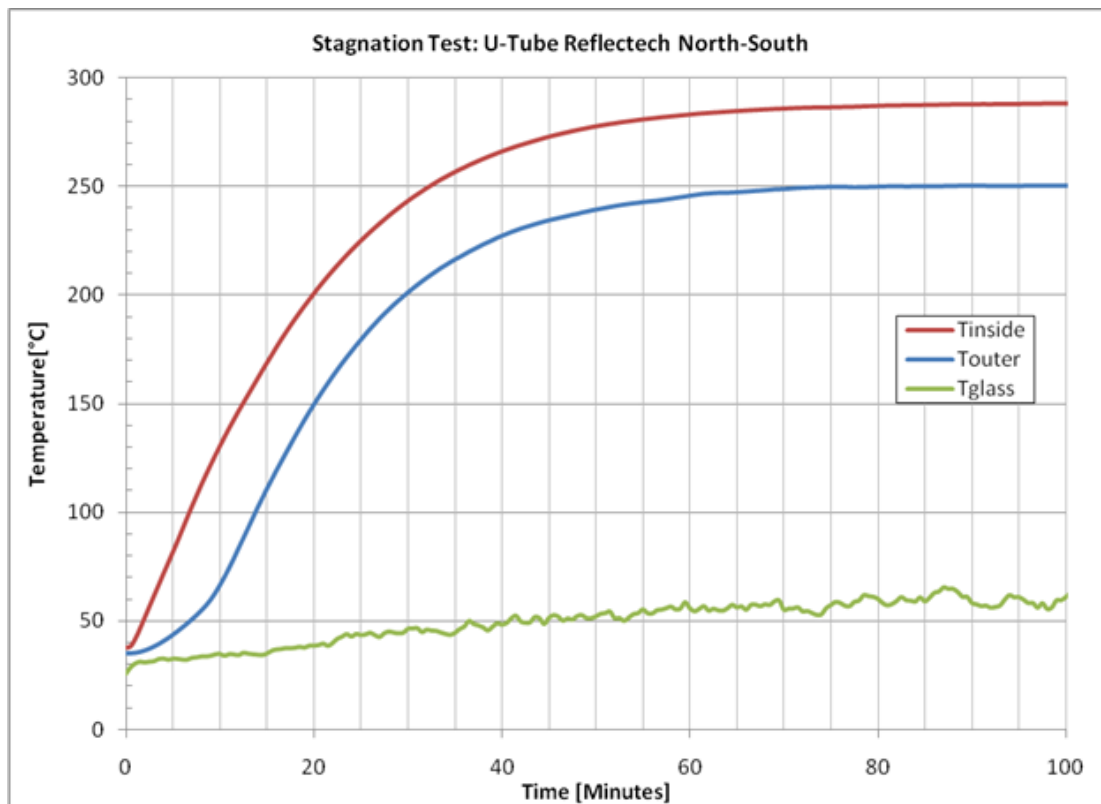


Figure 72. Stagnation results for North-South U-Tube with Reflectech

Collector Incident Angle Modifier (IAM)

The incident angle modifier (IAM) was not measured for this specific configuration. Since IAM is almost completely dependent on the geometric shape of the reflector and the placement of the tubes, it is reasonable to use the measured IAM from the Counterflow-Tube with Alanod Reflectors in North-South orientation collector to describe this collector.

4.2.7. East-West U-Tube with Reflectech Collector

Collector description

Table 25. Description of East-West U-Tube with Reflectech Collector

Orientation	East-West
Concentration C_x	1.15
Effective Collector Area A_A	3.24 m ²
Tube Type	U-Tube
Number of Tubes	6
Reflector	Reflectech

Collector optical efficiency

The optical efficiency of the East-West U-Tube with Alanod collector was assumed to be the value taken from a linear extrapolation.

The optical efficiency based on an effective irradiance, G_{eff} , was assumed to be 64.4%. The optical efficiency based on direct normal irradiance, G_{DNI} , was assumed to be 69.7%.

Collector thermal efficiency

The efficiency of the XCPC was measured from 7/1 – 9/16/08 using both the direct flow and the calorimetry methods at the following collector inlet temperatures: 80°C, 100°C, 120°C, 140°C, 160°C, 180°C, and 200°C; and at the following flow rates: 80 g/s, 100 g/s, 120 g/s, 140 g/s, and 160 g/s. All efficiencies reported are based the calorimetry method.

The performance characteristics are tabulated in Table 26 and the collector efficiencies are depicted in Figure 73 through Figure 75. Figure 73 displays the raw values for the efficiencies. Figure 74 displays the efficiencies based on the effective irradiance G_E while Figure 76 displays the efficiencies based on the direct normal irradiance (DNI) G_{DNI} .

Table 26. Performance Characteristics of East-West U-Tube with Reflectech Collector

	$G=G_{\text{eff}}$	$G=G_{\text{DNI}}$
Optical Efficiency η_o	64.4%	69.7%
Efficiency at 100 °C	58.1%	62.6%
Efficiency at 200 °C	41.7%	46.0%
Loss coefficient (1) a_1	0.488 W/m ² -K	0.633 W/m ² -K
Loss coefficient (2) a_2	0.00463 W/m ² -K ²	0.00411 W/m ² -K ²
Overall heat loss coefficient U	1.321 W/m ² -K	1.373 W/m ² -K

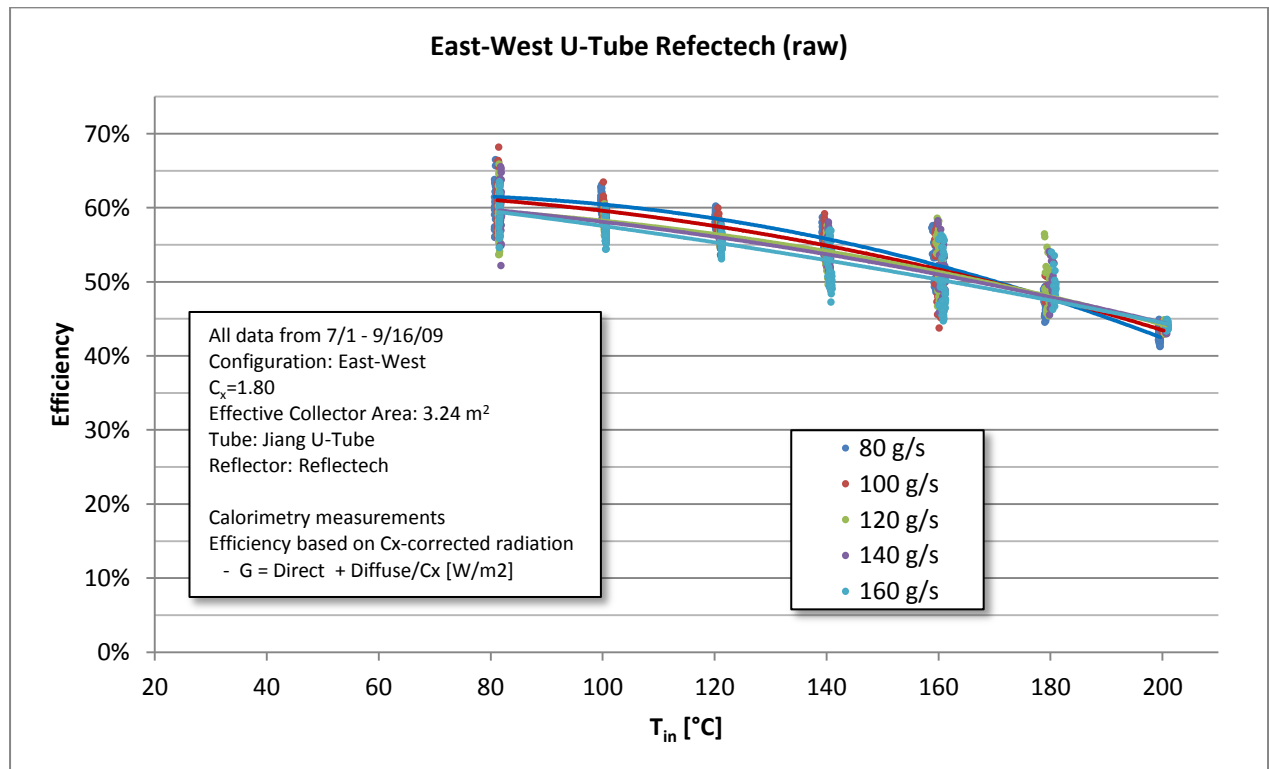


Figure 73. East-West U-Tube with Reflectech Raw Efficiency Curve

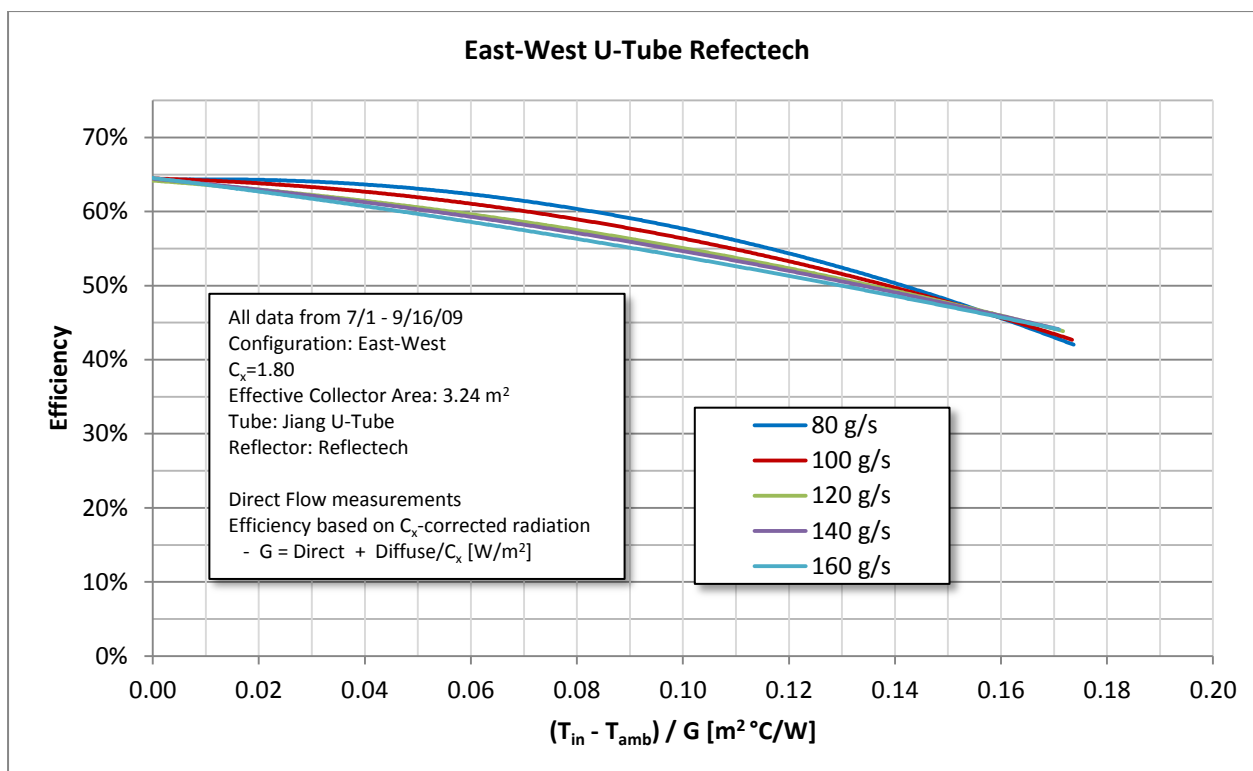


Figure 74. East-West U-Tube with Refectech Effective Reduced Efficiency Curve

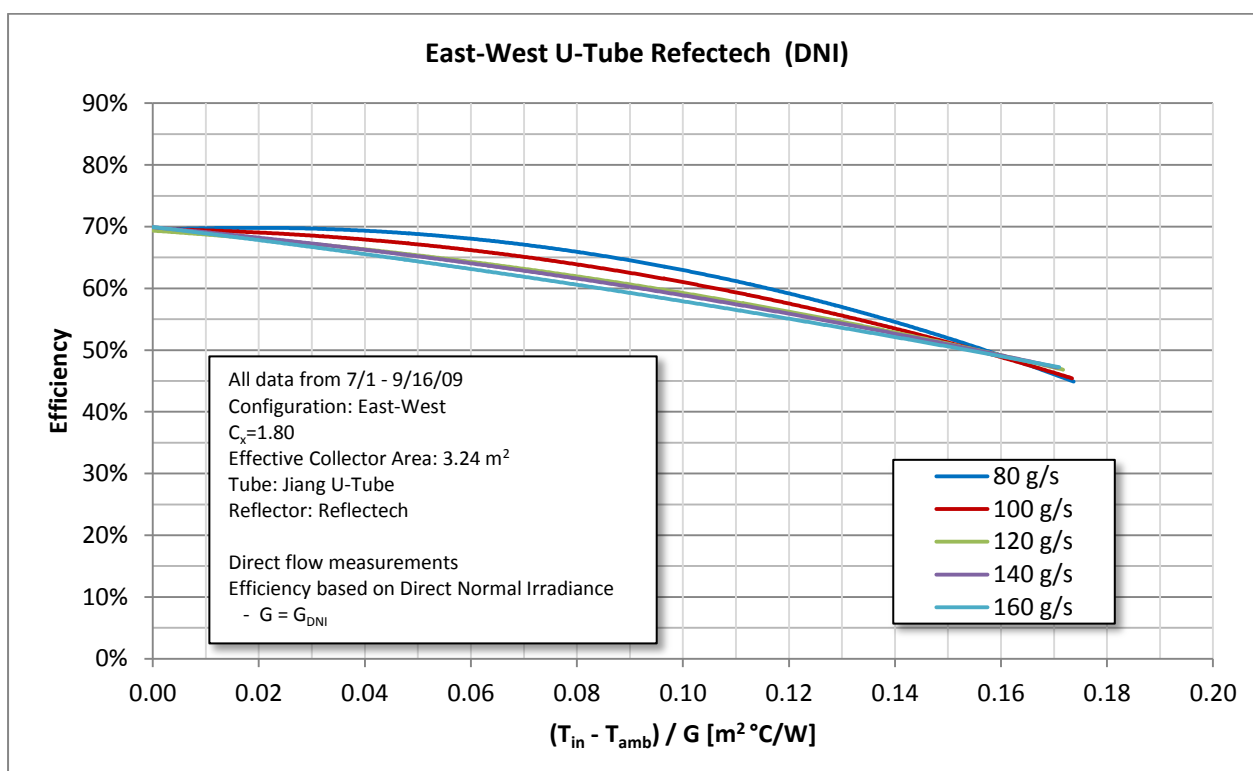


Figure 75. East-West U-Tube with Refectech Direct Reduced Efficiency Curve

Collector Incident Angle Modifier (IAM)

The IAM was measured at an inlet temperature of 120 °C. In this measurement the instantaneous efficiency was based on the direct normal insolation only that was measured with a Normal Incidence Pyrheliometer on a separate tracker. Figure 76 shows the relative drop in efficiency during the test as the sun angle varies between 0° and 45° relative to normal incidence. At roughly 32.5°, the collector performs at 90% of the nominal efficiency.

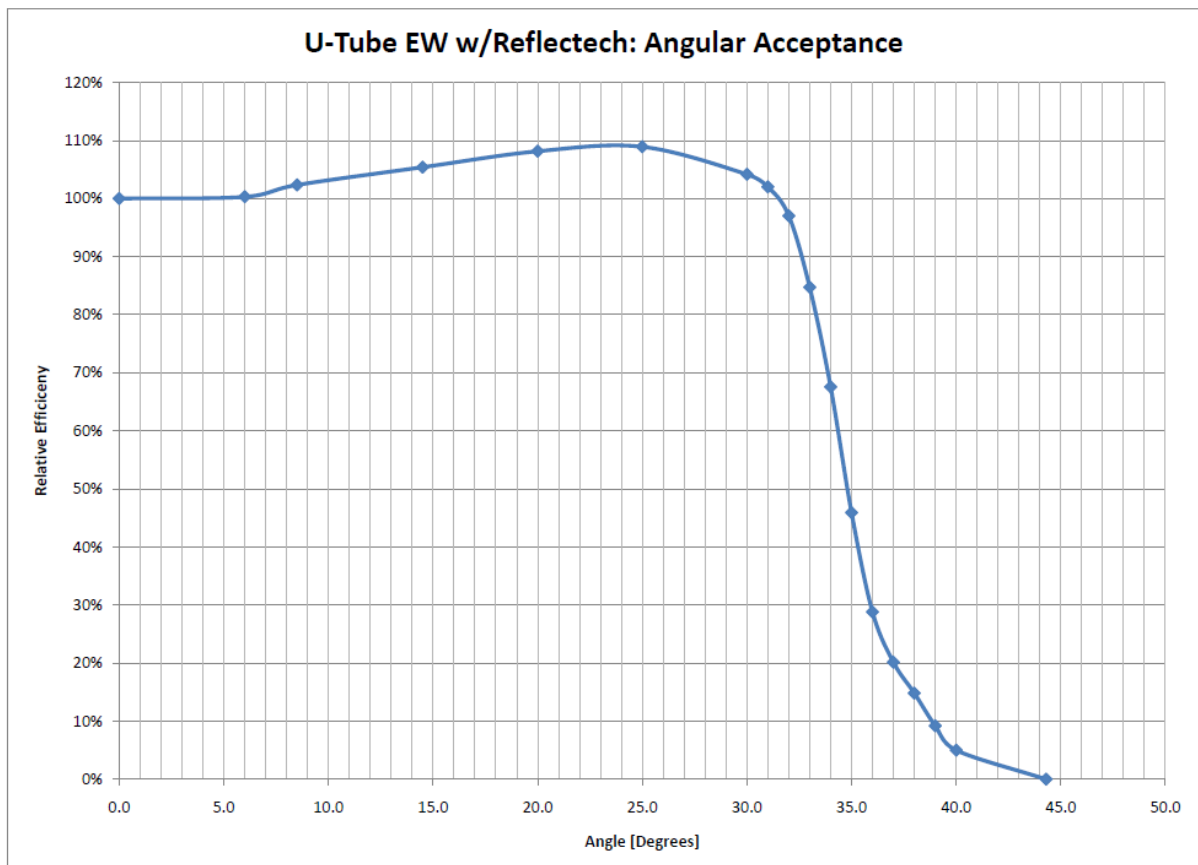


Figure 76. East-West U-Tube with Reflectech: IAM Chart

4.2.8. Summary of Results

Table 27 and Table 28 are a summary of the efficiencies of all of the collectors tested based on the effective irradiance and DNI, respectively.

Table 27. Performance Summary of All Collectors Based on Effective Irradiation

	NS AL CF	EW AL CF	NS AL UT	EW AL UT	EW AL XT	NS RT UT	EW RT UT
η_o	69.5%	64.62%	69.1%	66.4%	68.6%	71.3%	64.4%
$\eta(100^\circ\text{C})$	57.2%	54.61%	58.5%	58.3%	59.9%	61.9%	58.1%
$\eta(200^\circ\text{C})$	36.3%	40.29%	36.4%	43.2%	39.9%	35.8%	41.7%
a_1	1.445	1.293	1.080	0.908	0.799	0.664	0.488
a_2	0.00258	0.00070	0.00351	0.00239	0.00481	0.00780	0.00463
U	1.910	1.393	1.891	1.339	1.664	2.068	1.321

Table 28. Performance Summary of All Collectors Based on Direct Normal Irradiation

	NS AL CF	EW AL CF	NS AL UT	EW AL UT	EW AL XT	NS RT UT	EW RT UT
η_o	87.7%	69.33%	79.3%	71.5%	75.0%	88.5%	69.7%
$\eta(100^\circ\text{C})$	72.2%	59.85%	69.3%	63.1%	65.9%	71.7%	62.6%
$\eta(200^\circ\text{C})$	45.2%	44.33%	36.4%	45.2%	43.4%	43.3%	46.0%
a_1	1.793	1.139	0.595	0.822	0.756	1.975	0.633
a_2	0.00363	0.00207	0.00993	0.00387	0.00601	0.00348	0.00411
U	2.447	1.436	2.382	1.519	1.838	2.602	1.373
%Diffuse	23%	15%	15%	11%	15%	17%	11%

4.3. Discussion

4.3.1. North-South Counterflow with Alanod

Figure 77 compares the measured efficiency with the modeled efficiency of the North-South Counterflow with Alanod collector assuming $1,000 \text{ W/m}^2$ effective irradiance and an ambient temperature of 25°C . The “Measured” values in Figure 77 and in this discussion were measured at a flow rate of 80 g/s . The efficiencies referenced in Figure 77 compare the useful power out of the collector to the effective irradiance over the collector’s effective area:

$$\eta = \frac{P_{out}}{G_E A_A}$$

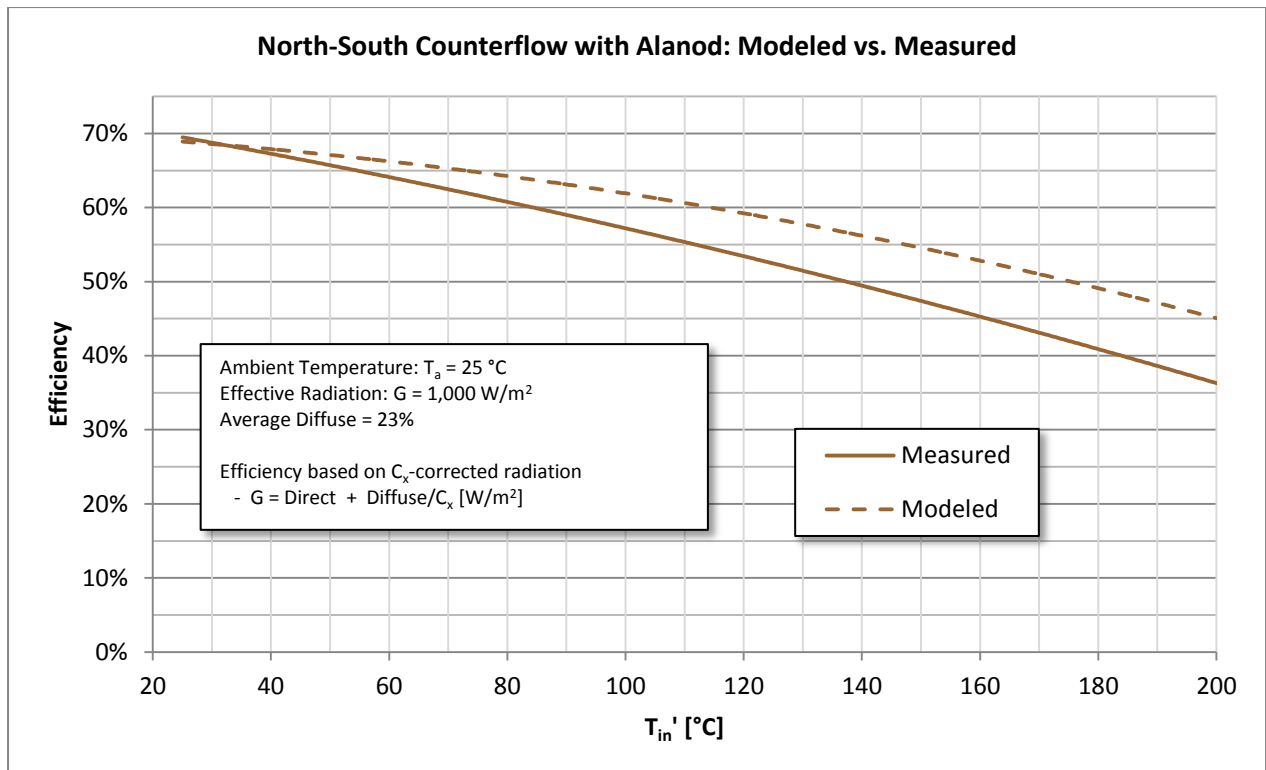


Figure 77. North-South Counterflow with Alanod: Measured vs. Model

The measured optical efficiency at 69.5% was slightly higher than the expected modeled optical efficiency (69.0%). The efficiency of this collector measured at 200°C (37.2%) is roughly eight percentage points less than what the model predicted at 45.0%. These indicate that the performance of the prototype appears to be slightly less than what the model predicted. Overall, the measurements of the optical and thermal efficiency appear to have a very good agreement with the model.

As seen in Figure 6, the acceptance angle of the North-South Counterflow with Alanod collector was found to be ± 55 degrees as opposed to the designed ± 60 degrees which suggests that the optics of the system are not exactly as designed. One possible defect is the shape of the reflector is not accurate. A more likely reason for the lowered acceptance angle is that the placement of the absorber may not have been in the designed position. If the absorber is lower than the designed position then the acceptance angle will be lowered while also increasing the optical efficiency at normal incidence which may also explain the higher than expected optical efficiency. This could happen if either the glass tubes' placement in the frame's holes were off or the absorber in the glass tube was not exactly concentric.

In addition to a lower than predicted acceptance angle, the IAM chart seems to be off center. The fact that the measurements were done continuously throughout the day, the shift in the chart is likely due to a thermal constant.

Efficiencies based on DNI appear very high. These high efficiencies are due to the fact that this collector was tested when there was a relatively large percentage of diffuse light. During the testing of this collector, the percent diffuse ranged between 15% and 30% with an average of 23%.

4.3.2. East-West Counterflow with Alanod

Figure 78 compares the measured efficiency with the modeled efficiency of the North-South Counterflow with Alanod collector assuming 1000 W/m² effective irradiance and an ambient temperature of 25°C. The “Measured” values in Figure 78 and in this discussion were measured at a flow rate of 80 g/s. The efficiencies referenced in Figure 78 compare the useful power out of the collector to the effective irradiance over the collector’s effective area:

$$\eta = \frac{P_{out}}{G_E A_A}.$$

The optical efficiency value used for the measured chart was an assumed value of 64.6%. Since the least squared quadratic curve has a natural shape, the assumed optical efficiency appears to fit the rest of the data.

The measured efficiency at 200°C in Figure 78 is 40.3% compared to the model efficiency of 50.0%. The thermal efficiency of the East-West Counterflow with Alanod collector appears to suffer from more heat loss than what was expected from the model. This lower efficiency is likely, in part, due to a high thermal resistance in the counterflow tubes. This high resistance and the higher concentration ratio of the East-West collector would allow the absorber temperature to be much higher than the oil temperature resulting in a large radiative loss from the absorber. In addition, the efficiency curve in Figure 78 is nearly linear which suggests that there is a large portion of the heat loss that is not due to radiation and can be assumed to be from losses in the manifold insulation.

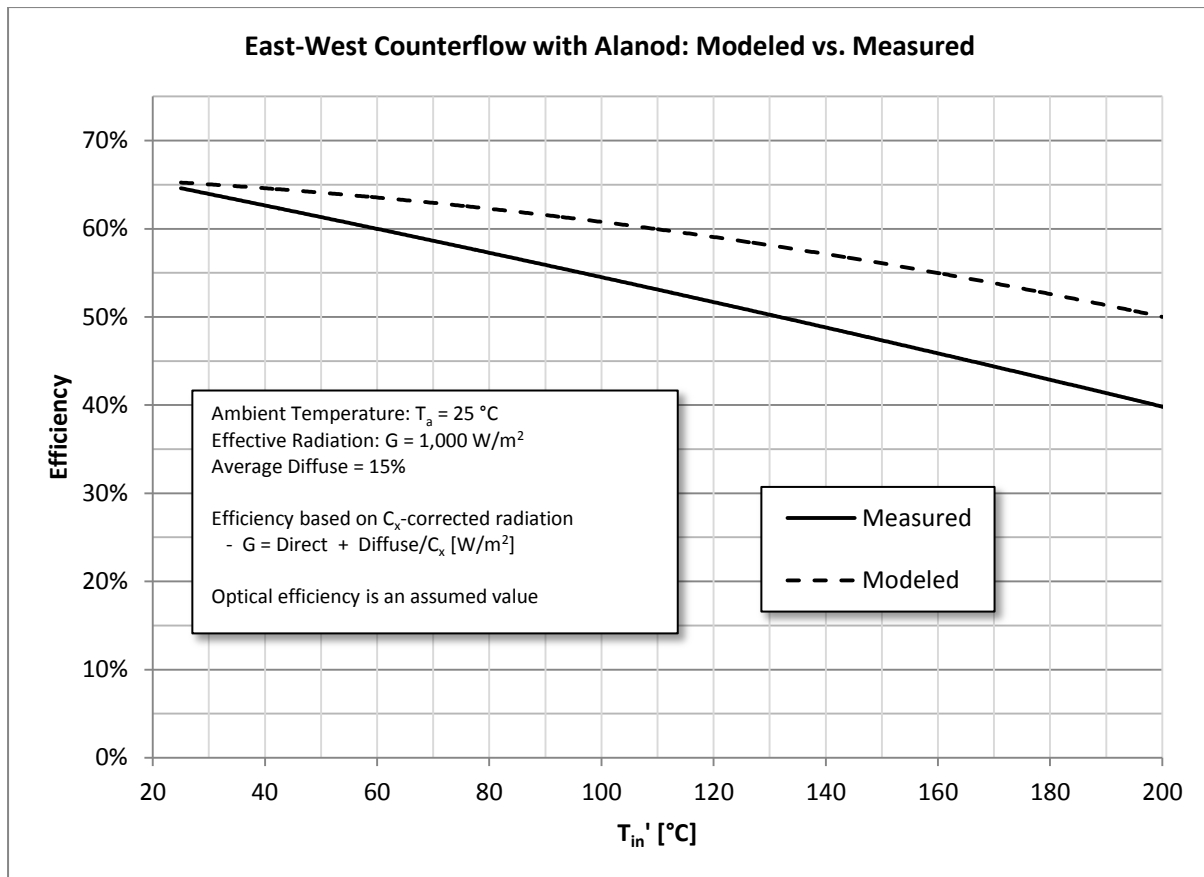


Figure 78. East-West Counterflow with Alanod: Measured vs. Model

Efficiencies based on effective irradiance in Figure 8 are roughly 9% lower than the efficiencies based on DNI in Figure 10 for this East-West collector. With an average diffuse of 15% during testing and a concentration of 1.8, one would expect an 8% difference in the efficiency between DNI and effective irradiance. The amount of diffuse accepted by the collector appears to agree with factor in the effective irradiance calculations.

4.3.3. Comparison between North-South and East-West Counterflow with Alanod collectors

Table 29 compares the efficiencies of the North-South and the East-West Counterflow with Alanod collectors. As expected, the North-South version has a higher optical efficiency. The North-South collector outperformed the East-West collector from temperatures up to $150^{\circ}C$ while the model suggests that the East-West collector should have a higher efficiency starting at about $85^{\circ}C$. As stated earlier, the East-West collector likely suffered from a large thermal resistance in the absorber and manifold heat losses which contributed to its lowered efficiency.

Table 29. Comparison of the North-South and East-West Counterflow with Alanod collectors

	G=G_{eff}		G=G_{DNI}	
	North-South	East-West	North-South	East-West
Optical Efficiency η_o	69.5%	64.6%	87.7%	69.3%
Efficiency at 100 °C	57.2%	54.6%	73.7%	59.9%
Efficiency at 200 °C	36.3%	40.3%	53.3%	44.3%
Loss coefficient (1) a_1	1.445 W/m ² -K	1.293 W/m ² -K	1.793 W/m ² -K	1.139 W/m ² -K
Loss coefficient (2) a_2	.00323 W/m ² -K ²	0.0007 W/m ² -K ²	.0045 W/m ² -K ²	.0021 W/m ² -K ²
Overall heat loss coefficient U	1.910 W/m ² -K	1.393 W/m ² -K	1.973 W/m ² -K	1.436 W/m ² -K
Acceptance angle ⁷	+/- 55°	+/- 32.5°	+/- 55°	+/- 32.5°

4.3.4. Improvements to North-South Collector (U-Tube and Reflectech)

Figure 79 and Figure 80 compare the improved North-South collectors with the original design, North-South Counterflow with Alanod collector. The charts assume that the ambient temperature is 25°C and the effective irradiance is 1000 W/m². The efficiencies shown in Figure 79 and Figure 80 are based on effective irradiance and DNI respectively.

The U-tube with Alanod version was designed to improve the performance of the collector by reducing the thermal resistance inside of the tube. In Figure 79, one can see that by simply replacing the counterflow tube with a U-tube virtually had no effect. This is likely due to the fact that the counterflow tube version performed very well and therefore the thermal resistance in the counterflow tube was reasonable.

⁷ The acceptance angle of the East-West Counterflow Alanod collector can be assumed to be the same as the U-Tube Reflectech version as presented in the table.

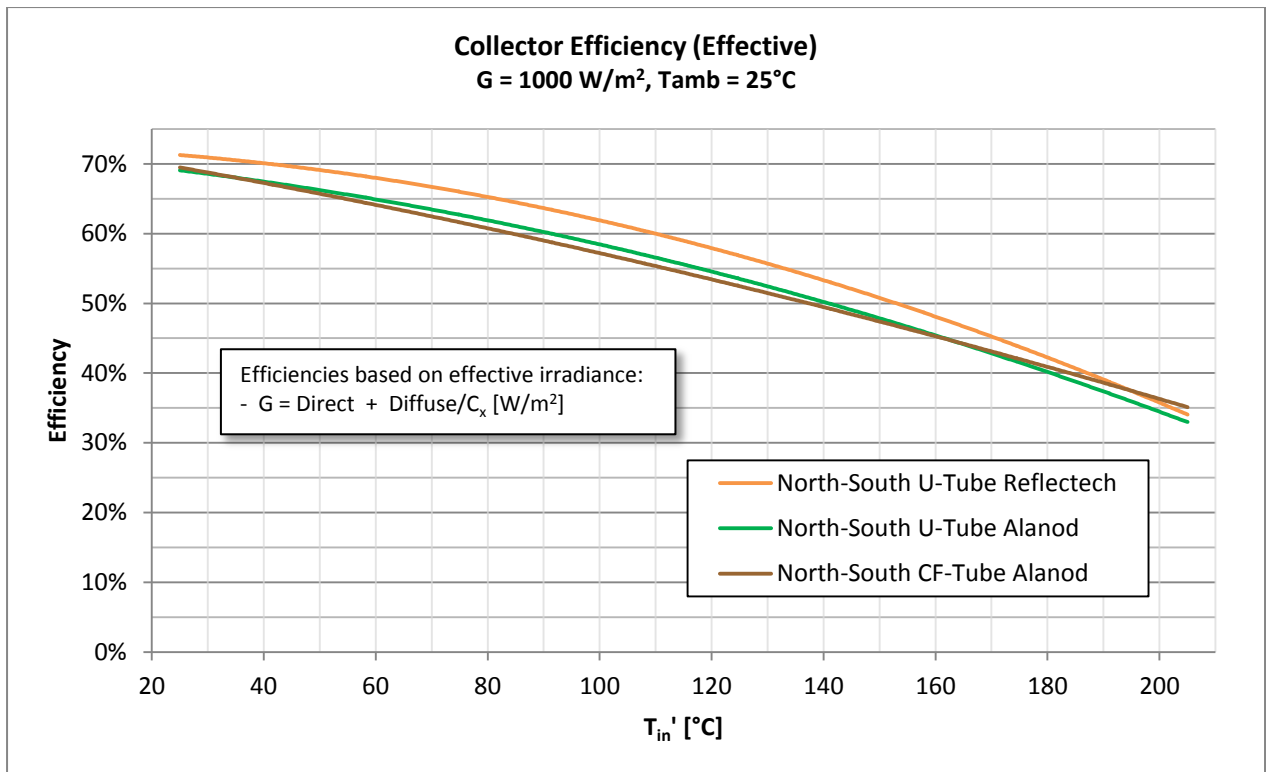


Figure 79. North-South Collector Efficiency (Effective)

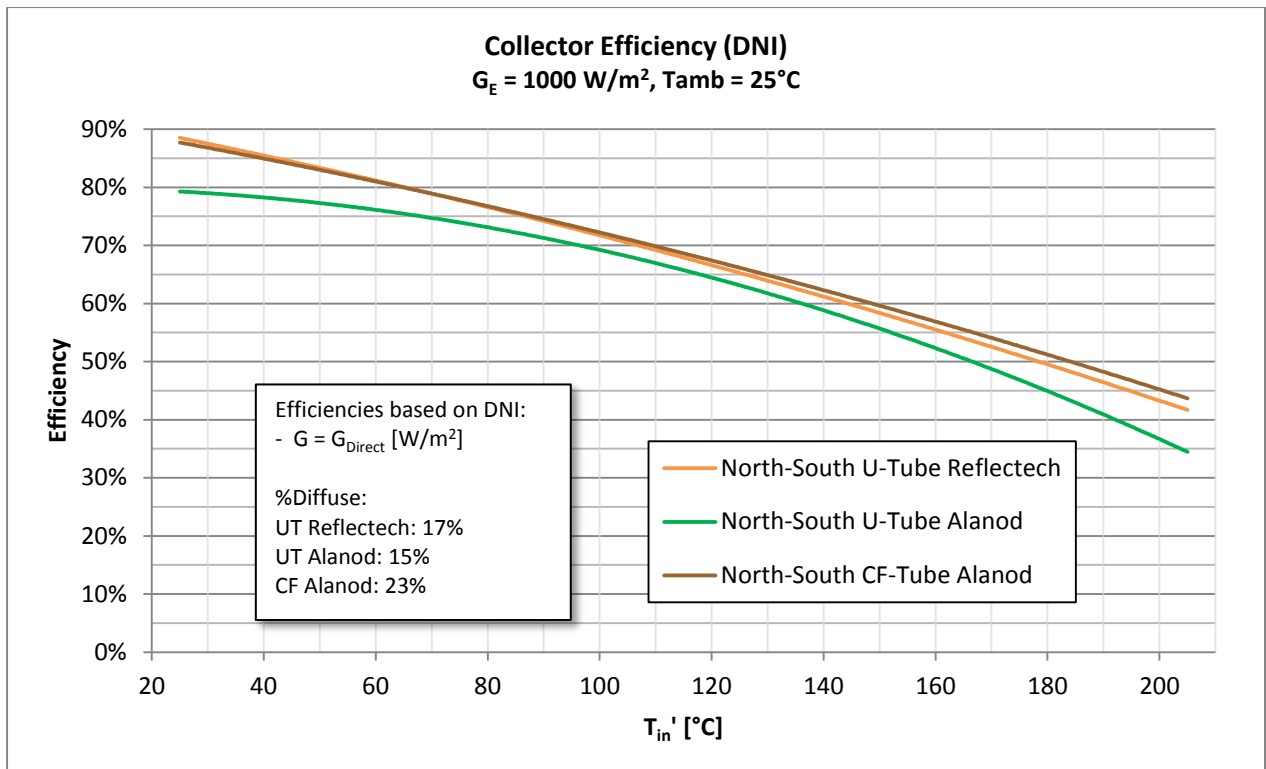


Figure 80. North-South Collector Efficiency (DNI)

The Reflectech design was intended to improve the optical efficiency of the collector. The measured optical efficiency gain from applying Reflectech was roughly 2.5% as opposed to

the expected 4%. One possible reason for the optical efficiency gain not being as expected is that the Reflectech film was difficult to apply to the Alanod reflectors and this resulted in bubbles under the film and scratches on the surface of the film.

The overall performance of the Reflectech version, as seen in Figure 24, was better than the Alanod versions for most temperatures. At temperatures higher than 180°C, the efficiency of the Reflectech version appears to converge with the Alanod version. This poor performance at higher temperatures is likely due to the differences in the ambient temperatures that the collectors were tested. The U-Tube Reflectech version was tested with an average ambient temperature of 2°C and 9°C below the U-Tube Alanod version tests during optical efficiency and 200°C measurements respectively.

In Figure 25 and Table 13 the performance values are reported based on DNI. As one could see, this chart is very different from Figure 24. The main reason for the difference is that the amount of diffuse radiation measured during the tests ranged from 15% to 23%.

4.3.5.Improvements to East-West Collector (X-Tube, U-Tube, and Reflectech)

The proposed improvements to the East-West Counterflow with Alanod were to change to the U-Tube and the X-Tube (extruded tube) and to add Reflectech film to the reflectors. Figure 81 and Figure 82 compare these improved designs to the original counterflow with Alanod design. The charts assume that the ambient temperature is 25°C and the effective irradiance is 1000 W/m². The efficiencies shown in Figure 81 and Figure 82 are based on effective irradiance and DNI, respectively.

As seen in Figure 81 and Figure 82, the use of the X-tube over the counterflow tube appears to have improved the performance at lower temperatures while having little effect at higher temperatures. The ambient temperature and the percent of the irradiance being diffuse during the tests for the East-West Counterflow and the X-Tube were not much different. These small differences are unlikely to have contributed to any error in comparing these two collectors.

The assumed optical efficiency of the X-Tube collector looks higher than one would expect by about two percentage points. This error is likely due to the nature of using a linear extrapolation to estimate the optical efficiency.

Employing the U-tube in place of the counterflow tube in the Alanod collector seems to have also improved the efficiency. The increase in the efficiency seems to be consistent through all temperatures tested. At lower temperatures, the U-tube with Alanod collector does not appear to perform as well as the X-tube collector and this may be due to the additional diffuse radiation during the X-tube testing.

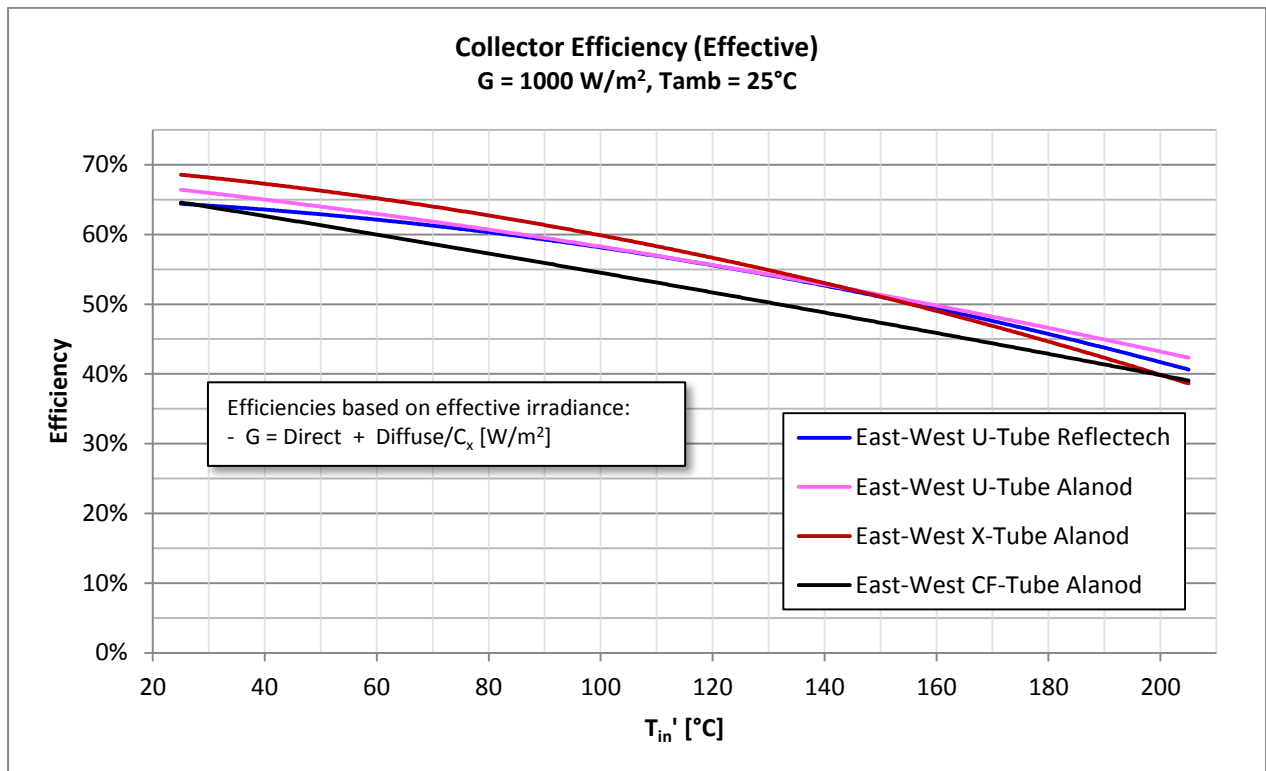


Figure 81. East-West Collector Efficiency (Effective)

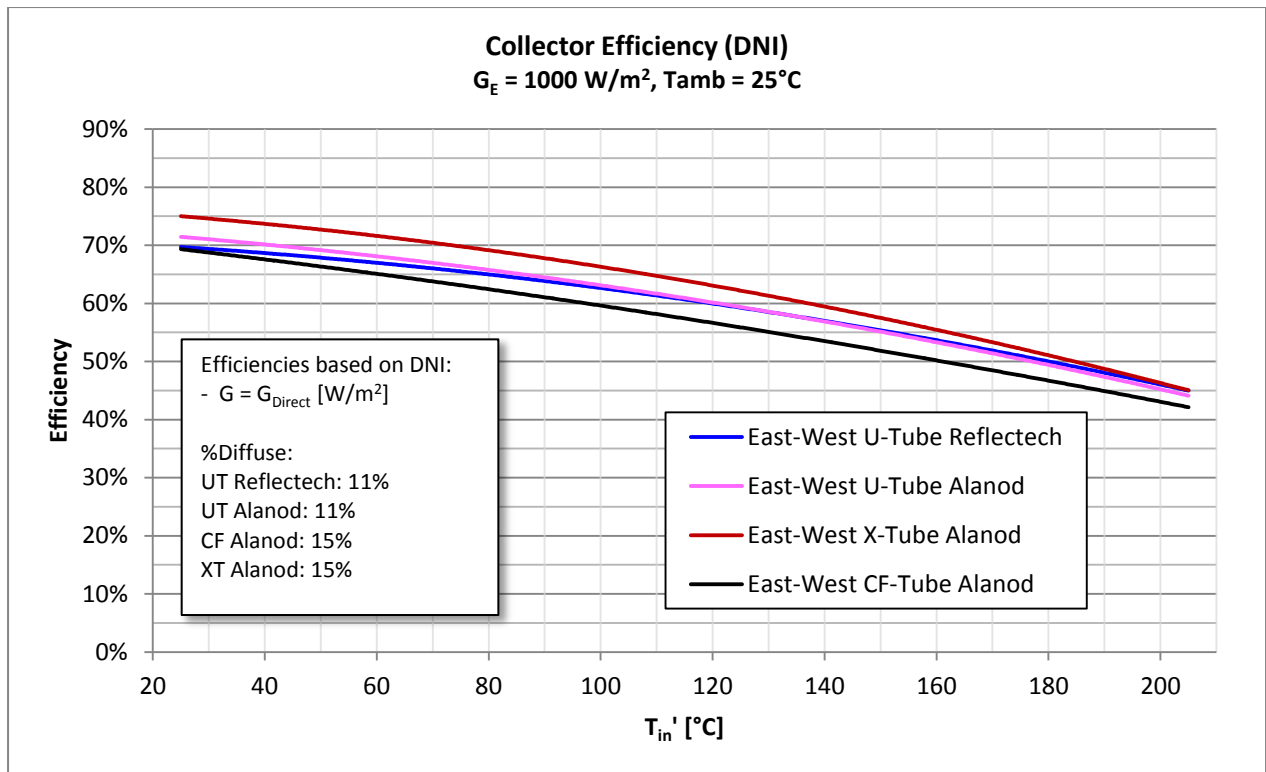


Figure 82. East-West Collector Efficiency (DNI)

Applying Reflectech film over the Alanod reflectors was expected to improve the optical efficiency of the collector in addition to adding to the efficiencies at all temperatures. This anticipated increase in efficiency cannot be seen in the data at any temperature. The most likely reason for this lack of improvement is that applying the Reflectech film was difficult and resulted in bubbles and blemishes. Both the North-South and the East-West versions with Reflectech had many imperfections yet only the North-South version seems to have improved the performance as can be seen in Figure 83 and Figure 84. The fact that the East-West collector has a higher concentration and a lower acceptance angle makes it more sensitive to imperfections in the optics in the system than the North-South version.

When comparing the charts in Figure 81 and Figure 82, there seems to be little difference in the shape of the curves. In addition, the efficiencies based on the direct irradiance only show about five percentage points higher than the efficiencies based on the effective irradiance. This implies that the East-West collector is only able to collect about half of the diffuse irradiance as expected with a concentration of 1.8.

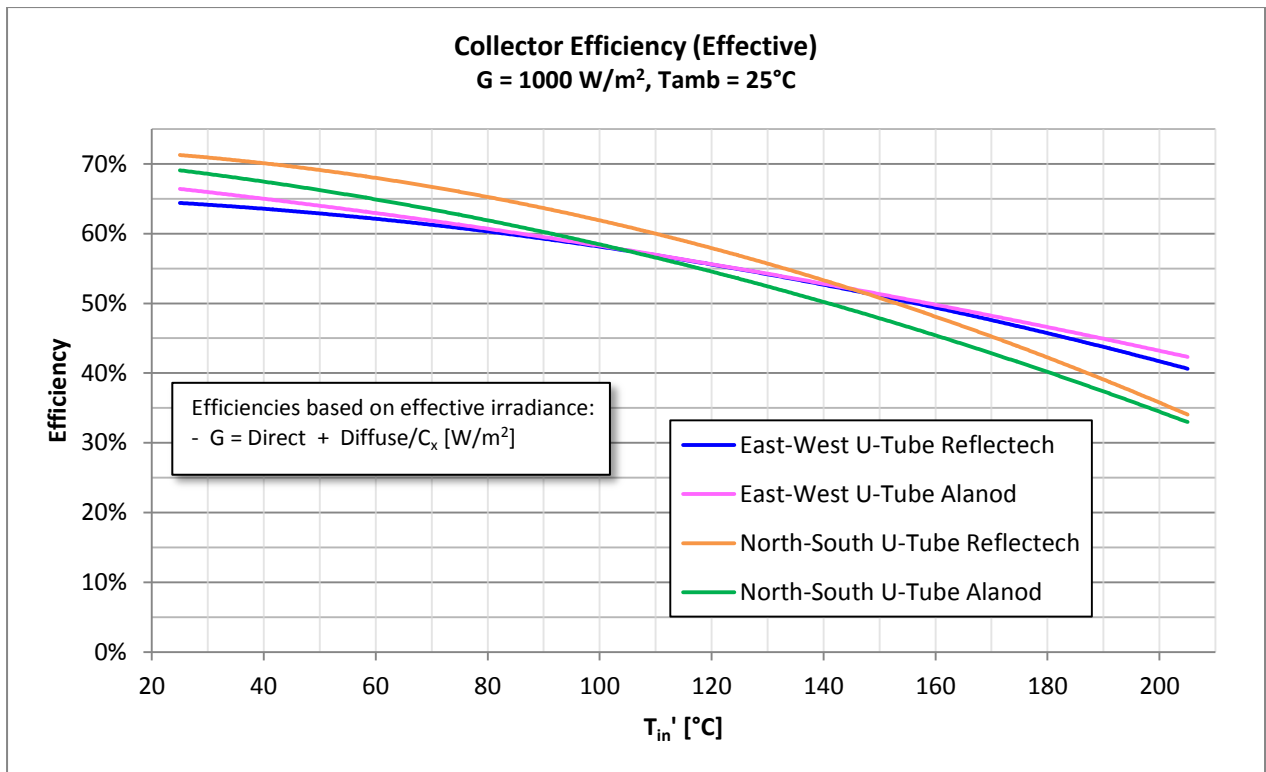


Figure 83. U-Tube Collector Efficiency (Effective)

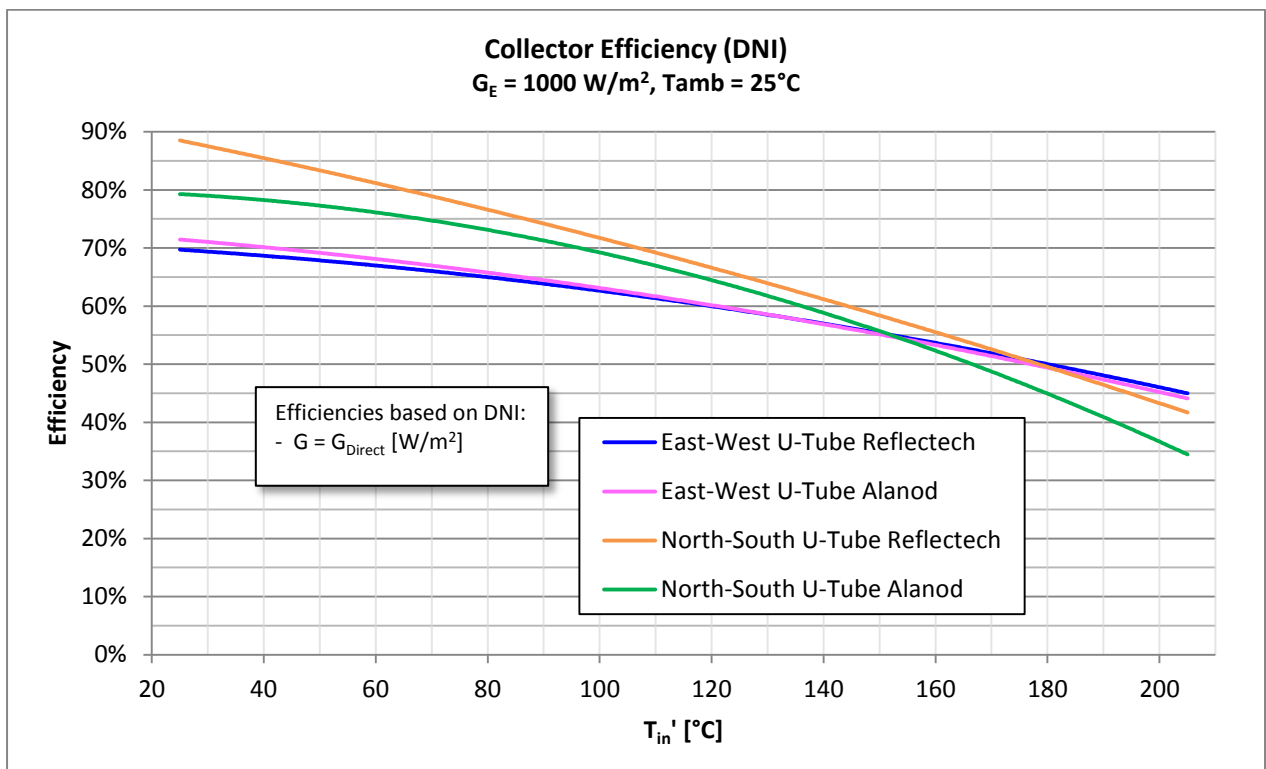


Figure 84. U-Tube Collector Efficiency (DNI)

4.3.6. Possible errors

Errors in the data may come from any of the following: instrumental errors, measurement errors, assumed values, tolerance errors, environmental effects, ground reflection, and errors in theory.

Although calibrated, instruments such as pyranometers, pyrhemometers, thermocouples and other temperature sensors, the flowmeter, and data acquisition systems may have non-trivial errors associated with them. While steps were taken to minimize these sources of error, it is impossible to avoid them completely. Errors in any of these instruments would affect the efficiency measurements and/or the temperature scale.

The effective area of the collector is a possible source of error due to it being measured manually but this error should be less than a fraction of a percent. Any error in the area of the collector would directly affect the calculated efficiency values.

The heat capacity of the oil seems to change over time. Since both of the counterflow and the North-South U-Tube with Alanod collectors' test did not use a calorimeter, the assumed values have an unknown error. An outside source, Rose Consulting, measured the heat capacity of the oil in November 2007 and in September 2009. The measurements in 2007 found the heat capacity of the oil to be less than the table values provided by the oil's manufacturer while the measurements in 2009 found that the heat capacity was higher than the table values. The September 2009 measurements from Rose Consulting agree well with the heat capacity measured during the East-West U-Tube with Alanod tests.

The shape of the reflector and the position of the holes in the frame are subject to tolerance errors that would affect the optical efficiency and the acceptance angle. In addition, the surface quality of the reflector surface will affect the results.

Soiling of the reflectors and the glass tubes can have a negative effect on the optical efficiency.

Ground reflection is inevitable when testing solar thermal collectors outdoors. The amount of ground reflection available to the collector depends on the optics and orientation of the collector, the time of day and the position of the tracker. While the pyranometer mounted on the tracker should be able to detect all or most of the ground reflection, the angle of incidence may be too severe to be accepted by the collector. Collectors with lower concentrations and collectors oriented in a vertical position like the North-South collectors will be able to accept

more of this reflected radiation. The ground reflection will be treated as diffuse light. Ground reflection can cause variation in data and cause East-West collectors to have an apparent lower than expected performance.

Much of the data presented in this report uses an effective irradiance to represent the amount of available power to the collector. The effective irradiance adjustment attempts to take into account that a concentrating optical system cannot accept all of the diffuse and is therefore not considered in the efficiency. Using this method will favor collectors with larger concentration ratios

Other data is presented in this report uses the direct normal irradiance (DNI) to represent the incoming radiation. This method completely ignores diffuse radiation which favors collectors with low concentrations. Using this method with data having a large percent of the irradiance as diffuse can create apparently high efficiencies.

Since the testing was done outdoors, it is virtually impossible to test with a constant or consistent ambient temperature. The charts and the data presented in this report attempt to minimize the effect of the differences in the ambient temperature by presenting data with the reduced temperature. Unfortunately, these evacuated tube collectors primarily lose heat through radiation which is non-linear. In addition, the Emittance of the absorber is a function of the absorber temperature only and not of the ambient temperature. This creates a less than perfect correction for the ambient temperature which is most apparent when a collector was tested during very different outdoor temperatures or when comparing two different collectors that were tested in different seasons.

5. Conclusions and Recommendations

All of the collectors tested performed well and close to the modeled performances. The East-West designs appear to have an advantage over the North-South designs at temperatures above roughly 140 °C under sunny conditions. In hazy locations and sites where clouds are more frequent, the North-South collector may prove superior. The Reflectech reflectors do attribute a measureable advantage over the Alanod reflectors, although the cost of which may prohibit its use for these collectors. The best performing tube appears to be the U-tube and as long as its costs are not much more than the other tube types, it may be the best candidate for commercial use.

A comparison of the performance of the top collectors tested with commercially available solar thermal collectors can be found in Figure 85⁸. As can be seen, the performance of both the East-West and the North-South designs fair very well against the competition over a large temperature range. This performance advantage, in addition to the non-tracking feature, suggests that these designs have the potential to be a viable alternative to the completion in the low and medium temperature ranges.

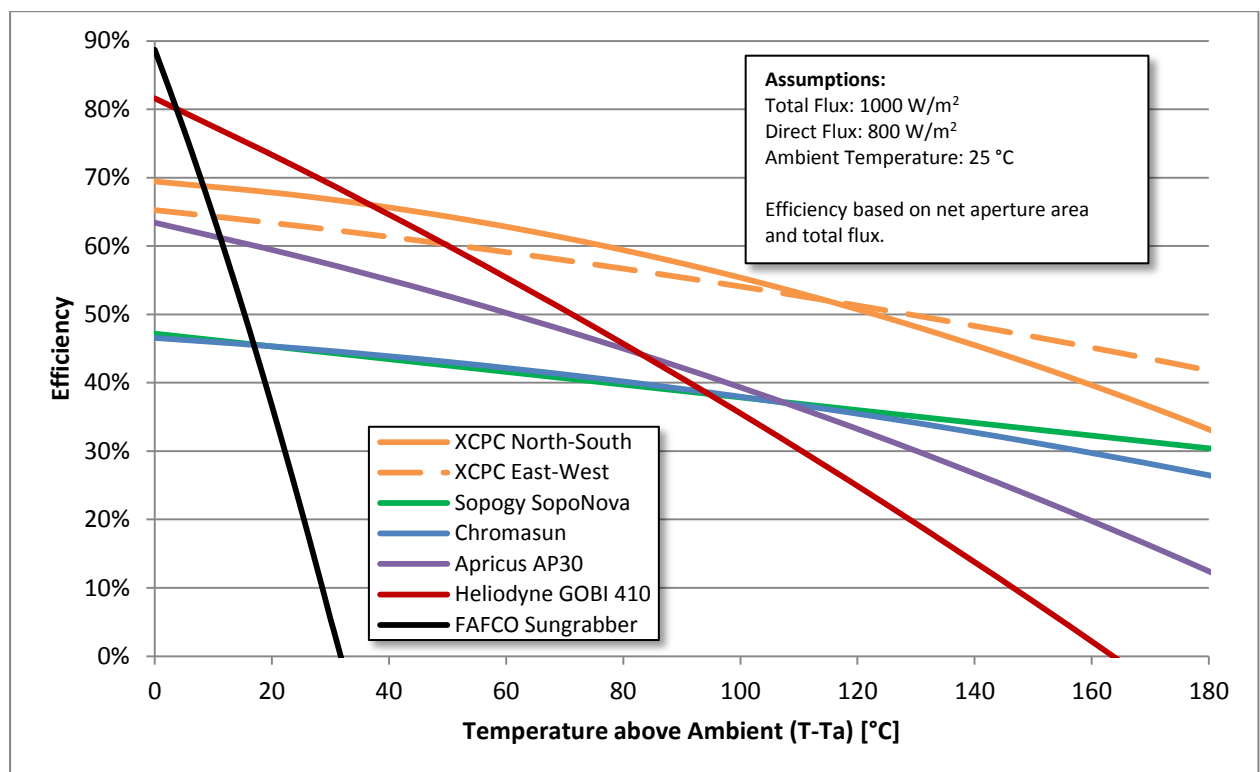


Figure 85. Performance comparison to commercial products [28]

⁸ The performance of the commercial collectors are based on SRCC ratings (in Appendix)

The high performance at 140 °C above the ambient suggests that the technology would be ideal for applications using a double effect absorption chiller. This conclusion led a team of researchers at UC Merced to create and analyze a demonstration project of the first non-tracking solar thermal system powering a double effect absorption chiller for air conditioning.

Future improvements to the design can include: improved selective coating, higher concentrations, anti-reflective coating on glass, and improved absorber to reduce thermal resistance. With these possible improvements, and possibly more, the XCPC may have a chance to perform well at temperatures approaching 300 °C and open up the opportunity to be applied to power generation.

APPENDIX A: Spec Sheets

Table 30. Alanod MIRO90 properties

Measurement	Measurement Method	Value
Total Light Reflection / 8°	DIN 5036-3 (U-Kugel)	≥ 93,5 %
Diffuse Light Reflection / 8°	DIN 5036-3 (U-Kugel)	≤ 10,0 %
Total Light reflection / 30°	ASTM E-1651 (TR-2)	≥ 93,0 %
Brightness at 30° incident angle parallel to the rolling direction, light acceptance angle < 2°	ASTM E-430 (Hunter Dorigon)	≥ 87,0 %
Brightness at 30° incident angle across the rolling direction, light acceptance angle < 2°	ASTM E-430 (Hunter Dorigon)	≥ 85,0 %
Brightness at 20° incident angle, light acceptance angle 10°	ISO 7668 (Dr. Lange)	≥ 88,0 %
Brightness at 60° incident angle, light acceptance angle 10°	ISO 7668 (Dr. Lange)	≥ 88,0 %
Total Spectral Light Reflection	DIN 5033 (Minolta)	≥ 93,5 %
Solar Light reflection (10°)	AM 1.5 ISO	≥ 88,5 %


Table 31. Durather 600 properties

PROPERTY VS. TEMPERATURE CHART

DURATHERM 600 METRIC

TEMPERATURE (Celsius)	DENSITY (kg/m ³)	KINEMATIC VISCOSITY (centistokes)	DYNAMIC VISCOSITY (centipoise)	THERMAL CONDUCTIVITY (W/m.K)	HEAT CAPACITY (kJ/kg.K)	VAPOUR PRESSURE (KPA)
-5	872.40	710.01	619.41	0.144	1.830	0.00
5	865.70	297.85	257.85	0.144	1.860	0.00
15	859.00	143.47	123.24	0.143	1.890	0.00
25	852.30	77.27	65.86	0.143	1.930	0.00
35	845.60	45.56	38.53	0.142	1.960	0.00
45	838.80	29.28	24.56	0.142	1.990	0.00
55	832.10	20.15	16.76	0.141	2.020	0.00
65	825.40	14.51	11.98	0.141	2.060	0.00
75	818.70	10.86	8.89	0.140	2.090	0.00
85	812.00	8.39	6.81	0.139	2.120	0.00
95	805.20	6.66	5.36	0.139	2.150	0.00
105	798.50	5.41	4.32	0.138	2.190	0.00
115	791.80	4.48	3.55	0.138	2.220	0.01
125	785.10	3.78	2.97	0.137	2.250	0.01
135	778.30	3.23	2.52	0.137	2.280	0.02
145	771.60	2.80	2.16	0.136	2.320	0.04
155	764.90	2.46	1.88	0.136	2.350	0.06
165	758.20	2.18	1.65	0.135	2.380	0.09
175	751.50	1.95	1.46	0.135	2.420	0.14
185	744.70	1.76	1.31	0.134	2.450	0.21
195	738.00	1.59	1.18	0.134	2.480	0.31
205	731.30	1.46	1.07	0.133	2.510	0.45
215	724.60	1.34	0.97	0.133	2.550	0.64
225	717.90	1.24	0.89	0.132	2.580	0.90
235	711.10	1.15	0.82	0.132	2.610	1.25
245	704.40	1.07	0.76	0.131	2.640	1.70
255	697.70	1.01	0.70	0.131	2.680	2.30
265	691.00	0.95	0.66	0.130	2.710	3.06
275	684.30	0.90	0.61	0.130	2.740	4.04
285	677.50	0.85	0.57	0.129	2.780	5.28
295	670.80	0.81	0.54	0.129	2.810	6.84
305	664.10	0.77	0.51	0.128	2.840	8.78
315	657.40	0.74	0.48	0.128	2.870	11.17

SRCC Certifications

SOLAR COLLECTOR CERTIFICATION AND RATING  SRCC OG-100	CERTIFIED SOLAR COLLECTOR SUPPLIER: Fafco, Inc. 435 Otterson Dr. Chico, CA 95928 USA MODEL: Sungrabber COLLECTOR TYPE: Unglazed Flat-Plate CERTIFICATION#: 2008007A Original Certification Date: 29-APR-08
--	---

ALL SIZES OF THIS COLLECTOR MODEL ARE CERTIFIED

COLLECTOR THERMAL PERFORMANCE RATING							
Kilowatt-hours Per Square Meter Per Day				Thousands of BTU Per Square Foot Per Day			
CATEGORY (Ti-Ta)	CLEAR DAY (6.3 kWh / m ² .day)	MILDLY CLOUDY (4.7 kWh / m ² .day)	CLOUDY DAY (3.1 kWh / m ² .day)	CATEGORY (Ti-Ta)	CLEAR DAY (2000 Btu / ft ² .day)	MILDLY CLOUDY (1500 Btu / ft ² .day)	CLOUDY DAY (1000 Btu / ft ² .day)
A (-5 °C)	6.6	5.2	3.8	A (-9 °F)	2.1	1.6	1.2
B (5 °C)	4.5	3.1	1.8	B (9 °F)	1.4	1.0	0.6
C (20 °C)	2.0	0.9	0.0	C (36 °F)	0.6	0.3	0.0
D (50 °C)	0.0	0.0	0.0	D (90 °F)	0.0	0.0	0
E (80 °C)	0.0	0.0	0.0	E (144 °F)	0.0	0.0	0.0

A- Pool Heating (Warm Climate) B- Pool Heating (Cool Climate) C- Water Heating (Warm Climate) D- Water Heating (Cool Climate) E- Air Conditioning

COLLECTOR SPECIFICATIONS

Gross Area: 2.266 m² 24.39 ft²
Dry Weight: 3.6 kg 8. lb
Test Pressure: 310. KPa 45. psig

Net Aperture Area: 2.27 m² 24.39 ft²
Fluid Capacity: 6.5 liter 1.7 gal

COLLECTOR MATERIALS

Frame: None
Cover (Outer): None
Cover (Inner): None

Pressure Drop

Flow		ΔP	
ml/s	gpm	Pa	in H ₂ O
150.00	2.38	1875.50	7.54
250.00	3.96	4631.3	18.6
350.00	5.55	8591.60	34.53

Absorber Material: Tube - UV Stabilized Plastic Polymer /
Absorber Coating: None

Insulation Side: None
Insulation Back:

TECHNICAL INFORMATION

Efficiency Equation [NOTE: Based on gross area and (P)=Ti-Ta]

SI Units: $\eta = 0.887 - 22.61780 (P)/I + 0.17107 (P)^2/I$

IP Units: $\eta = 0.887 - 3.98413 (P)/I + 0.01674 (P)^2/I$

Y INTERCEPT

0.882 -18.858 W/m².°C

0.882 -3.322 Btu/hr.ft².°F

SLOPE

Incident Angle Modifier [(S)=1/cosθ - 1, 0°<θ<=60°]

Kτα = 1 0.159 (S) -0.107 (S)²

Kτα = 1 0.05 (S) Linear Fit

Test Fluid: Water

Test Flow Rate: 69.7 ml/s.m² 0.1027 gpm/ft²


REMARKS:

November, 2011

Certification must be renewed annually. For current status contact:

SOLAR RATING & CERTIFICATION CORPORATION

400 High Point Drive, Suite 400 ♦ Cocoa, Florida 32926 ♦ (321) 213-6037 ♦ Fax (321) 821-0910

<p align="center">SOLAR COLLECTOR CERTIFICATION AND RATING</p>  <p align="center">SRCC OG-100</p>	<p>CERTIFIED SOLAR COLLECTOR</p> <p>SUPPLIER: Heliodyne, Inc. 4910 Seaport Avenue Richmond, CA 94804 USA</p> <p>MODEL: GOBI 410 001</p> <p>COLLECTOR TYPE: Glazed Flat-Plate</p> <p>CERTIFICATION#: 2010115A</p> <p>Original Certification Date: 28-MAR-11</p>
---	--

COLLECTOR THERMAL PERFORMANCE RATING							
Kilowatt-hours Per Panel Per Day				Thousands of BTU Per Panel Per Day			
CATEGORY (Ti-Ta)	CLEAR DAY (6.3 kWh / m ² .day)	MILDLY CLOUDY (4.7 kWh / m ² .day)	CLOUDY DAY (3.1 kWh / m ² .day)	CATEGORY (Ti-Ta)	CLEAR DAY (2000 Btu / ft ² .day)	MILDLY CLOUDY (1500 Btu / ft ² .day)	CLOUDY DAY (1000 Btu / ft ² .day)
A (-5 °C)	16.9	12.8	8.7	A (-9 °F)	57.6	43.5	29.5
B (5 °C)	15.4	11.2	7.1	B (9 °F)	52.4	38.4	24.4
C (20 °C)	13.1	9.1	5.1	C (36 °F)	44.7	30.9	17.2
D (50 °C)	9.0	5.2	1.7	D (90 °F)	30.7	17.7	5.7
E (80 °C)	5.3	2.1	0.0	E (144 °F)	18.2	7.0	0.0

A- Pool Heating (Warm Climate) B- Pool Heating (Cool Climate) C- Water Heating (Warm Climate) D- Water Heating (Cool Climate) E- Air Conditioning

COLLECTOR SPECIFICATIONS

Gross Area: 3.732 m² 40.17 ft²
 Dry Weight: 43.5 kg 96. lb
 Test Pressure: 1103. KPa 160. psig

Net Aperture Area: 3.47 m² 37.33 ft²
 Fluid Capacity: 5.1 liter 1.3 gal

COLLECTOR MATERIALS

Frame: Aluminum
 Cover (Outer): Tempered glass
 Cover (Inner):

Pressure Drop

Flow		ΔP	
ml/s	gpm	Pa	in H ₂ O
20.00	0.32	41.93	0.17
50.00	0.79	121.0	0.5
80.00	1.27	219.43	0.88

Absorber Material: Tube - Copper /
Plate - Aluminum
 Absorber Coating: Selective coating

Insulation Side: Foam
 Insulation Back: foam

TECHNICAL INFORMATION

Efficiency Equation [NOTE: Based on gross area and (P)=Ti-Ta]

SI Units:	η = 0.750	-3.68570 (P)/l	-0.00548 (P) ² /l	Y INTERCEPT	0.752	SLOPE	-4.023 W/m ² .°C
IP Units:	η = 0.750	-0.64924 (P)/l	-0.00054 (P) ² /l		0.752		-0.709 Btu/hr.ft ² .°F


Incident Angle Modifier [(S)=1/cosθ - 1, 0°<θ<=60°]

Kτα = 1 -0.078 (S) -0.086 (S)²
 Kτα = 1 -0.17 (S) Linear Fit

Test Fluid: Water
 Test Flow Rate: 22.2 ml/s.m² 0.0328 gpm/ft²

REMARKS:

November, 2011

SOLAR COLLECTOR CERTIFICATION AND RATING  SRCC OG-100	CERTIFIED SOLAR COLLECTOR SUPPLIER: Apricus Inc. 6 Sycamore Way, Unit #2 Branford, CT 06405 USA MODEL: Apricus AP-30 COLLECTOR TYPE: Tubular CERTIFICATION#: 2007033A Original Certification Date: 24-AUG-09
--	---

COLLECTOR THERMAL PERFORMANCE RATING							
Kilowatt-hours Per Panel Per Day				Thousands of BTU Per Panel Per Day			
CATEGORY (Ti-Ta)	CLEAR DAY (6.3 kWh / m ² .day)	MILDLY CLOUDY (4.7 kWh / m ² .day)	CLOUDY DAY (3.1 kWh / m ² .day)	CATEGORY (Ti-Ta)	CLEAR DAY (2000 Btu / ft ² .day)	MILDLY CLOUDY (1500 Btu / ft ² .day)	CLOUDY DAY (1000 Btu / ft ² .day)
A (-5 °C)	13.5	10.2	6.9	A (-9 °F)	46.1	34.8	23.5
B (5 °C)	12.9	9.6	6.3	B (9 °F)	44.0	32.7	21.4
C (20 °C)	11.9	8.6	5.3	C (36 °F)	40.6	29.3	18.0
D (50 °C)	10.0	6.7	3.5	D (90 °F)	34.2	23.0	11.8
E (80 °C)	7.9	4.7	1.7	E (144 °F)	27.1	15.9	5.9

A- Pool Heating (Warm Climate) B- Pool Heating (Cool Climate) C- Water Heating (Warm Climate) D- Water Heating (Cool Climate) E- Air Conditioning

COLLECTOR SPECIFICATIONS

Gross Area: 4.158 m² 44.76 ft²
 Dry Weight: 96.2 kg 212. lb
 Test Pressure: 1103. KPa 160. psig

Net Aperture Area: 2.98 m² 32.05 ft²
 Fluid Capacity: 1.0 liter 0.3 gal

COLLECTOR MATERIALS

Frame: Stainless Steel
 Cover (Outer): Glass Vacuum Tube
 Cover (Inner): None

Pressure Drop

Flow		ΔP	
ml/s	gpm	Pa	in H ₂ O
20.00	0.32	105.00	0.42
50.00	0.79	524.0	2.1
80.00	1.27	1257.00	5.05

Absorber Material: Tube - Copper /
Plate - Aluminum

Insulation Side: Vacuum

Absorber Coating: Aluminum Nitride

Insulation Back: Vacuum

TECHNICAL INFORMATION

Efficiency Equation [NOTE: Based on gross area and (P)=Ti-Ta]

SI Units: $\eta = 0.456 - 1.35090 (P)/I - 0.00381 (P)^2/I$

IP Units: $\eta = 0.456 - 0.23796 (P)/I - 0.00037 (P)^2/I$

Y INTERCEPT

0.458 -1.579 W/m².°C

0.458 -0.278 Btu/hr.ft².°F

Incident Angle Modifier [(I)=1/cosθ - 1, 0°<θ<=60°]

K_{τα} = 1 1.306 (S) -1.034 (S)²

K_{τα} = 1 0.23 (S) Linear Fit


Test Fluid: Water


Test Flow Rate: 20.0 ml/s.m² 0.0294 gpm/ft²

REMARKS:

Tested with long axis of tubes oriented north-south. IAM perpendicular to the tubes is listed above. IAM parallel to the tubes = 1.0 - 0.09(S)

November, 2011

SOLAR COLLECTOR CERTIFICATION			CERTIFIED SOLAR COLLECTOR				
			SUPPLIER:		Sopogy, Inc. 2660 Waiwai Loop Honolulu, HI 96819 USA		
			MODEL:		SopoNova 4.1		
			COLLECTOR TYPE:		Concentrating		
			CERTIFICATION#:		2010113A		
Original Certification Date: 12-Aug-11							
COLLECTOR SPECIFICATIONS (for the tested collector)							
Gross Area	6.712 m ²	72.24 ft ²	Gross Length	4.105 m	13.47 ft		
Aperture Area	5.384 m ²	57.95 ft ²	Gross Width	1.635 m	5.364 ft		
Absorber Area	0.088 m ²	0.9472 ft ²	Gross Depth	1.81 m	5.938 ft		
Fluid Capacity	1.27 liter	0.3355 gal	Test Pressure	1103 kPa	160 psi		
Dry Weight	79.38 kg	175 lb	Concentration Ratio	61			
Tracking: single axis			Control System: active				
Cover Geometry: none			Reflector Geometry: parabolic trough				
COLLECTOR MATERIALS and COATINGS							
Cover: borosilicate			Reflector: aluminum, polymeric laminate				
Absorber: 304 stainless steel tube			Absorber Coating: black chrome				
TECHNICAL INFORMATION							
Collector Model: (Based on Aperture Area)							
$Q/A_a = F'(\tau\alpha)_{en} K_{\theta b}(\Theta)G_b + F'(\tau\alpha)_{en} K_{\theta d}(\Theta)G_d - c_1(t_m - t_a) - c_2(t_m - t_a)^2 - c_3u(t_m - t_a) + c_4(E_L - \sigma t_a^4) - c_5 dt_m/dt - c_6uG$							
$K(\Theta) = 1 - b_0 [1/\cos(\Theta) - 1]$							
Collector efficiency factor: $F'(\tau\alpha)_{en}$				0.5897			
Incident angle modifier for diffuse radiation: $K_{\theta d}$				0.00			
Longitudinal incident angle modifier constant: b_{0L}				0.52			
Transverse incident angle modifier constant: b_{0T}				0.00			
Heat loss coefficient: c_1				0.9317	[W/(m ² K)]		
Temperature dependence of the heat loss coefficient: c_2				0.00	[W/(m ² K ²)]		
Wind speed dependence of the heat loss coefficient: c_3				0.00	[J/(m ³ K)]		
Sky temperature loss coefficient: c_4				0.00	[W/(m ² K)]		
Effective thermal capacity: c_5				2459.2	[J/(m ² K)]		
Wind dependence of zero-loss efficiency: c_6				0.01248	[s/m]		
IAM	10°	20°	30°	40°	50°	60°	70°
$K_{\theta T}(\Theta_T)$							
$K_{\theta L}(\Theta_L)$	0.997	0.985	0.932	0.782	0.661	0.496	0.378
Impact Safety Rating: 0							
Test Conditions:							
Max Fluid Temperature During Efficiency Test: 150 °C				Wind Speed Range During Efficiency Test: 0.4 to 3.1 m/s			
Test Fluid: water				Test Flow Rate: 0.1730 kg/sec			
Exposure Test Conducted: wet				Tested Method: SRCC Standard 600			

SOLAR COLLECTOR CERTIFICATION 			CERTIFIED SOLAR COLLECTOR SUPPLIER: Chromasun, Inc. 1050 N 5th Street, Suite San Jose, CA 95112 MODEL: MCT-HT-001 COLLECTOR TYPE: Concentrating CERTIFICATION#: 2010064A				
Original Certification Date: 24-May-11							
COLLECTOR SPECIFICATIONS (for the tested collector)							
Gross Area	3.99 m ²	42.95 ft ²	Gross Length	3.390 m	11.12 ft		
Aperture Area	3.39 m ²	36.49 ft ²	Gross Width	1.230 m	4.04 ft		
Absorber Area	0.30 m ²	3.23 ft ²	Gross Depth	0.316 m	1.04 ft		
Fluid Capacity	0.9 liter	0.238 gal	Test Pressure	1110 kPa	161.5 psi		
Dry Weight	99.79 kg	220 lb	Concentration Ratio	20			
Tracking: Single axis			Control System: Active				
Cover Geometry: Flat			Reflector Geometry: Fresnel				
COLLECTOR MATERIALS and COATINGS							
Cover: Low Iron Glass			Reflector: Coated Aluminum				
Absorber: Stainless Steel, U-tube			Absorber Coating: Black Chrome				
TECHNICAL INFORMATION							
Collector Model: (Based on Aperture Area)							
$Q/A_a = F'(\tau\alpha)_{en} K_{\Theta b}(\Theta) G_b + F'(\tau\alpha)_{en} K_{\Theta d}(\Theta) G_d - c_1(t_m - t_a) - c_2(t_m - t_a)^2 - c_3 u(t_m - t_a) + c_4(E_L - \sigma t_a^4) - c_5 dt_m/dt - c_6 u G$							
$K(\Theta) = 1 - b_0 [1/\cos(\Theta) - 1]$							
Collector efficiency factor: $F'(\tau\alpha)_{en}$				0.565			
Incident angle modifier for diffuse radiation: $K_{\Theta d}$				0.12			
Longitudinal incident angle modifier constant: b_{0L}				0.13			
Transverse incident angle modifier constant: b_{0T}				-0.19			
Heat loss coefficient: c_1				0.54	[W/(m ² K)]		
Temperature dependence of the heat loss coefficient: c_2				0.0032	[W/(m ² K ²)]		
Wind speed dependence of the heat loss coefficient: c_3				0.00	[J/(m ³ K)]		
Sky temperature loss coefficient: c_4				0.00	[W/(m ² K)]		
Effective thermal capacity: c_5				7800	[J/(m ² K)]		
Wind dependence of zero-loss efficiency: c_6				0.00	[s/m]		
IAM	10°	20°	30°	40°	50°	60°	70°
$K_{\Theta T}(\Theta_T)$	1.003	1.012	1.030	1.059	1.110	1.190	1.003
$K_{\Theta L}(\Theta_L)$	0.998	0.992	0.980	0.96			
Impact Safety Rating: 0							
Test Conditions:							
Max Fluid Temperature During Efficiency Test: 179. °C				Wind Speed Range During Efficiency Test: 0.0 to 1.68 m/s			
Test Fluid: Water				Test Flow Rate: 0.114 kg/sec			
Exposure Test Conducted: Wet				Tested Method: SRCC Standard 600			
Remarks:							

APPENDIX B: Code

Finite Element Code (MATLAB) [29]:

```
%Counterflow Model - UCMERI Summer Research Fellowship
%Kevin Balkoski
%UC Merced
%9-3-10
clear all
clc

n=50; %Number of divisions

%Properties and Dimensions

%Absorber Dimensions
D_Ae=56e-3; %[m]. Diameter of Metal Absorber
thick_A=1e-3; %[m]. Absorber thickness
L=1.640; %[m]. Length of metal absorber
A_A = pi*D_Ae*L; %[m^2]. Area of absorber
dx = L/(n-1); %[m]. Divided length
dA_Ae=pi*D_Ae*dx; %[m^2]. Area of metal absorber
dA_A=pi*(D_Ae-2*thick_A)*dx; %[m^2]. Area of metal absorber
dA_t=thick_A*dx; %[m^2]. Cross section area of absorber

%Absorber Properties
alpha_a=0.904; %Absorption coefficient
epsilon_A=(T -273)*.00008+.048; %Emmissivity of selective coating on absorber
k_Al=240; %[W/m-K]. Thermal conductivity of aluminum
c_Al=.900; %[W-s/g-K]. Heat capacity of aluminum
rho_Al=2.700; %[g/m^3]. Density of aluminum
h_cont=25000; %[W/m2-K]. Contact "conductance" between tube and absorber

%Glass Dimensions
D_ge = 65e-3; %[m]. Diameter of external wall: glass
D_g = 61e-3; %[m]. Diameter of internal wall: glass

A_ge = pi*D_ge*L; %[m^2]. Area of external wall of glass
A_g = pi*D_g*L; %[m^2]. Area of internal wall of glass

dA_ge = pi*D_ge*dx; %[m^2]. Area of external wall of glass
dA_g = pi*D_g*dx; %[m^2]. Area of internal wall of glass

%Glass properties
epsilon_g = 0.92; %Emissivity of glass in the infrared range
k_g=1; %[W/mK]. Thermal conductivity of glass
alpha_g=0; %Absorptivity of glass
hg=100; %[W/m2K]. Heat transfer coefficient between glass and air

%Tube Dimensions
D_oe=12e-3; %[m]. External wall: outer tube
D_o=10.5e-3; %[m]. Internal wall: outer tube
D_ie=7e-3; %[m]. External wall: inner tube
D_i=6e-3; %[m]. Internal wall: inner tube
D_h=D_o-D_ie; %[m]. Hydraulic Diameter

thick_o = D_oe - D_o; %[m]. Thickness of Outer Tube
thick_i = D_ie - D_i; %[m]. Thickness of Inner Tube

A_c=(pi/4)*(D_o^2-D_ie^2); %[m^2]. Cross section area for external flow
A_ci=(pi/4)*(D_i^2); %[m^2]. Cross section area for internal flow

Aii=pi*D_i*dx; %[m2]. Differential area of internal wall: inner tube
Aio=pi*D_ie*dx; %[m2]. Differential area of external wall: inner tube
Aoi=pi*D_o*dx; %[m2]. Differential area of internal wall: outer tube

%Tube Properties
k_Cu=400; %[W/m-K]. Thermal conductivity of copper
c_Cu=385; %[W-s/kg-K]. Heat capacity of copper
r_Cu = 0.0000015; %[m]. Pipe roughness for copper pipe.

hii(1:n)=1000; %[W/m2K]. Heat transfer coef from inner tube to inner fluid
```

```

hoi(1:n)=1000;           %[W/m2K]. Heat transfer coef from inner tube to outer fluid
hio(1:n)=1000;           %[W/m2K]. Heat transfer coef from outer tube to outer fluid

%Radiation Constants
Fga=dA_Ae/A_g;
Fgg=1-Fga*(n-1);
sigma=5.67e-8;

%Inputs
m_dot=13.33/1000;        %[kg/s]. Mass flow rate
T_di(1)=200 + 273;        %[K]. Inlet oil temperature
Tamb=25+273;             %[K]. Ambient temperature
Cx=1.8;                  %Concentration Ratio
eta_o=.65;               %Optical efficiency of collector
Gi=1000;                 %[W/m2]. Input solar flux into collector
G=Gi*eta_o*Cx;           %[W/m2]. Input solar flux into absorber
power_in=Gi*Cx*pi*D_Ae*L; %[W]. Power into collector
power_in_t=G*Cx*pi*D_Ae*L; %[W]. Solar power into absorber

%Initial guesses
T_di_guess(1:n)=T_di(1);
T_do_guess(1:n)=T_di(1);
T_a_guess(1:n)=T_di(1)+20;
T_gi_guess=40+273;

d_guess_di=10;
d_guess_do=10;
d_guess_a=10;
d_guess_g=10;
j=0;
while (d_guess_di>.001 || d_guess_do>.001 || d_guess_a>.001 || d_guess_g>0.001) && j <= 20

    cp_di=hcaps(T_di_guess);
    cp_do=hcaps(T_do_guess);
    epsilon_a=emis(T_a_guess);

    M=zeros(5*n,5*n);      %Initialize matrix
    D=zeros(5*n,1);

    %Set 1: Inner Fluid
    M(1,1)=1;
    D(1,1)=T_di(1);        %Apply initial condition

    for i = 2:n

        M(i,i-1)=m_dot*cp_di(i-1)-hii(i-1)*Aii;
        M(i,i)=m_dot*cp_di(i-1);
        M(i,i+n-1)=hii(i-1)*Aii;
        D(i,1)=0;

    end

    %Set 2: Inner side of Inner Pipe
    for i = n+1:2*n

        M(i,i-n)=-hii(i-n)*Aii;
        M(i,i)=hii(i-n)*Aii+2*pi*dx*k_Cu/log(D_ie/D_i);
        M(i,i+n)=-2*pi*dx*k_Cu/log(D_ie/D_i);
        D(i,1)=0;

    end

    %Set 3: Outer Side of Inner Pipe
    for i = 2*n+1:3*n

        M(i,i-n)=-2*pi*dx*k_Cu/log(D_ie/D_i);
        M(i,i)=2*pi*dx*k_Cu/log(D_ie/D_i)+hio(i-2*n)*Aio;
        M(i,i+n)=-hio(i-2*n)*Aio;
        D(i,1)=0;

    end

    %Set 4: Outer Fluid
    M(3*n+1,n)=-hii(n)*Aii+m_dot*cp_di(n);

```

```

M(3*n+1,4*n)=-m_dot*cp_di(n);
M(3*n+1,2*n)=hii(n)*Aii;
D(3*n+1,1)=0;

for i = 3*n+2:4*n

    M(i,i-n)=hio(i-3*n)*Aio;
    M(i,i-1)=-m_dot*cp_do(i-3*n);
    M(i,i)=m_dot*cp_do(i-3*n)-hoi(i-3*n)*Aoi-hio(i-3*n)*Aio;
    M(i,i+n)=hoi(i-3*n)*Aoi;
    D(i,1)=0;

end

%Set 5: Inner Side of Outer Pipe
for i = 4*n+1:5*n

    M(i,i-n)=-hoi(i-4*n)*Aoi;
    M(i,i)=hoi(i-4*n)*Aoi-2*pi*dx*k_Cu/log(D_oe/D_o);
    M(i,i+n)=2*pi*dx*k_Cu/log(D_oe/D_o);
    D(i,1)=0;

end

%Set 6: Outer Side of Outer Pipe
for i = 5*n+1:6*n

    M(i,i)=pi*D_oe/2*dx*h_cont-2*pi*k_Cu*dx/log(D_oe/D_o);
    M(i,i-n)=2*pi*k_Cu*dx/log(D_oe/D_o);
    M(i,i+n)=-pi*D_oe/2*dx*h_cont;
    D(i,1)=0;

end

Rad1=alpha_a*(1-alpha_a)*G*Fga/(Fga*(1-alpha_a)+Fgg-1)-alpha_a*G;
Rad2=Fgg-1;
%Set 7: Absorber
for i = 6*n+1:7*n

    M(i,i-n)=pi*D_oe/2*dx*h_cont;
    M(i,i)=-epsilon_a(i-6*n)*sigma*pi*dx*D_Ae*T_a_guess(i-6*n)^3-pi*D_oe/2*dx*h_cont;
    M(i,7*n+1)=epsilon_a(i-6*n)*pi*dx*D_Ae*sigma*T_gi_guess^3;
    D(i,1)=Rad1*dA_Ae;

end

%Set 8: Inner side of glass
for i = 6*n+1:7*n
    M(7*n+1,i)=epsilon_a(i-6*n)*epsilon_g*Fga*sigma*T_a_guess(i-6*n)^3*pi*dx*D_g;
end
M(7*n+1,7*n+1)=-2*pi*dx*k_g/log(D_g/D_ge)-
mean(epsilon_a)*epsilon_g*Fga*sigma*T_gi_guess^3*pi*dx*D_g*(n-1);
M(7*n+1,7*n+2)=2*pi*dx*k_g/log(D_g/D_ge);
D(7*n+1,1)=-Rad2*pi*dx*D_g;

%Set 9: Outer side of glass
M(7*n+2,7*n+1)=-2*pi*dx*k_g/log(D_ge/D_g);
M(7*n+2,7*n+2)=2*pi*dx*k_g/log(D_ge/D_g)-hg*A_ge;
D(7*n+2,1)=-hg*A_ge*Tamb;

X=M\D;

T_di=X(1:n);
T_ii=X(n+1:2*n);
T_io=X(2*n+1:3*n);
T_do=X(3*n+1:4*n);
T_oi=X(4*n+1:5*n);
T_oo=X(5*n+1:6*n);
T_a= X(6*n+1:7*n);
T_gi=X(7*n+1);
T_go=X(7*n+2);

```

```

d_guess_di=abs(mean(T_di_guess)-mean(T_di))/mean(T_di);
d_guess_do=abs(mean(T_do_guess)-mean(T_do))/mean(T_do);
d_guess_a=abs(mean(T_a_guess)-mean(T_a))/mean(T_a);
d_guess_g=abs(T_gi_guess-T_gi)/T_gi;

T_di_guess=T_di';
T_do_guess=T_do';
T_a_guess=T_a';
T_gi_guess=T_gi;
j=j+1;
end

T=T_di;
T(n+1:2*n)=T_do(n:-1:1);
x=(1:n)*dx-dx;

plot(x,T_di-273);
hold on
plot(x,T_do-273, 'r')

power_out=m_dot*mean([cp_do])*(T_do(1)-T_di(1));
efficiency=power_out/power_in

```

References

- [1]. Goswami, D. Yogi., Frank Kreith, Jan F. Kreider, and Frank Kreith. *Principles of Solar Engineering*. Philadelphia, PA: Taylor & Francis, 2000.
- [2]. DeWinter, Francis. *Solar Collectors, Energy Storage, and Materials*. Cambridge, MA: MIT, 1990.
- [3]. SunTherm Energy, Inc. *Solar Thermal Market Research*. Oct. 2011.
- [4]. Winston, R. 2009. Design and Development of Low-cost, High-temperature, Solar Collectors for Mass Production. California Energy Commission PIER Public Interest Energy Research Program Report: CEC-500-05-021
- [5]. Tovar, Alfonso. "Performance Assessment of Three Concentrating Solar Thermal Units Design with XCPC Reflectors and Evacuated Tubes, Using an Analytical Thermal Model." Thesis. University of California, Merced, 2008.
- [6]. Cisneros, Jesus. "Design and Analysis of Non-Tracking Non-Imaging External Compound Parabolic Concentrator (XCPC) for Low-Cost High Temperature Solar Thermal Collector." Thesis. University of California, Merced.
- [7]. Modest, Michael F. *Radiative Heat Transfer*. Amsterdam: Academic, 2003.
- [8]. "Solar Spectral Irradiance: Air Mass 1.5." *Renewable Resource Data Center (RReDC) Home Page*. National Renewable Energy Laboratory. Web. 14 Oct. 2011.
<<http://rredc.nrel.gov/solar/spectra/am1.5/>>.
- [9]. Mills, Anthony F. *Basic Heat and Mass Transfer*. Upper Saddle River, NJ: Prentice Hall, 1999.
- [10]. Winston, Roland, and Weiya Zhang. "Pushing Concentration of Stationary Solar Concentrators to the Limit." *Optics Express* 18.S1 (2010): A64.
- [11]. Winston, Roland, Juan C. Miñano, Pablo Benítez, and W. T. Welford. *Nonimaging Optics*. Amsterdam: Elsevier Academic, 2005.

- [12]. Winston, Roland. "Light Collection within the Framework of Geometrical Optics." *Journal of the Optical Society of America* 60.2 (1970): 245.
- [13]. "Recent Projects." APG Solar. Web. 10 Nov. 2011.
<http://www.apgsolar.com/projects/image_imfeld.html>.
- [14]. Moran, Michael J., and Howard N. Shapiro. *Fundamentals of Engineering Thermodynamics*. Hoboken, N.J. : Chichester: Wiley ; John Wiley, 2008.
- [15]. "PRESS RELEASE: CLEAN POWER FROM DESERTS." DESERTEC-UK. Web. 10 Nov. 2011. <http://www.trec-uk.org.uk/press/brussels/prince_hassan_presentation.html>.
- [16]. *Sustainable Hot Water Systems*. Apricus. Web. 10 Nov. 2011.
<<http://www.apricus.com/en/america/>>.
- [17]. AREVA Solar. Web. 10 Nov. 2011. <<http://www.areva.com/EN/global-offer-725/concentrated-solar-power-renewable-energies-solutions.html>>.
- [18]. Abengoa Solar. Web. 10 Nov. 2011.
<<http://www.abengoasolar.com/corp/web/en/index.html>>.
- [19]. *Sopogy MicroCSP*. Sopogy. Web. 10 Nov. 2011.
<<http://sopogy.com/microcsp/index.php?id=31>>.
- [20]. Chromasun. Web. 10 Nov. 2011. <<http://chromasun.com/>>.
- [21]. "ReflecTech® Mirror Film - Product." ReflecTech. Web. 10 Nov. 2011.
<<http://www.reflectechsolar.com/product.html>>.
- [22]. *LightTools*. Computer software. Vers. 7.1. Optical Research Associates. Web.
<http://www.opticalres.com/lt/ltprodds_f.html>.
- [23]. Rabl, A. "Comparison of Solar Concentrators." *Solar Energy* 18.2 (1976): 93-111.
- [24]. Winston, R., and H. Hinterberger. "Principles of Cylindrical Concentrators for Solar Energy." *Solar Energy* 17.4 (1975): 255-58.

- [25]. Rabl, A. "Practical Design Considerations for CPC Solar Collectors." *Solar Energy* 22.4 (1979): 373-81.
- [26]. Rabl, Ari. "Solar Concentrators with Maximal Concentration for Cylindrical Absorbers." *Applied Optics* 15.7 (1976): 1871.
- [27]. "600° Heat Transfer Fluid." Duratherm. Web. 10 Nov. 2011. <<http://www.heat-transfer-fluid.com/heat-transfer-fluid/duratherm-600>>.
- [28]. Solar Rating & Certification Corporation. Web. 10 Nov. 2011. <<http://www.solar-rating.org/>>.
- [29]. Burden, Richard L., and J. D. Faires. *Numerical Analysis*. 8th ed. Boston: PWS-Kent Pub., 2005.